

Crystal Nucleation and Growth in Poly(ϵ -caprolactone) Studied by Fast Scanning Differential Calorimetry

Dissertation

zur Erlangung des akademischen Grades
Doktor der Naturwissenschaften
Dr. rer. nat.

am Institut für Physik
der Mathematisch-Naturwissenschaftlichen Fakultät
der Universität Rostock

vorgelegt von

M.Sc. Evgeny Zhuravlev
geboren am 30. September 1983 in Saransk
aus Russland

Rostock, Juni 2010

Gutachter:

Prof. Dr. Christoph Schick	Universität Rostock, Institut für Physik
Prof. Dr. Eberhard Burkel	Universität Rostock, Institut für Physik
Prof. Dr. Toshiji Kanaya	Kyoto University, Institute for Chemical Research

Tag der Disputation: 23.09.2010

Content

1. Introduction	4
2. Literature review	9
2.1. Polymer crystallization.....	9
2.2. Thin film fast scanning calorimetry	21
3. Fast scanning differential calorimeter with power compensation.....	32
3.1. Issues of single sensor calorimeter	32
3.2. Differential temperature control scheme with power compensation	34
3.3. Electric scheme and power difference determination	39
3.4. Hardware and software realization.....	42
3.5. Solidification of metals studied by fast scanning calorimeter.....	45
3.6. Temperature calibration	48
4. Heat capacity determination.....	54
4.1. Scheme for differential power determination.....	54
4.2. Heat Balance	55
4.3. Determination of differential loss function	58
4.4. Crystallization of polyethylene (PE)	62
4.5. Solidification of pure and nucleated poly(ϵ -caprolactone) (PCL)	64
5. Crystal nucleation and overall crystallization kinetics in PCL	67
5.1. Influence of existing nuclei and crystals on subsequent heating	67
5.2. Elimination of homogeneous crystal nuclei formation in PCL on cooling.....	71
5.3. Annealing experiments with PCL	76
5.4. Characteristic time of nucleation and crystallization at different temperatures.....	79
6. Discussion	83
7. Summary	91

8. References	92
Appendix	100
A1. Experimental data for all heating curves after annealing	100
A2. Fast scanning calorimeter software	111
A2.1. Measurement software	111
A2.2. Data evaluation.....	117

1. Introduction

Solidification from the melt has been actively studied since ancient times. The process of metals casting, glass blowing and injection molding of plastics are all basic examples of shaping a liquid in order to produce solid parts.

In modern times, people have been trying to modify these procedures to improve the properties of the product, to reduce manufacturing costs and to make production more environmental-friendly. Special heat treatment is an important constituent of this type of technological processes. An example of such treatments is quenching. In metallic systems, it is commonly used for hardening the materials or in order to avoid phase separation in alloys. Extremely rapid cooling of metallic melts can prevent the formation of crystalline structures. As the result, amorphous vitreous metals are formed, which are of high practical interest nowadays. Very rapid cooling is also used in polymer production to avoid high temperature phase transitions providing a possibility to reduce the degree of crystallinity which results in an increasing toughness of the materials. The critical cooling rate which is needed to make a material amorphous is an important parameter not only for polymers. The ability to quench materials without crystallization allows one performing of crystallization at desired temperatures during a special heat treatment in subsequent heating. This method is used in production to control the crystallization rate in order to modify properties of the final product.

The common way of treating crystallization consists of two different basic processes; critical nuclei formation and their subsequent growth. Same can also be applied to polymers. Nucleation, i.e. the stochastic formation of nuclei of the new phase capable to a further deterministic growth, is an essential ingredient of crystallization. However, the direct measurement of nucleation is not yet possible, as a rule, by the existing techniques. This is due to a very small size of the nuclei and very small effects (e.g. heat effect) which occurs in the course of their formation. Therefore indirect methods are usually utilized in order to detect them. One of them is known as polarized optical microscopy.

In polarized optical microscopy, the number of supercritical nuclei formed can be determined by counting the number of finally formed crystals and identifying both numbers. However, the optical microscopy technique is limited in its application to materials where the crystals formed and matured are visible and that have slow enough crystallization rates. In

calorimetry, the enthalpy of cold crystallization on heating was found to be dependent on the number of previously formed nuclei. As cold crystallization, we denote hereby the crystallization processes occurring at heating the sample from below the glass transition towards the melting temperature. Mathot et al. [1] observed a reduction of the cold crystallization peak on heating after cooling with increasing cooling rate. But, even a high rate differential scanning calorimeter (DSC) was not able to prevent fully the nuclei formation on cooling in poly(l-lactic acid) (PLLA), a rather slowly crystallizing polymer. Oguni et al. [2] and Vyazovkin et al. [3] studied by similar methods nucleation below the glass transition temperature in low molecular mass organic substances by analyzing data on crystallization on heating after annealing at different temperatures for different times. In this way, DSC may serve as an effective tool to study nucleation processes by analyzing the heat effects.

However, most of the existing studies are investigating either crystallization (i.e., nucleation and simultaneous growth) or nucleation in different ranges of temperature. One of the reasons for that is the separation of these two processes in time and temperature. Figure 1A shows the results of several separate measurements of crystal nucleation and growth kinetics in glycerol (taken from [4]).

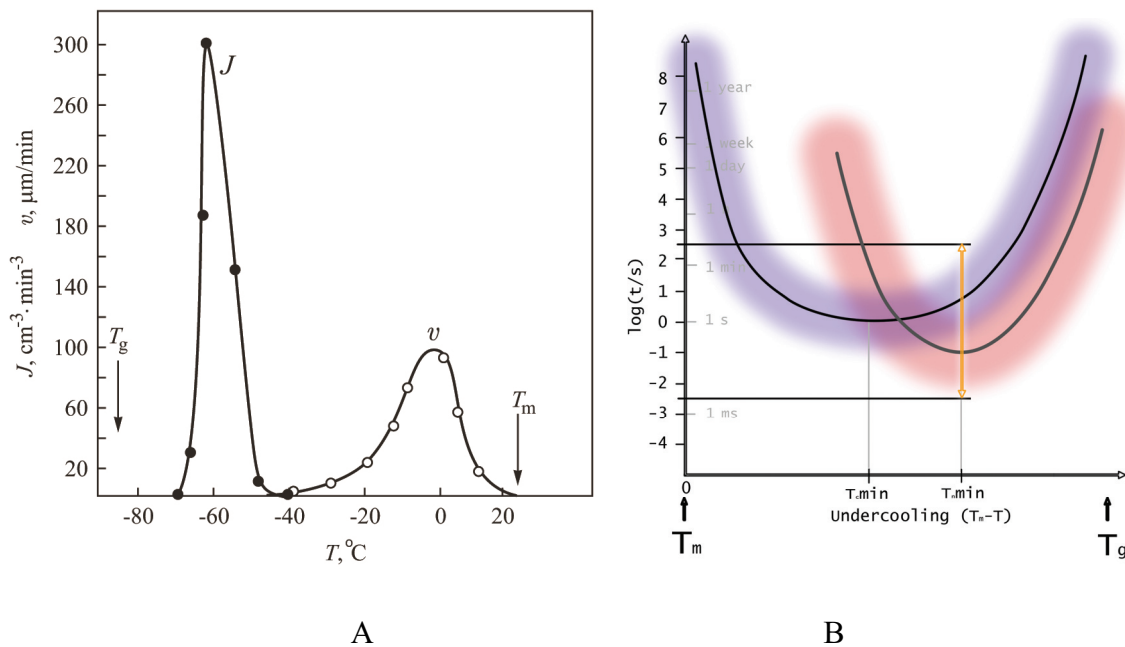


Figure 1. Temperature dependence of the steady-state nucleation rate J and of linear rate of crystal growth v for glycerol from [4] (A). Schematic representation of half-time of nucleation and crystallization versus undercooling temperature (B).

The full separation of these two processes, as shown in Figure 1A, is not always the case and in different materials they can overlap, see Figure 1B. In this case the study of both processes at the same temperature becomes important. In Figure 1B the nucleation and overall crystallization half-times are represented versus undercooling below melting temperature. The shadows below the curves show the distribution of the corresponding processes around their characteristic times. The width of these regions is commonly several orders of magnitude in time. Here a time scale is assigned based on the result of this work showing poly(ϵ -caprolactone) (PCL) crystal nucleation and overall crystallization kinetics. For investigation of nucleation process at least the experiment at maximum nucleation rate (minimum nucleation half-time) is of interest. For simultaneous determination of crystallization half-time (or rate) at this temperature the experiment should cover the time range designated by the orange arrows in Figure 1. In more details the experimental requirements for this study are shown in Figure 2.

For isothermal study of nuclei formation and growth at any temperature it is required to avoid both processes on cooling. Linear cooling profiles are shown as blue lines (4, 6, 7). To avoid crystallization of PCL on cooling at constant rate 500 K/s (linear cooling) is required (line 6). On cooling faster than 7,000 K/s formation of homogeneous nuclei is suppressed (line 7). To finalize crystallization at temperature T_{nmin} , where the nucleation is fastest, a time span of 5 orders of magnitude is required (green line in between red circles 1 and 2). To study both processes at other temperatures an even larger dynamic range is required. Most of the available conventional temperature scanning techniques, e.g. DSC, are limited to 10 K/s (line 4) as the fastest rate because of sample size of at least a few milligrams. Let us consider a hypothetical experiment on a material with the fastest nucleation time of several minutes, which can be avoided at 10 K/s cooling. Following the same ideas as for construction of line 1 and 5, but for slower rates, the crystallization and nucleation half time of the hypothetical material would follow the dashed lines 2 and 3 in Figure 2. The same experiment, which was described previous for a fast crystallizing material, will span again over 5 orders of magnitude in time, but starting from several minutes (upper orange arrow in Figure 2). In this case the crystallization will be finalized only after several months. An investigation at other temperatures will require even more time. In any case, these times are too long and not practicable for a large number of experiments, which are required for a kinetic study of the two processes.

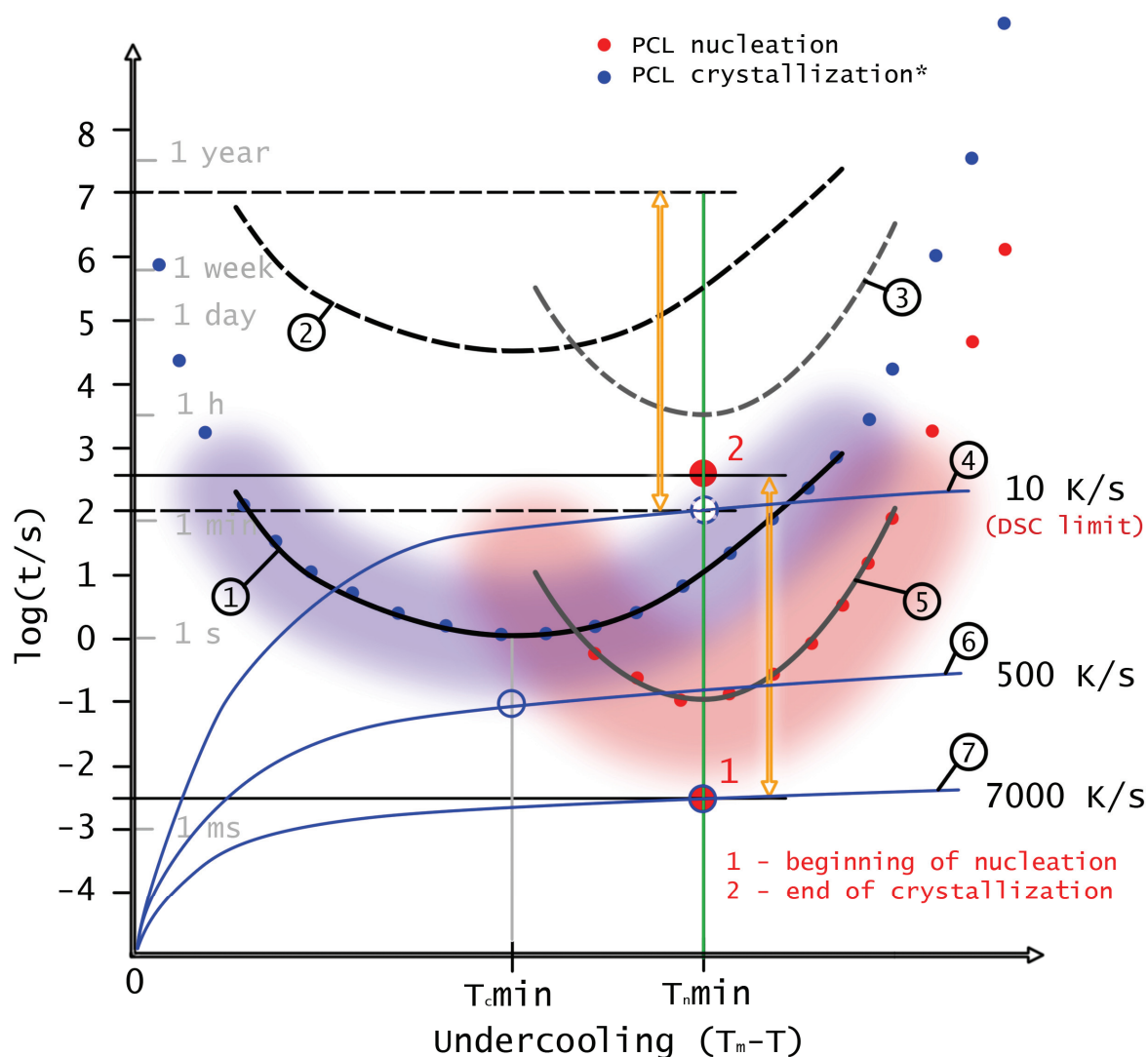


Figure 2. Schematic representation of crystal nucleation and overall crystallization kinetics, for details see text.

From the discussion above it follows that for the investigation of polymer crystal nucleation and growth, the conventional techniques cannot cool fast enough to prevent nucleation on cooling for materials, which allow studying crystallization at the same temperature in a reasonable time (< 1 month). Therefore it was decided to use a technique which allows appropriately fast cooling. The single sensor fast scanning calorimeter [5] allows heating and cooling of nano-gram samples at rates starting from 100 K/s up to 1 MK/s. This dynamic range is appropriate for the above described investigation. Nevertheless, the single sensor calorimeter has several limitations regarding temperature control and quantitative measurements.

To improve the existing technique we design a differential scheme of two of such sensors, with power compensation. The presence of an empty reference sensor reduces the influence of heat losses and addenda heat capacity on the obtained data dramatically. For a better sample temperature control, particularly in the transition regions, power compensation was introduced. To separate the two control circuit's power compensation was done asymmetrically compensating only sample side temperature. Furthermore, user-friendly experiment management software and a software package for data evaluation were developed.

The improved calorimeter is able to perform heat flow measurements during controlled heating and cooling up to 500,000 K/s. The new control circuit allows performing isothermal experiments for times from 0.1 ms (with overshoot of < 1 K). The device is therefore well suited for an isothermal study of crystal nucleation and growth.

In the following chapters a short review of the state of the art regarding nucleation and growth, and its investigation are given. The basis of polymer crystallization, recent observations and available techniques for investigation of solidification will be briefly discussed. The technique review includes a description of existing ultra-fast scanning calorimeters which were used as a basis for the new instrument. The second part contains technical information about the new fast scanning calorimeter developed for isothermal investigation of crystal nucleation and growth in a polymer. The advantages and limitations of the new technique are demonstrated on several examples including investigation of melting and crystallization of metal particles and polymers. The third part deals with results on PCL crystal nucleation and growth kinetics. The comparative analysis of the results is given in the discussion.

2. Literature review

2.1. Polymer crystallization

When cooling a molten material it will either crystallize or vitrify. Avoiding crystallization of different materials like metals and polymers becomes more and more industrially important. For crystallizing polymers the basic physical properties like optical transparency, density, thermal stability and others are strongly dependent on its solidification temperature. Temperature of solidification determines the crystal size and crystallization time. The processes preceding the crystal formation – stabilization of nuclei – is also temperature dependent and often controls the crystallization process.

A theoretical description of nucleation and growth processes was developed at 20-30th of the preceding century by several groups of scientists in Germany (Becker, Döring, Volmer), Russia (Frenkel, Zeldovich), Bulgaria (Stranski, Kaschiew), the United States (Fisher, Turnbull, Reiss) as well as others. It resulted in the derivation of so-called steady-state nucleation rates, the description of non-steady-state nucleation period (starting with the work of Zeldovich and applied later for the first time to crystallization of glass-forming melts by Gutzow and Kashchiev) and the formulation of expressions for the growth rates of the supercritical clusters (for an overview see e.g. [4, 6-7]). In further development, this theory was widely applied to the interpretation of experimental data. Hereby different modifications have been introduced. In particular it was shown that the classical nucleation theory overestimates the work of critical cluster formation and therefore underestimates the nucleation rate. In a variety of cases this property leads to serious deviations between theory and experimental results. It can be overcome, as shown in a series of papers, by accounting for deviations of the bulk properties of the critical clusters as compared to the properties of the evolving macroscopic phase (see [6]). This theory was proved by several experimental works including [8-9]. Other modifications of the classical theory of nucleation and growth are connected with their application to polymer crystallization. Here a variety of different attempts of description have been developed in order to model appropriately the peculiarities of nucleation in such complex systems.

The scheme of polymer crystallization as it is conventionally treated in the theoretical description is shown in Figure 3. Due to highly entangled molecules polymer crystallization proceeds by forming layers of folded molecules separated by amorphous material (for a

review see [10]). These layers called lamellae and they are approximately 10 nm thick and can create three-dimensional structures (spherulite) up to 100 μm and larger in diameter.

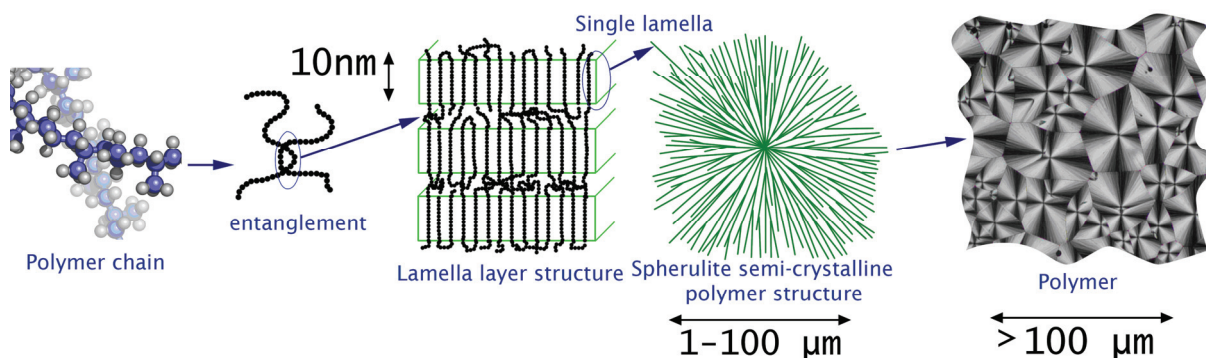


Figure 3. Formation of a polymer semi-crystalline structure. Left - polymer chains, next – spatial confinement of two chains, which results in separation of lamellas by amorphous layers. The lamellae growth from one nucleus can create large spatial structures – spherulite. Last – spherulite in an optical microscopy image.

A widely applied theory of polymer crystallization was proposed by Hoffman Lauritzen, for a review see [11]. The theory is based on classical nucleation and growth theory for small molecule systems. According to this theory, the potential barrier needed for first folding of the first polymer chain in the crystal determines the nucleation rate. Another free energy barrier is due to the folding of successive polymer chains at the growth front of the crystal. This barrier determines the crystal growth rate. The main findings were the prediction of final lamellae thickness and crystal growth rate at particular temperatures. For both of these characteristics the direct dependency on under-cooling below melting temperature was found.

Although qualitatively the description was verified by experimental data, quantitatively the theoretical predictions of lamellar thickness were found to contradict experimental data, for a general overview see [12]. Therefore several extensions of the theory were developed based on the Hoffman-Lauritzen (HL) approach. Three regimes of crystal growth (secondary nucleation) [13] were proposed in order to explain increased growth rate in PE and POM. Sadler and Gilmer developed their own model basing on simulations of the crystal growth front [14].

The HL-theory with its extensions is widely applied nowadays, but two main defects remain to be mentioned. The first one is inability of the theory to describe early stages of

crystallization and the second is inability to explain reorganization processes in already developed lamellae.

Several experimental observations like lamellae thickening and internal structure rearrangement in the crystalline state were used as one of the basic reasons for Strobl's multiphase model of polymer crystallization [15]. Strobl developed a theory of polymer crystallization which is qualitatively different from the classical approach. According to his theory the crystallization of polymers occur in three steps: formation of a mesophase in the melt, stabilization of the mesophase into granules and merging of granules into lamellae.

Several steps of lamellae formation were proposed by Muthukumar [16]. His analysis was based on molecular dynamics simulations of the crystallization process including very early stages. The results were quantitatively different from the predictions made using HL theory. A new model of early stages of crystallization was developed. Schematically it is shown in Figure 4.

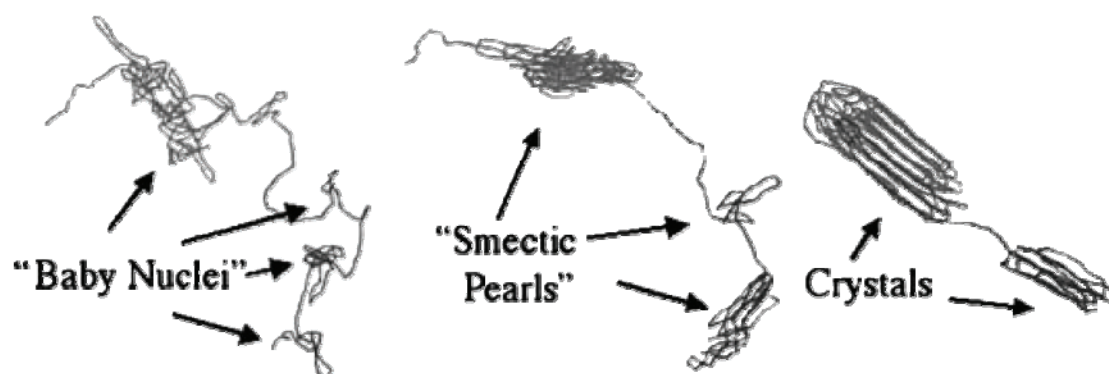


Figure 4. Muthukumar's polymer crystallization model, for review see [16].

According to this model, the first primordial stage of crystallization consists of the growth of density fluctuations and the birth of baby nuclei, which then mature into lamellae passing in its evolution a stage of smectic pearls. As one of the results, a spontaneous selection of finite equilibrium lamellar thickness is addressed in this model. As opposed to small molecule materials, the single polymer chain can participate in several 'baby nuclei'. Some of them will disappear which allow the other to stabilized into 'smectic pearls'. This bonding between nuclei embryos is a specific property of large molecule systems and it should be taken into account for theoretical description of nucleation and overall crystallization kinetics.

Besides homogeneous (bulk) nucleation the crystal formation can be initiated from already existing impurities, interfaces or existing crystals of the material itself (self seeding) – the heterogeneous or catalyzed nucleation.

For a variety of experimental analyses the separate knowledge of nucleation and growth effects is not required but their simultaneous effect resulting in the formation of a certain amount of a crystalline phase which is dependent on time. This is also the basic quantity employed in DSC since it determines the heat release measure in cooling and heating of polymers or other systems capable to crystallize and/or to go over in to the vitreous state. The overall crystallization is usually described using Kolmogorov-Johnson-Mehl-Avrami equation [17] which was independently developed by several authors giving this equation their names. The equation describes transformation of volume of the material by nucleation and a following growth process. According to this theory the volume fraction of a transformed material can be expressed as:

$$x(t) = 1 - \exp(-E(t)) \quad (2.1)$$

Where

$$E(t) = \text{const} \cdot \int_0^t \dot{N}(s) \left[\int_s^t \dot{R}(z) dz \right]^m ds \quad (2.2)$$

Where m – dimensionality of growth, $\dot{N}(t)$ – nucleation rate, $\dot{R}(t)$ – growth rate.

Assuming that nucleation and growth rate are time independent and depends only on temperature, the equation can be simplified to yield

$$\begin{aligned} E(t) &= kt^n \\ 1 - x(t) &= \exp(-kt^n) \end{aligned} \quad (2.3)$$

where $n = m + n_n$ is composed of the dimensionality of growth (m) and nucleation (n_n). Last number is usually equal to one for homogeneous and equal to zero for heterogeneous nucleation, k is a parameter which includes information on nucleation and growth rate, for a recent review see [18]. This simplified version is usually referred to as the Avrami equation. Its extensions to a transient nucleation [8, 19] and non-isothermal crystallization [8, 19] is widely applied by the experimentalists for estimation of the parameters of crystallization kinetics.

The optical observation of nucleation made by most of the authors is not useful for fast crystallizing materials and materials that have no observable crystals, e.g. if they are too small. Several other attempts to observe crystallization including nucleation of crystals were performed. Using scattering techniques Strobl has shown the formation of a meso-phase prior

to crystallization of iPP [20-23]. Hobbs et al. [24] made progress in in-situ AFM imaging. They observed homogeneous nucleation and mesomorphic to α -phase transition in iPP droplets. But this technique can not follow overall nucleation in bulk material and has problems with temperature treatments of the sample. Optical hot stage microscopy is traditionally used for direct observation of crystal front growth. It also allows counting the amount of nuclei created during crystallization. But this method is limited to slowly crystallizing materials with optically distinguishable crystals. Wurm et al. observed a peak in ϵ' prior to crystallization, which was assigned to mobility restricted structures before crystallization [25]. The reorganization of the material even before nucleation was observed e.g. in [26-28] in poly(ethylene terephthalate) PET using small angle X-ray scattering (SAXS) technique. The formation of dens domains before crystal nucleation was observed which supports multi stage crystallization theories like that by Mutukumar [16]. The study was performed in PET at a temperature 5 K above the glass transition temperature, where crystallization is relatively slow. To study crystal nucleation and growth in the full range of temperatures, between glass transition and melting, a much faster technique is required, as will be shown below.

The need of controlled fast cooling techniques for the study of crystallization was realized by Piccarolo et al. in [29]. They developed a device allowing controlled fast cooling of polymer films at cooling rates up to several thousands Kelvin per second. A 100-200 μm thick polymer sample was placed in a copper-beryllium block, molten, and finally cooled in the block by cold water. Temperature was measured by a thermocouple giving information on cooling rate as function of temperature. Different cooling rates can be obtained by varying water flow rate and temperature. Polymer films after temperature treatments can be then investigated using other measurement techniques for study of influence of different cooling.

This controlled cooling technique was used by Androsch et al. for sample preparation for investigation of crystallization of polypropylene and its copolymers [30]. In this work samples were prepared at different cooling rates 10...100 K/s, and investigated using AFM. Polypropylene is known to form spherulitic structures with big crystallites on slow cooling and a nodular structure with small structures after quenching. It was found that the stable α phase can be developed from the mesophase within the nodular structure already in solid state. This shows that this transition was performed without melting of the nodular structure, which supports Strobl's theory of polymer crystallization through a mesophase.

One of the disadvantages of such a study is that the sample has to be moved out of cooling device into the other one for investigation and therefore undergoes an unwanted temperature treatment. For example polypropylene crystallizes at room temperature and can therefore not be kept in the amorphous state. To avoid this one has to perform all studies inside the instrument which performs the heat treatment, like in a calorimeter.

The single sensor ultrafast calorimeter that will be described in details below was used for investigation of isothermal and non-isothermal crystallization of iPP and PVDF [31-32]. Taking advantage of measurement on controlled fast cooling the suppression of crystallization was studied. As known the polymers can also crystallize on heating. If the cooling was fast enough, the polymer does not crystallize, but crystal nucleation is difficult to avoid as far as it is a much faster process. On successive heating - as soon as the mobility of the molecules is high enough - the nuclei grow and the material crystallizes. This process of crystallization on heating is called cold crystallization and is usually faster than crystallization from the melt as more nuclei are created before crystallization. Therefore higher temperature scanning rate is required to avoid crystallization on heating rather than on cooling. The single sensor ultrafast calorimeter was used also to study the reduction and further elimination of crystallization both on cooling and heating.

Possibility to avoid crystallization on cooling allows one the study of isothermal crystallization. Conventional DSC technique is limited by cooling rate to high temperatures where crystallization is slow enough to avoid it on cooling. Figure 5 schematically shows the problem, which appears when crystallization of the polymer is faster than the cooling capability of the device. Most of the possible range of temperatures of crystallization is not accessible (red part) in such situations. Unfortunately most of the industrially important materials are crystallizing faster then conventional techniques are able to cool. Just as shown in Figure 5.

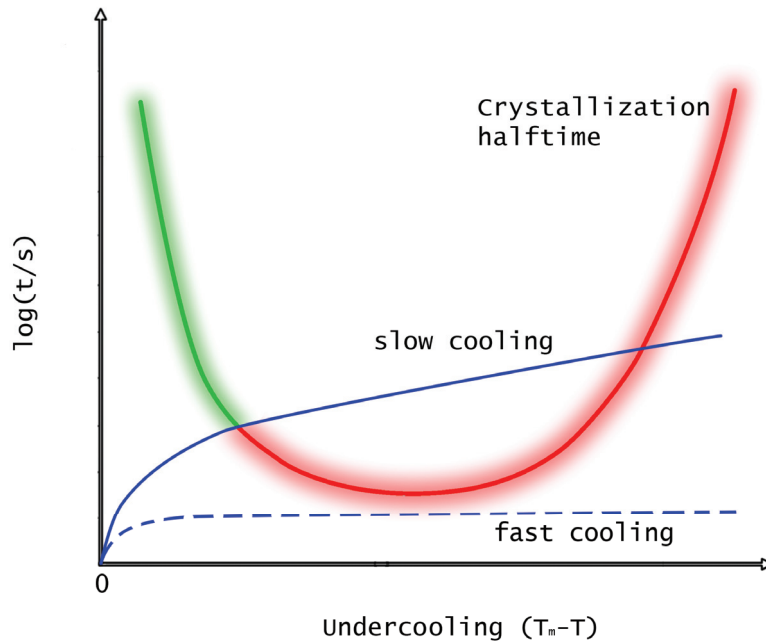


Figure 5. Crystallization halftime and the part of it which is accessible for isothermal investigation after slow cooling (green).

More than that, the low temperature crystallization (larger under-cooling) is of special interest for industry. For example polypropylene in such cases creates a large number of small crystals with dimensions smaller than the wavelength of visible light, which make the material optically transparent. But to study such processes a device is needed, which can perform isothermal measurements just after fast cooling as indicated by the dashed blue curve in Figure 5. For pure isotactic polypropylene (iPP) a cooling rate faster than 600 K/s is needed for that. To improve transparency or some other properties of the final product after crystallization, manufacturers often try to increase crystallization rate by adding nucleating agents, so that more small crystals can grow because of a large number of nuclei. Nucleated iPP crystallization can not be avoided up to cooling rates of several thousands Kelvin per second, depending on the additives. In this case an even faster cooling device is required for isothermal crystallization studies in the full range of possible temperatures.

As was shown already by Piccarolo [29], the decrease of the sample size is critical for fast cooling of the sample. The smaller the sample the smaller temperature gradients inside it and the smaller heat exchange is required on cooling. This argumentation will be used in the description of the fast scanning calorimeter in the following chapter. This calorimeter was successfully used in [31-33] to find the critical cooling rate where the crystallization on cooling can be avoided. It was applied further by De Santis [34-36] for investigation of

isothermal crystallization (Figure 6). The upgraded version of the device was also used to study isothermal crystallization of nucleated iPP (Figure 6).

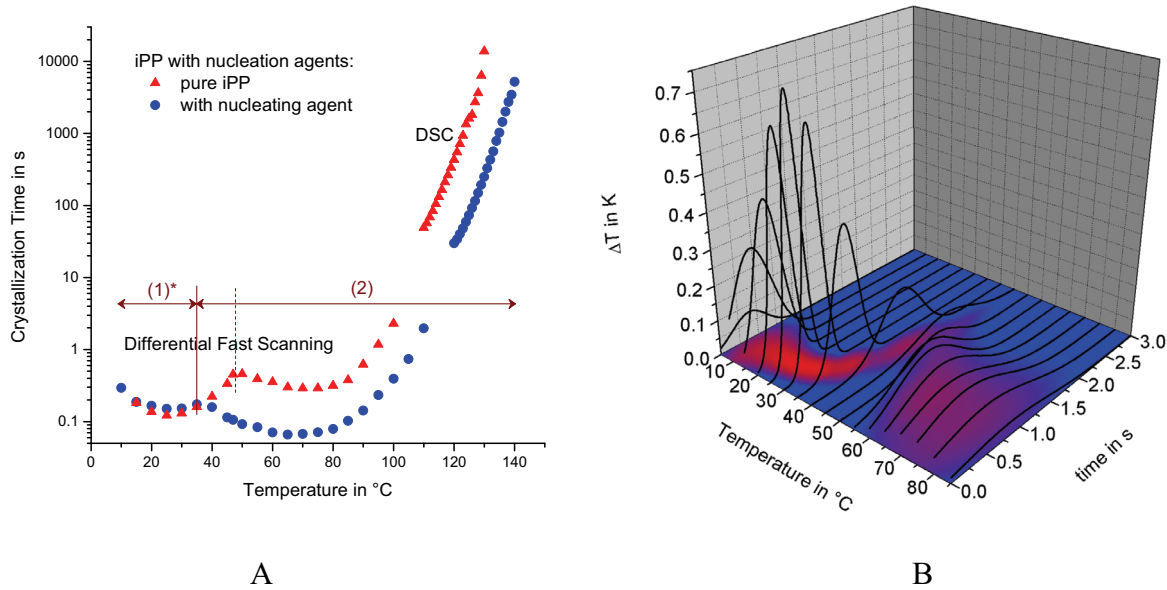


Figure 6. Isothermal crystallization halftime (A) of pure (red dots) and nucleated (blue dots) iPP. The exotherms during crystallization at different temperatures – B. De Santis et al. [34]

Crystallization double kinetics was observed (Figure 6A) which already had been reported before [37] and later by [35-36]. The change in kinetics trend at 45 °C was assigned to a change in nucleation mechanism. At high temperatures heterogeneous nucleation dominates. Whereas at low temperatures homogeneous nucleation becomes dominating. The crystallization exotherm, shown in Figure 6B, reveals significant increase of maximum intensity in this case. This result could be interpreted as an immediately space filling crystallization on a large number of nuclei formed in the bulk material, which is expected for homogeneous nucleation. The observed crystallization kinetics provides interesting information about crystallization and possibly nucleation. Therefore separation of nucleation and growth kinetics would be highly useful.

Common understanding of nucleation and growth kinetics is shown in Figure 7A. Nucleation is a process connected with overcoming of a potential barrier of critical cluster formation. The steady state nucleation rate J can be written as [6]:

$$J = J_0 \exp\left(-\frac{W_c}{k_B T}\right) \quad (2.4)$$

J_0 – prefactor, W_c – work of critical cluster formation, k_B – Boltzmann constant, T – absolute temperature. Which then basing on Gibbs' analysis can be expressed as:

$$J = \sqrt{\frac{\delta}{k_B T}} \left(\frac{D}{d_0^4} \right) \exp \left(-\frac{\Delta G_c}{k_B T} \right) \quad (2.5)$$

σ – specific surface energy or interfacial tension, D – diffusion coefficient, ΔG – change of Gibbs free energy.

Corresponding growth rate is (from [6]):

$$u = f \frac{D}{4d_0} \left[1 - \exp \left(-\frac{\Delta \mu}{k_B T} \right) \right] \quad (2.6)$$

f – numerical factor, D – diffusion coefficient of the ambient phase units, $\Delta \mu$ – difference of the chemical potential per ambient phase unit in the melt and crystal.

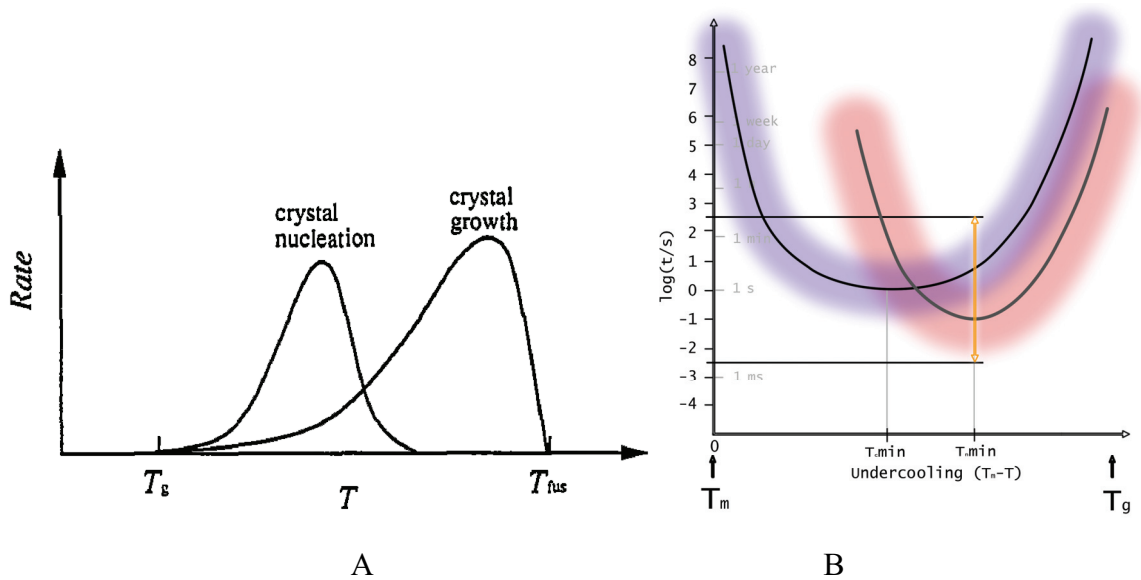


Figure 7. Common representation of crystal nucleation and growth rate taken from [2] (A). Schematic view of nucleation and crystallization kinetics of a fast crystallizing polymer (B).

The two processes can be also represented by their half-times versus undercooling temperature as more demonstrative for explanation of the curse of the experiments.

One of the first separate observations of nucleation rate dependency on temperature was performed by Tammann in 1898 on piperine and glycerol (for review see [38]). The idea

of Tammann's method of observation of nucleus development was accepted and employed by most other investigators at that time. It consists of two steps (Figure 8).

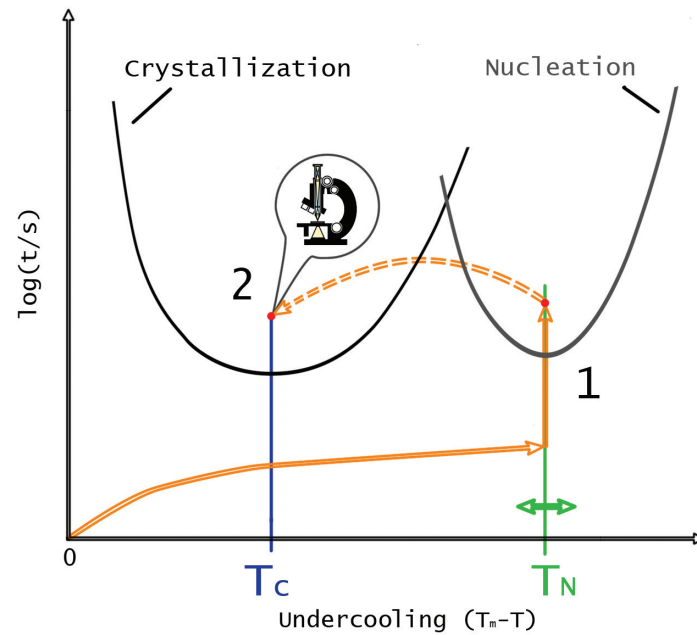


Figure 8. Nucleation kinetics investigation using Tammann's method [38]. Number of nuclei created at temperature T_N can be observed by number of visible crystals, grown at T_C .

First the molten material is annealed at high under-cooling where the nucleation is much faster than crystallization ('1' and T_N in Figure 8). The nuclei created at first step are allowed to grow at higher temperature ('2', T_C in Figure 8) to microscopic observable size. The number of crystals provides some estimation of nuclei formed at T_N and surviving until T_C . Varying temperature T_N one can obtain temperature dependence of nucleation rate. Among limitations of this method is inability to study materials with optically invisible crystals. Another possibility to probe the number of nuclei developed on annealing is a similar calorimetric measurement.

In analogy to Tammann's experiment a calorimetric experiment probing nucleation by crystallization was performed by Oguni [2] and is schematically shown in Figure 9.

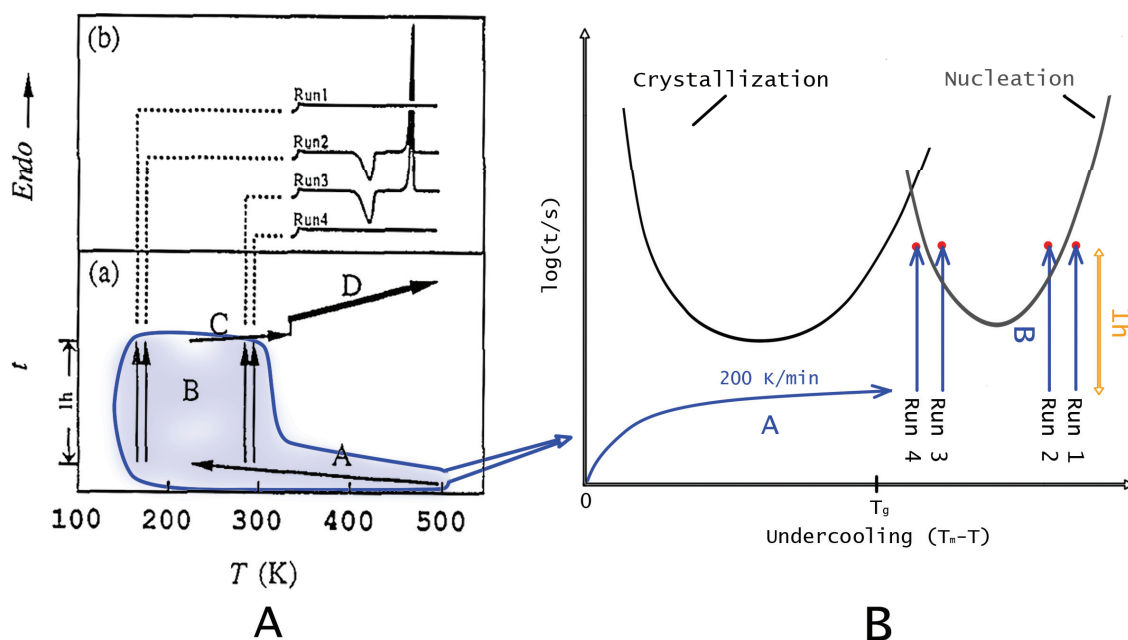


Figure 9. Scheme of DSC annealing experiments on 3,3'-dimethoxy-4,4'-bis(2,2-diphenylvinyl) biphenyl (DMDPVbiphenyl) for determination of nuclei formation below glass transition temperature [2] (A). Representation of annealing step 'A' and 'B' are shown in B, for details see text.

Oguni [2, 39] used the cold crystallization enthalpy as a measure of number of nuclei formed on previous annealing. Due to cooling rate limitation very slowly crystallizing materials were taken to avoid crystallization and nucleation on cooling. It was demonstrated that if one cools fast enough to avoid crystallization and nucleation and performs an annealing step ('A' and 'B' in Figure 9 A) at a certain range of temperatures far below glass transition (between 'Run 2' and 'Run 3'), the cold crystallization peak appears on successive heating after annealing ('D' in Figure 9 A). This was explained by formation of crystal nuclei during annealing, which later on heating allows cold crystallization. The schematic representations of the first two steps ('A' and 'B') of the annealing experiments are shown on Figure 9 B. The sample was cooled at temperatures below glass transition ('Run 1' ... 'Run 2') fast enough to avoid nucleation on cooling (200 K/min). If the annealing temperature would be in between the temperatures of 'Run 2' and 'Run 3', the crystal nuclei were formed on annealing. Thereby on successive heating after annealing (10 K/min) these nuclei grow up and crystallization was observed. If the sample was cooled below the temperature of 'Run 1' or above the temperature of 'Run 4' then the annealing time was not long enough for nuclei formation and on successive heating there was no cold crystallization (Figure 9 A 'Run 1' and 'Run 3').

This method of detection of nucleation by successive heating will be discussed in details below. The possibility of nucleation below glass transition was contradicting classical theory of crystallization, which assumes no diffusion of molecules towards a growing object below glass transition. Therefore another explanation was developed.

In Oguni's theory [40] the nucleation is a process of local rearrangements of the molecules at the border of a nuclei embryo. Therefore nucleation only requires reorientational movement of the molecules accompanied by a small displacement. According to dielectric absorption α -relaxation determines glass transition and β -relaxation – local rearrangements. Therefore Oguni placed nucleation in between α - and β - relaxation, and assumed that it is dominated by the β -relaxation.

The simultaneous observation of both processes of nuclei formation and overall crystallization at the same temperature would allow one a better understanding of them. But for DMDPVdiphenyl nucleation is observed at much lower temperatures in comparison to crystallization. Therefore simultaneous observation below the temperature of 'Run 3' is impossible. At the same time faster crystallizing materials would require faster cooling rate to avoid nucleation on cooling. The Perkin Elmer DSC-7 used by Oguni allowed maximum cooling up to 200 K/min. A newly developed High Performance DSC based on Perkin Elmer DSC was used by Mathot et al. [1] for investigation of nucleation in the same way as Oguni did but for a much faster crystallizing Poly(L-Lactic Acid) (PLLA). But even 10 K/s cooling was not fast enough to fully avoid nucleation. Therefore nucleation kinetics was investigated only partly, and still apart from crystallization. The PLLA crystallization was too slow to be observed at the same temperature where the nuclei formation was detected. The need of investigation of crystal nucleation and growth for one sample implies certain limitations on the material and instrumentation. To study crystal nucleation and growth at one and the same temperature one should perform experiments on much faster crystallizing materials utilizing a much faster technique with a large dynamic range.

The task of my work was therefore to study isothermal nuclei formation and overall crystallization kinetics at one and the same temperature. The detection of nucleation could be performed by observation of cold crystallization on successive heating after annealing following Oguni's and Mathot's work. The study of both of these processes, nucleation and crystallization, at the same temperature requires investigations in the range of temperatures from melting temperature to below glass transition. The chosen model material should be fast enough to allow observation of crystallization even close to glass transition, where the

nucleation is expected to be fastest. On the other hand the chosen model polymer should nucleate and crystallize slowly enough to allow avoiding nucleation on cooling before the measurements.

The experimental technique chosen was fast scanning calorimetry because of its broad dynamic range starting from short enough observation times. The scanning calorimeter also allows controlled temperature treatment of the sample on time scales, which were hardly available in any other experimental technique before. The available fast scanning calorimeters and needed improvements will be discussed in the next chapters.

2.2. Thin film fast scanning calorimetry

The main reason why conventional DSC cannot be used for my task is scanning rate limitation. As was shown in the previous chapter, the materials for which nucleation can be avoided using conventional DSC crystallizes slowly. Therefore simultaneous investigation of nucleation and crystallization at the same temperature is hardly realizable. The first problem of fast temperature control of a polymer sample is the temperature gradient inside the sample due to heat transfer. Therefore the temperature lag inside the sample due to heat conductivity should be minimized. Minimizing of sample mass also reduces the heat flow rate needed to provide or remove from the sample for heating or cooling. This increases maximum possible heating and cooling rate. The cooling of thin polymer foils was performed by Piccarolo et al. [29], which was already mentioned above. But the device was used only for cooling. The sample holder which was used as heat exchanger was much larger than the sample itself. Therefore heating and quantitative measurements were complicated. The improvement of this technique could be made by an improvement of the temperature control and a reduction of the measurement cell addenda heat capacity.

Thin film calorimeters were solution for that. Membrane calorimeter was introduced by Hellman et al. [41]. The thin (180 nm) SiN membrane was used as holder for sample, heater and resistors used for temperature measurement (Figure 10).

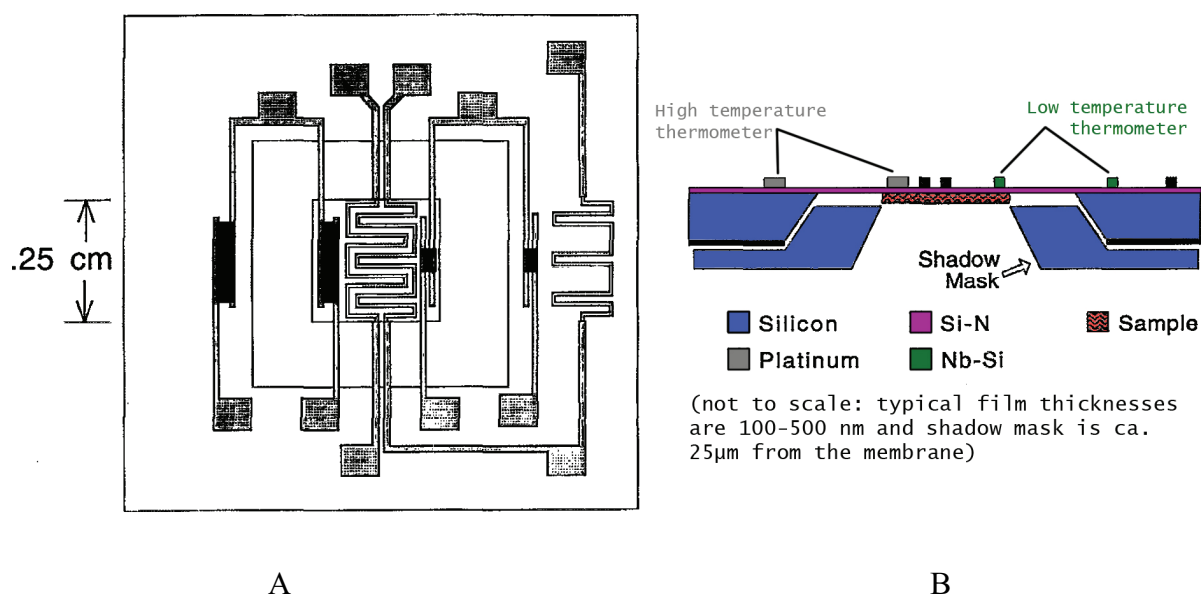


Figure 10. Thin film sensor for calorimetric measurements of microgram samples in wide range of temperatures with low addenda heat capacity of measuring cell developed in the group of F. Hellman [41]. A – planar view, B – cross-section (schematically).

The membrane was placed on a Si frame $1 \cdot 1 \text{ cm}^2$ with a window of $0.5 \cdot 0.5 \text{ cm}^2$ around the measurement area (Figure 10 B). The Si mask window of ca. $0.25 \cdot 0.25 \text{ cm}^2$ was used for low pressure chemical vapor deposition (LPCVD) of sample films of thicknesses 100-500 nm. Addenda heat capacity of measuring cell was several orders of magnitude smaller than conventional calorimeters existing at that time. This allowed heat capacity measurement of samples with a mass of only several micrograms. The sample heat capacity at different temperatures was determined using AC temperature scan technique. The first temperature scan (heating) with similar technique was performed in Allen group as described below.

The same idea of a low addenda heat capacity sensor was used by the group of Allen for a fast heating calorimeter [42]. To improve heating possibilities of the sensor the temperature control elements were reduced to one heater stripe with 4-wire connection for simultaneous heating and temperature determination (Figure 11).

This calorimeter has an even more reduced addenda heat capacity (in a new version only 30 nm membrane thickness [43]) for studying samples of several nanometer thickness on extremely fast heating in vacuum. Introduction of a differential scheme of temperature measurement [43] reduces noise level and simplifies quantitative measurement significantly.

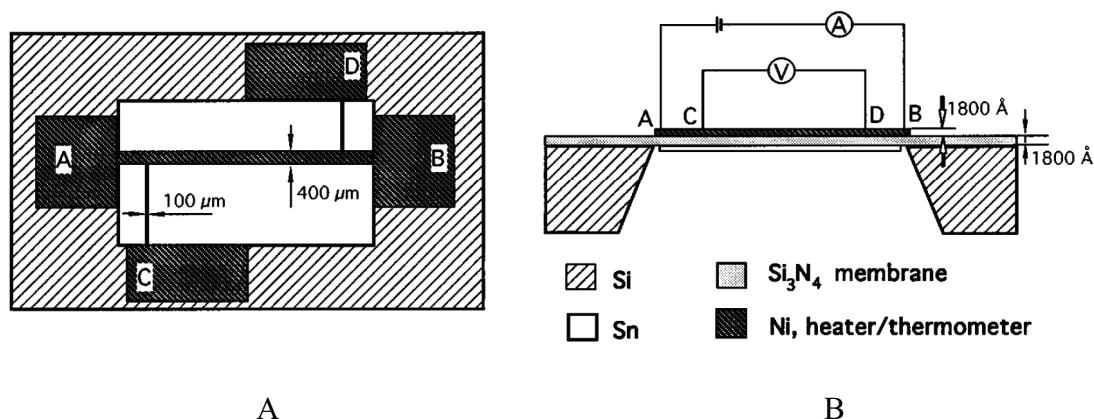


Figure 11. Calorimetric sensor for quasi-adiabatic ultra-fast scanning in the group of L. Allen [42] planar view (A) and cross-section (B).

For the study of crystallization processes the fast heating is not enough – fast cooling is of high interest as well. Firstly to allow one fast cooling it is needed to go to non-adiabatic conditions to allow heat transfer from the sample on cooling. It was shown by Minakov that gas is the best cooling agent for heating-cooling experiments because it is less inert than a solid medium therefore it allows faster reactions on changes of the scanning regime [44]. The membrane sensor appears to be appropriate for fast cooling as well as for fast heating.

Following Allen's ideas, a differential scanning calorimeter was developed in the group of Rodríguez-Viejo [45]. It allows both controlled heating and cooling of microgram samples. While Allen uses quasi-adiabatic conditions for fast heating here the losses through the membrane in vacuum were used for controlled cooling. The general sensor view, schematic cross-section and temperature control scheme are shown in Figure 12.

The digital differential control scheme with power compensation was introduced (Figure 12 C) allowing heating and cooling of microgram sample at rates from 10^{-3} K/s to 1000 K/s. The highest possible scanning rate of this calorimeter is restricted by digital controller speed. Therefore relatively large samples were measured in comparison to the faster scanning device developed by Allen et al. Typical sample thickness varies from 100 nm to 50 μm .

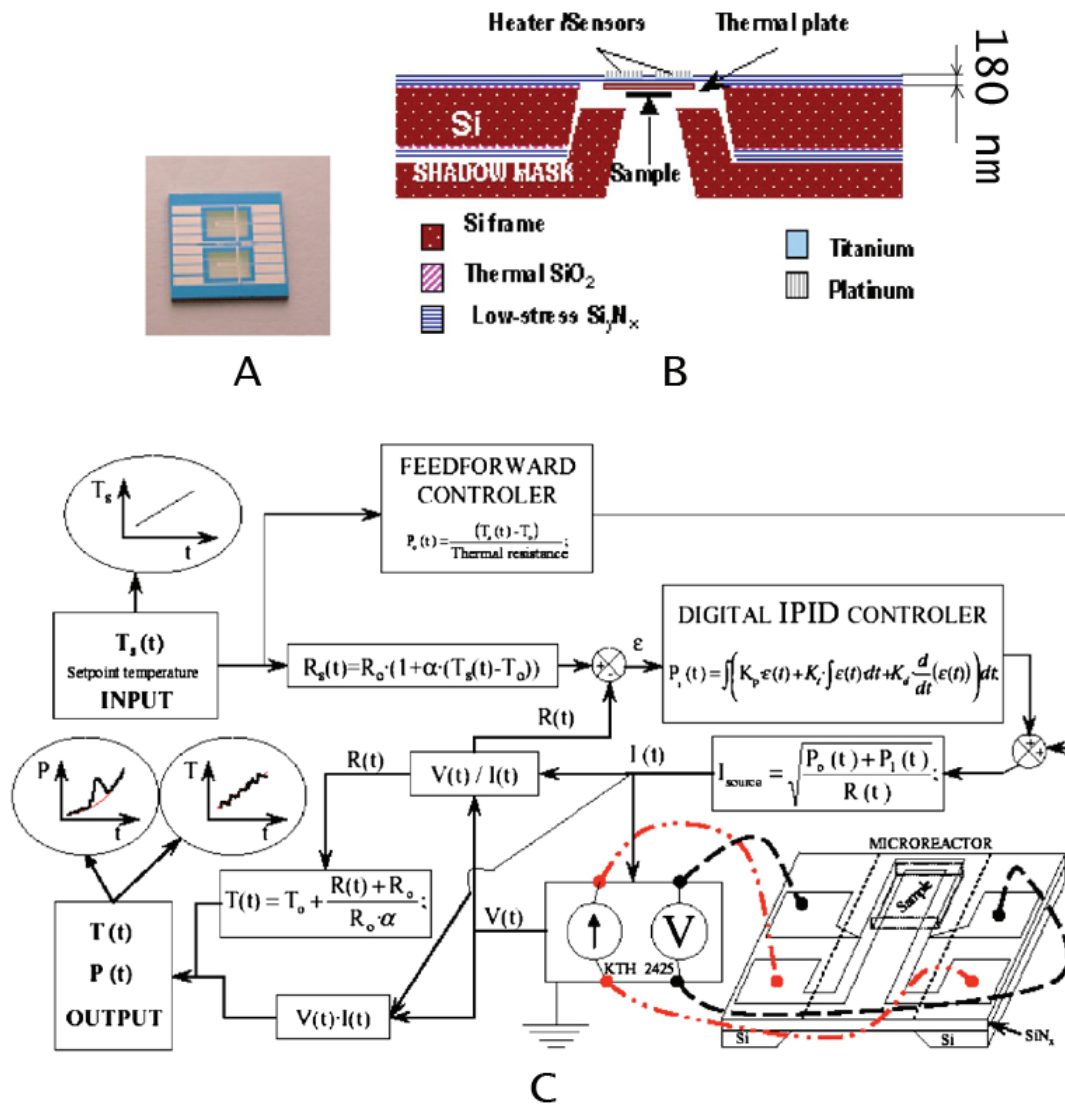


Figure 12. Differential power compensated calorimeter allowing one controlled fast cooling and heating of microgram samples. Developed in the group of Rodríguez-Viejo [45]. A – general view of a pair of sensors, B – schematic cross-section of sensor, C – temperature control and data acquisition scheme.

The differential temperature control scheme with power compensation allowed the sample to follow exactly the required temperature profile, but also causes difficulties. The significant difference in surfaces of sample and empty reference side introduces significant non-linear influence on differential signal. The similar problem will be discussed later for another calorimeter.

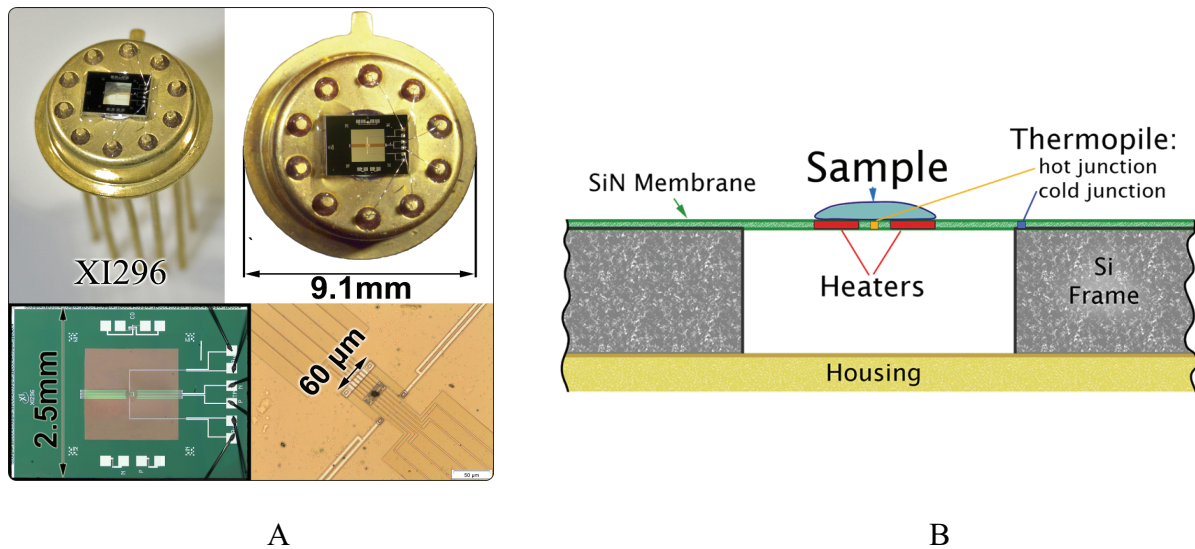


Figure 13. Thin-film calorimetric sensor. Dimensions and comparison of measuring area size with the membrane size (A). Schematic view of sensor and sample placement (B).

Again following Allen et al. another calorimeter for controlled fast cooling was developed [44, 46]. The main ideas of this technique were similar to the previously described: reduction of sample mass, reduction of addenda heat capacity of measuring cell but using gas as a cooling agent. Nevertheless, several significant differences were introduced in sensor construction allowing much higher possible cooling rate.

The commercially available chip sensor that was used is shown in Figure 13. The measuring cell consists of heater stripes and thermopiles embedded into 0.5 μm SiN membrane. The size of the heater area is 60·60 μm vs. 1.2·1.2 mm membrane total size (Figure 13). The size of the sample and addenda heat capacity of the measuring cell (heated area) is the key factor for achievement of controlled high cooling rates.

As was already mentioned above, Minakov et al. [44] has demonstrated that maximum possible scanning rate for performing heating cooling scan at reasonable temperature range depends mainly on density and heat capacity of heat transfer medium. As shown in this paper, assuming ideal heat contact between sample and cooling medium, the maximum possible temperature scanning rate is inversely proportional to density and heat capacity of the cooling agent, and almost does not depend on heat conductivity (as it still exists). The gas even at reduced pressure is the most appropriate cooling agent.

Depending on gas environment the heater on sensor in Figure 13 heats a larger or smaller part of the membrane, measuring therefore different addenda heat capacity. For measurement of very small samples it is important to know this influence. The

temperature distribution across the membrane in helium and nitrogen are shown in Figure 14A [47].

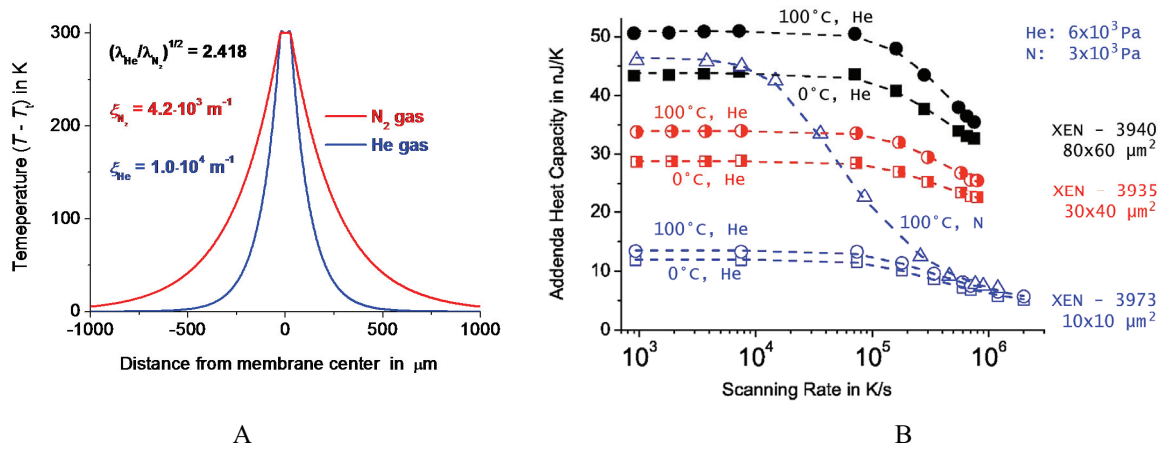


Figure 14. Temperature distribution across the membrane around the measuring area for sensor XEN-3880 – A. Influence of different gases at different pressure on addenda heat capacity of sensors of different types at two temperatures - B [5].

As shown in Figure 14, the use of helium gas instead of nitrogen (air) reduces heated part of the membrane (Figure 14A) and therefore addenda heat capacity (Figure 14B). The information about heating profile of the membrane is important for sample placement. To heat the sample in the most efficient way and avoid temperature gradients inside the sample along the membrane it should cover just the heated area.

The most effective cooling of the sample in gas takes place in case of point-like sample with the distance to cooler much larger then the size of the sample [44]. Assuming a disk-like sample it was shown in the same paper that the maximum cooling rate in this case is depending on sample parameters as follows:

$$\left(\frac{dT}{dt} \right)_{\max} \sim \frac{4\lambda_g(T - T_0)}{r_s d_s \rho_s c_s} \quad (2.7)$$

where λ_g – gas thermal conductivity (e.g. 0.026 W/Km), T – sample temperature, T_0 – thermostat temperature ($(T - T_0) = 500$ K), r_s , d_s , ρ_s and c_s – sample parameters ($\rho_s c_s = 2 \cdot 10^6$ J/Km³). For sample of radius 50 μm, 10 μm height and in air at room temperature, $(dT/dt)_{\max}$ is ca. $5 \cdot 10^4$ K/s.

The disk like shape is more preferable as compared to a spherical one due to a specialty of the heating-cooling mechanism. As seen from Figure 13, the sample is heated from one side and cooled from the other. This results in a temperature gradient inside the

sample that cannot be neglected. The maximum heating rate for the sample with thickness d_s and allowed temperature gradient inside it, δT_s , is [44]:

$$\left(\frac{dT}{dt} \right)_{\max} \sim \frac{\delta T_s \lambda_s}{\rho_s c_s d_s^2} \quad (2.8)$$

For the case of $dT/dt = 5 \cdot 10^3$ K/s and $d_s = 10$ μm , polymer sample ($\rho_s c_s = 2 \cdot 10^6$ J/Km³) the temperature gradient δT_s will be ca. 3 K at the conditions given above. Thus at $5 \cdot 10^4$ K/s the sample thickness should be ca 1 μm for $\delta T_s = 3$ K.

All previous estimations were given assuming ideal heat contact between sample and sensor. In reality, thermal resistance on the membrane-sample interface creates additional temperature difference between surface and sample, thereby reducing maximum possible scanning rate and disturbing temperature calibration. The maximum scanning rate could be reduced for one order of magnitude in addition to previously described limitations [44] as follows:

$$\left(\frac{dT}{dt} \right)_{\max} \sim \frac{\delta T_c}{\rho_s c_s d_s R_c} \quad (2.9)$$

That is proportional to allowed temperature drop between membrane and sample δT_c , heat capacity of the sample c_s , density ρ_s , thickness d_s and thermal resistivity coefficient in W/m²K. Temperature calibration problems will be discussed in more details in the experimental chapter. Especially for spherical or irregularly shaped solid particles heat contact resistance increases significantly in comparison with flat or even better liquid samples. For polymers a simple solution for this problem is to melt it on the sensor before measurement. In this case it either wets the membrane or at least flattens the contact surface. Significant improvement of heat transfer from the heater could be made by using adhesive grease between membrane and the sample.

The maximum controlled cooling rate depends on the temperature interval of interest and oven temperature. The heating-cooling rate possibilities of described above technique with predefined (not active, not differential) temperature control can be observed in Figure 15 for normal size sensor (XI 240, 60·80 μm^2) and average size sample (10 μm in diameter). Even the sample shape is the worst possible from the point of view of heat transfer into the sample and temperature gradients inside it. To improve heat contact small amount of Apiezon grease was used. Air atmosphere at normal pressure was used. The oven temperature is 25 °C.

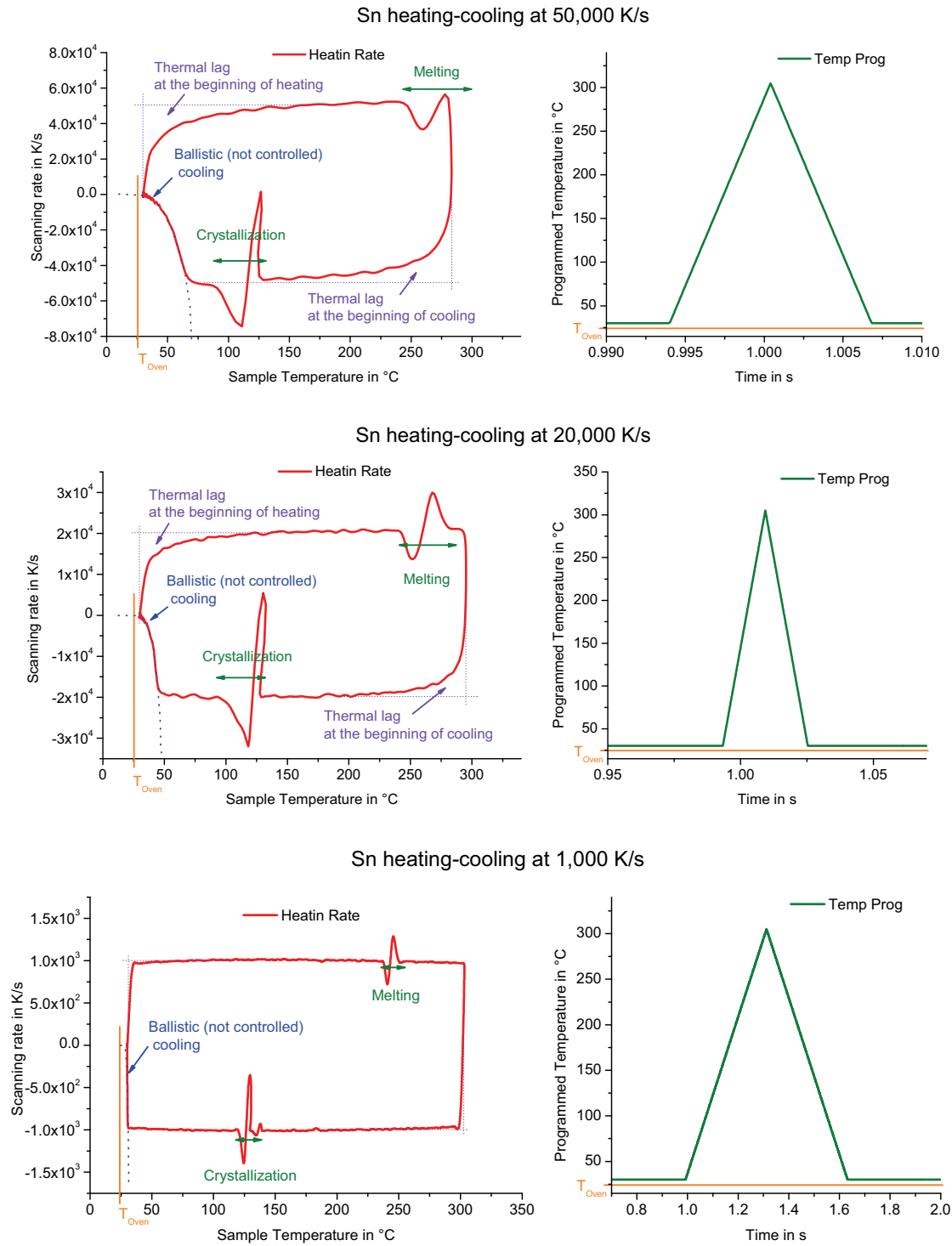


Figure 15. Temperature scanning rate at heating-cooling experiment. Controlled cooling (green) is limited by ballistic cooling (maximum possible cooling rate under existing conditions). Sensor: XI-240 (XEN-3940), sample – Sn sphere ca. 10 μm in diameter.

At highest rate – $5 \cdot 10^4$ K/s the beginning of heating and cooling is smeared due to relatively big heat capacity of the sample plus sensor system and thermal lag inside it and in

between them. To improve performance at higher rates the smaller sensor and sample should be used (e.g. XEN-3973 and $\varnothing 1\text{-}5\text{ }\mu\text{m}$ particle).

The maximum cooling possibility of the surrounding gas can be probed at the end of cooling, close to oven temperature – where cooling occurs without any power provided to the heaters – so-called ballistic, or free cooling. This effect could be reduced by measuring far above oven temperature and in the reduced pressure helium atmosphere.

At lower scanning rates both problems are reduced to nothing and the temperature is almost fully controlled. The control is absent in the areas of phase transitions. The disadvantage of predefined temperature control used in single sensor device is that the device does not ‘know’ about temperature changes on the sensor and cannot actively compensate it. Therefore oscillations during melting and crystallization are observed.

The principal scheme of the calorimeter is shown on Figure 16A. The temperature profile programmed by the user is recalculated into voltage using a calibration function and generated via IC1. The calibration procedure is described in [48]. The heater power and sample temperature are collected via IC2-4.

Applying power P_0 to the heater the sensor heat balance equation becomes

$$(C + C_0) \left(\frac{dT}{dt} \right) = P_0 - \xi(T(t) - T_0) \quad (2.10)$$

where C_0 - cell addenda heat capacity, C - sample heat capacity and $\xi(T(t) - T_0)$ - losses to the surrounding. C_0 is determined from the measurement of the empty sensor. The losses can be determined from a symmetric heating-cooling scan at the same rate. It is assumed to be the symmetry line between heating and cooling electrical power, which is proportional to heat flow. Typical measurement results using this setup are shown on Figure 16B.

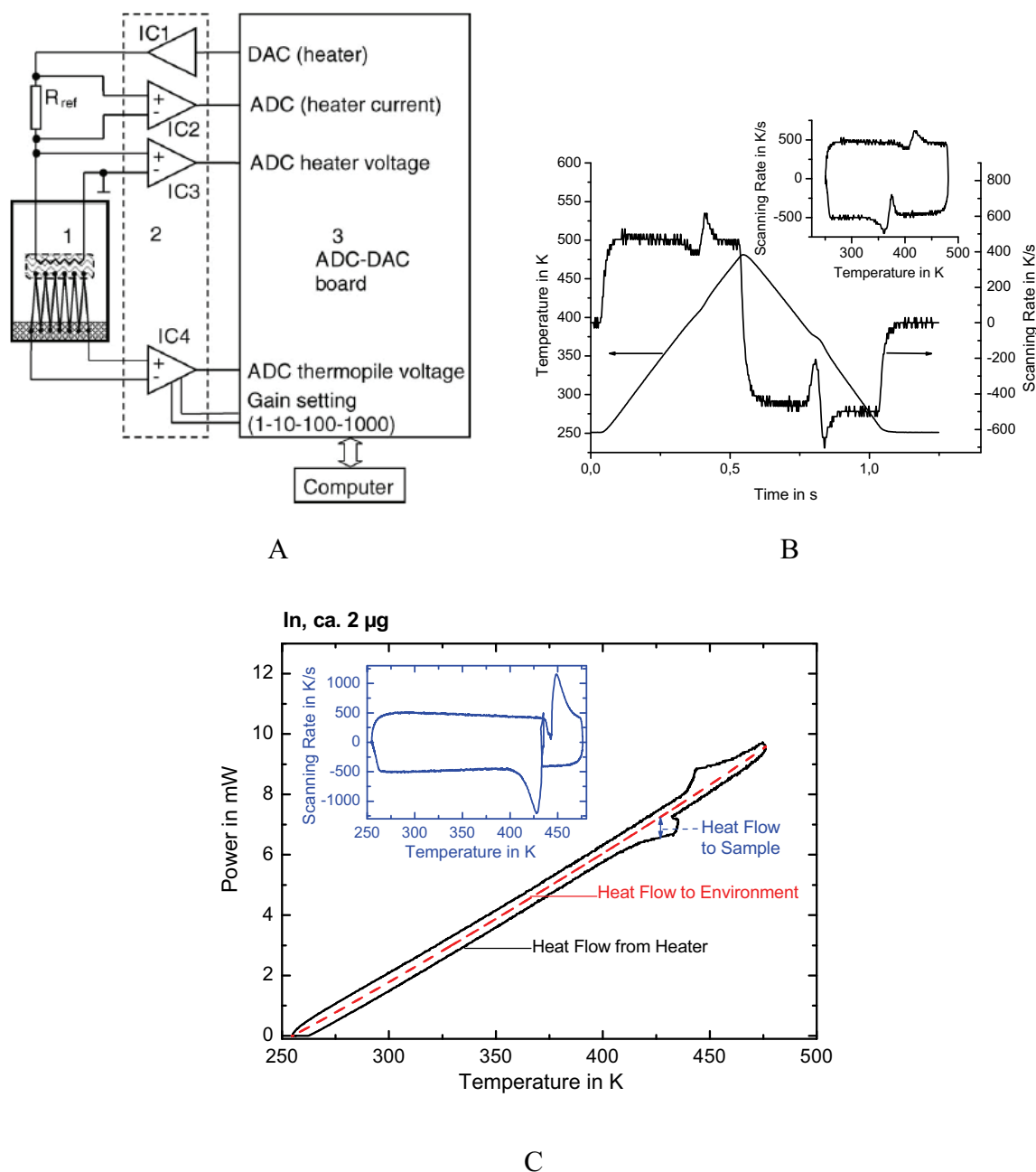


Figure 16. Single sensor setup principle scheme (A) [44]. Heating-cooling scan at 500 K/s of sensor with ca. 120 ng PE (B) [48]. Loss function ($\xi(T(t)-T_0)$) determination - C

This single sensor ultra-fast scanning device [5] was successfully applied for the investigation of polymer melting and crystallization. The reorganization kinetics in PET and iPS was studied in combination with conventional DSC at scanning rates covering 8 orders of magnitude [49-51]. Isothermal and non-isothermal crystallization and the formation of different crystal polymorphs were studied in a wide range of temperatures and scanning rates applying DSC and the fast scanning setup in PE, iPP and PVDF [31-36, 48, 52-53]. The

complex behavior in the temperature range between glass transition and melting temperature was investigated in PBT [54]. The crystallization and cold crystallization suppression in PA6 confined to droplets and in the bulk was studied using such fast scanning calorimeter [55]. The dynamic range of scanning rates of the device allowed the investigation of superheating in linear polymers like iPS, PET, PBT and iPP [56-57].

The examples given above have shown that the effective range of controlled heating and cooling rates using different sensors [58] is $100 \dots 10^6$ K/s. Unfortunately, at low rates signal to noise ratio and therefore sensitivity is reduced. Usually the device is limited to rates above 100 K/s. Nevertheless, the scanning rate range between conventional DSC and this technique - the range $10 \dots 100$ K/s - is of high interest because several material processing steps are applying cooling rates just in this range [29, 59].

The thin-film calorimeter has a better cooling possibility, but needs better control scheme and ability of quantitative measurements. Differential temperature control with active power compensation has been successfully used in Perkin Elmer DSC since 1964 [60].

A similar temperature control scheme was first introduced in thin film calorimeter by Rodri'guez-Viejo [61]. The main idea was to compensate the temperature difference between the sensor with sample and the empty one by adding power to the sample side and removing the same amount from the reference side. The scheme works relatively well for heating rates up to 1000 K/s, but has several limitations. Due to the digital compensation the scheme is not fast enough for events like melting. More importantly, because of the large sensor area the difference in heat losses between both sensors are not easy to take into account and the sensor is not able to cool fast enough due to relatively large area, as well as sample and measuring cell mass.

All these fast scanning calorimeters and control schemes were finally taken as a basis for a new device for fast cooling for the study of nucleation and crystallization kinetics, which will be described below.

3. Fast scanning differential calorimeter with power compensation

3.1. Issues of single sensor calorimeter

In order to improve fast scanning nano-calorimetry the very successfully applied single sensor device as described above and in [5, 44, 48, 62-63] was therefore first analyzed and the weak points were identified.

- The first problem is the non-interactive temperature control, which is based on a predefined voltage-time profile yielding an essentially linear temperature increase of the sensor. But the needed voltage is only known for the empty sensor but not for the sample loaded one. Therefore the voltage profile should be corrected for each experiment by making at least one test scan with the sample under investigation [48]. This excludes the application to "first scans", which are often needed if the influence of the sample history is of particular interest.
- Another problem is the sample temperature discontinuity at phase transitions. Even if a preliminary scan was performed to adjust the voltage profile for linear heating and cooling, the scanning rate during sharp transitions may significantly deviate from the programmed value. This results in smearing and inaccuracy of heat capacity and enthalpy determination. Similar problems exist for the adiabatic fast scanning devices [64].
- The main problem for heat capacity determination for the non-adiabatic single sensor device is the subtraction of the heat loss function. It is realized as a subtraction of a 3rd to 5th order polynomial function [48] providing C_p values symmetric around zero, but as soon as we have several sharp events in the sample, the error in determination of the loss polynomial increases dramatically (see Figure 17).

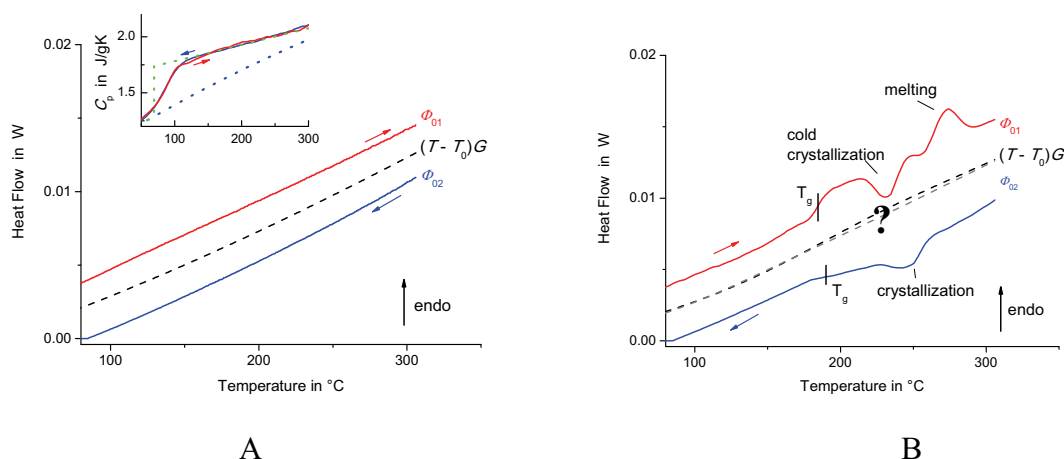


Figure 17. Heat losses curve $(T-T_0)G$ determination for C_p recalculation of PET sample (A). Problems of heat losses determination in case of “overlapping” of different events in the sample during heating and cooling (B).

A differential power compensated fast scanning calorimeter was set up to overcome these problems at least in part. It covers the scanning rate range between 1 and 10^5 K/s in heating and cooling. The device uses the same low addenda heat capacity sensors [58] as previously used for the single sensor device [5, 47-48]. The presence of an empty reference sensor reduces the influence of heat losses and addenda heat capacity on the obtained data. For a better sample temperature control, particularly in the transition regions, a power compensation was introduced, following the work by Rodríguez-Viejo and co-workers [45, 65] and Merzlyakov [66]. To improve signal to noise ratio and resolution of the device even under fast scanning conditions an analog power compensation technique was implemented. A differential power compensation scheme provides, under the conditions of ideal symmetry of both sensors, directly the heat flow rate into the sample, which simplifies heat capacity calculation. Furthermore, user-friendly experiment management software and software package for data evaluation were developed. This device including control and data treatment algorithms, and measurements of metal samples on melting and solidification are presented finally to demonstrate the benefits of the instrument.

3.2. Differential temperature control scheme with power compensation

The developed instrument is intended to measure heat flow rate into the sample as the power difference between an empty and a sample loaded sensor during fast temperature scans on heating and cooling at controlled rate. Finally, the obtained heat flow rate should be recalculated into heat capacity [67-68].

A very successful version of a power compensation differential scanning calorimeter was realized by PerkinElmer [60, 69-70]. It is based on the measurement of the energy difference required to keep both sides, sample and reference, at the same temperature throughout the analysis. When an endothermic transition occurs, the energy absorbed by the sample is compensated by an increased energy input to the sample side to maintain the temperature balance. Because of this energy input, under the assumption of a perfectly symmetric measuring system, is precisely equivalent in magnitude to the energy absorbed in the transition, a recording of this balancing energy yields a direct calorimetric measurement of the energy of the transition. The block diagram of the PE power compensation DSC is shown in Figure 18. It consists of two separate control loops: one for the control of the average temperature of both cups, the second for the control of the temperature difference between the cups.

The average controller compares the arithmetic average of sample and reference temperature with the program temperature. In case of a deviation the average controller corrects the electrical power to both cups accordingly. Due to the feedback the difference between measured average temperature and program temperature is minimized. If the temperature called for by the programmer is greater than the average temperature of sample and reference holders, more power will be fed to both heaters which, like the thermometers are embedded in the cups to realize a short response time of the whole system.

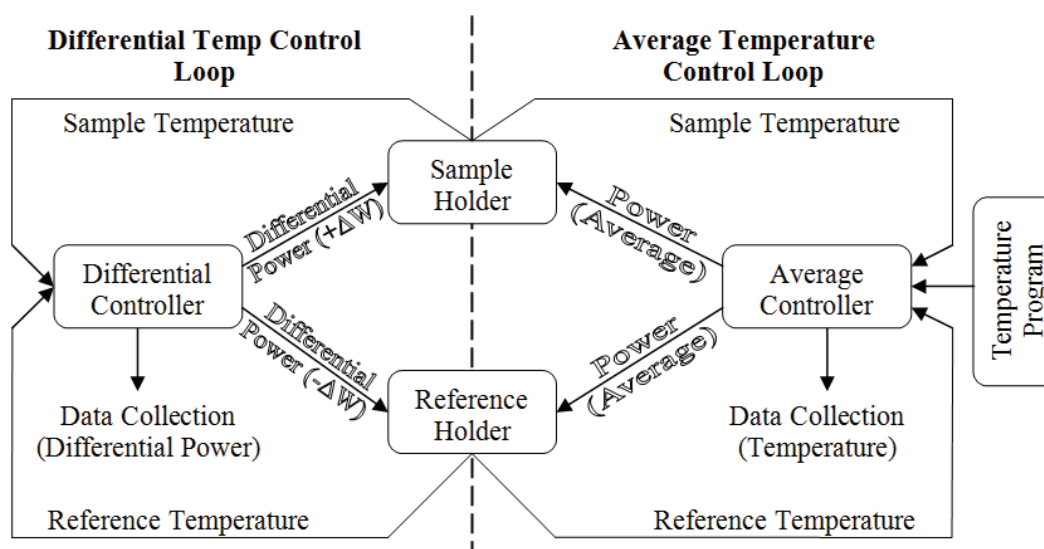


Figure 18. Perkin Elmer power compensation scheme: the average temperature controller makes both sensors to follow programmed temperature. The differential controller compensates the heat flow due to events in the sample and asymmetries. Symmetric compensation on reference and sample side simplifies computation of heat flow to the sample which was critical for that time when computers were not yet available [60, 69-71].

The second controller measures the temperature difference between both cups. Signals representing the sample and reference temperatures, measured by the platinum thermometers, are fed to the differential temperature amplifier. The differential temperature amplifier output will then adjust the power difference fed to the reference and sample heaters in the direction and magnitude necessary to correct any temperature difference between them. In case of a lower temperature of the sample cup, e.g. due to an endothermic transition, an additional power is added to the sample cup. In order to minimize the difference most effectively and to keep a strict symmetry of the measuring system the same power is subtracted on the reference side. Consequently, the heat of transition is not provided by the differential controller but by the average controller keeping the average temperature following the program temperature. The remaining temperature difference between both cups, which is proportional to the power difference [60, 69-71] is recorded, and together with the average temperature profile it provides the complete information about the heat flow rate to the sample.

This scheme proves itself in PerkinElmer DSC calorimeters working up to 10 K/s scanning rate with milligram samples. In conclusion in the PE differential power compensation DSC, the additional heat needed (or released) during an endothermic (exothermic) event in the sample, and is finally provided by the average controller because the

differential controller does not add or remove heat from the system due to his symmetric operation. This scheme allows for a relatively simple determination of the heat flow difference from the remaining temperature difference between sample and reference cups [60, 69], and is not required to measure multiple signals or computing capabilities, but in this case both controllers must be fast to avoid deviations from the programmed temperature. Therefore, it is common practice to use proportional controllers for average as well as differential loop.

Once we want to go to a higher rates and sensitivity we are confronted with the problem of controller performance limitations. This is because the differential signal can contain fast events from the nanogram samples, which requires fast response of the controllers. Time resolution for the control of the average temperature could be much slower if the fast sample events would not be included. Output power range (dynamics) of the average controller is by orders of magnitude larger than needed for the compensation of the sample related effects. Therefore it may be beneficial to separate average and difference control totally avoiding any cross-talk between both control loops.

Following this idea we have developed a new power compensation scheme to realize such separate control loops as shown in Figure 19 [72]. First, we measure and control reference sensors' temperature alone. No average temperature is used. There is no influence of any, even very strong events occurring in the sample sensor on the reference temperature controller. This allows us to use a relatively slow but precise PID controller for the reference temperature control. The integral part of the controller assures that the difference between program temperature and reference temperature is practically zero. Applying the output voltage of the PID also to the sample sensor heater yields nearly the same temperature profile in the sample sensor as in the reference sensor if a high symmetry between reference and sample sensor is realized. Next, the differential controller detects any difference between reference and sample sensor temperatures and adds or subtracts its output voltage to the PID output voltage to the sample sensor alone. In this way a total separation between both controllers is realized. It allows us to use a precisely but relatively slow working PID controller for the control of the reference temperature and a high sensitive and fast proportional controller for the difference controller.

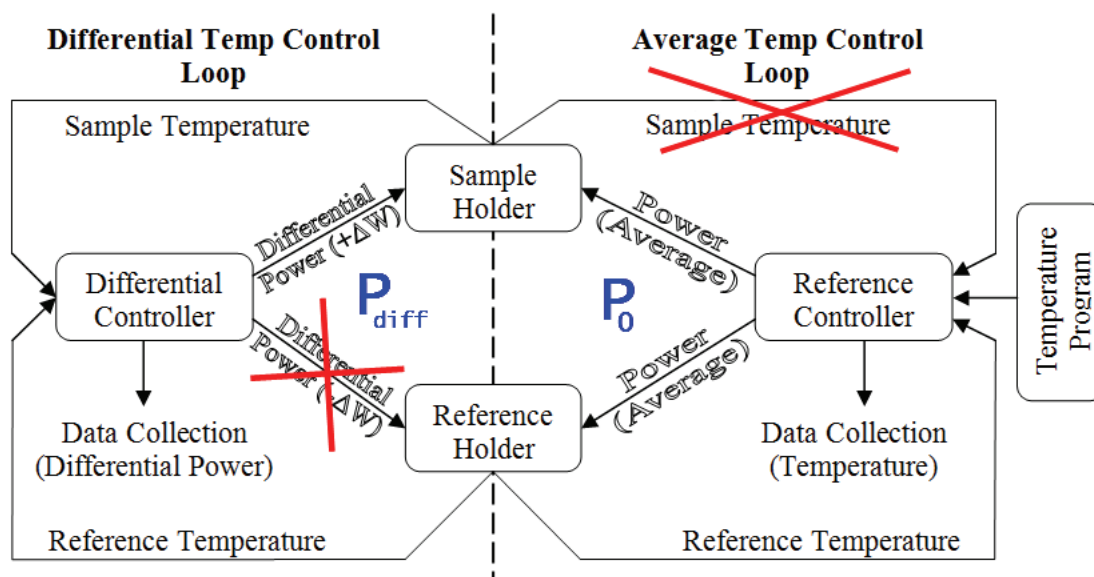


Figure 19. Modified power compensation scheme for operation at high scanning rates: separation of average temperature control (slow changes, large dynamic range) and differential control (fast events, small dynamic range).

Compared to the PerkinElmer power compensation scheme this method allows us a more precise control of the temperature of both sensors, but the proportionality between the remaining temperature difference in the differential control loop and the differential heat flow rate is lost. Therefore the new scheme requires the measurement of more than only one signal to allow us a recalculation of the power difference as it is described below.

The user defined experimental time-temperature profile is recalculated into voltage and provided as the set-point for the PID controller. The PID controller makes the temperature of the reference sensor to follow the experimental profile by adjusting power P_0 to its heater. The same power P_0 is applied to the sample loaded sensor. The difference between the temperatures of reference and sample side is minimized by the differential controller by adding power P_{diff} to the sample side.

The resistive film-heaters of the sensors, ca. 1 k Ω , provide the power, which is supplied to the membrane/sample interface and propagates through the sample, membrane and the ambient gas. For a perfectly power compensated system power is distributed in a way that both sensors are always at the same temperature, T , and scanned at the programmed rate, dT/dt , independent of any heat effect in the sample. Assuming such an ideally symmetric differential system, which means equal addenda heat capacities C_0 on both sides and equal

heat losses $P_{loss}(T)$ to the surrounding on both sides. The heat balance equations for both sensors are as follows:

$$\text{reference:} \quad C_0(T) \frac{dT}{dt} = P_0(T) - P_{loss}(T) \quad (3.1)$$

$$\text{sample:} \quad (C_0(T) + C(T)) \frac{dT}{dt} = P_0(T) + P_{diff}(T) - P_{loss}(T) \quad (3.2)$$

where C is sample heat capacity. In this particular case the difference between equations (3.1) and (3.2) yields

$$C(T) \frac{dT}{dt} = P_{diff}(T) \quad (3.3)$$

where P_{diff} is the difference between the power supplied to the sample and the reference sensors. Consequently, the aim was to set up a system with near to perfect power compensation, which allows one the determination of $P_{diff}(T)$ and finally to correct for the effect of unavoidable asymmetries between both sides in real measurements at high scanning rates.

The hardware was designed for that aim having in mind anticipated scanning rates of up to 100,000 K/s and response times of a few milliseconds. The differential controller, see Figure 20 below, was therefore realized as proportional controller to make it as fast as possible. Amplifiers with adjustable gain settings (X2 and X4[#]) were used for that purpose. The gain is always set to the maximum value, which still damps self-oscillations in the circuit. Analog devices were used in the scheme to shorten response time and therefore allow us high rate temperature processing.

Power difference and all voltages needed for calculation are collected by the computer using a fast ADC/DAC board from Meilhaus [73]. A SRS Small Instrumentation Module analog device frame allows us to control almost all parameters of the amplifiers from the computer. The program for managing the experiment and data collection is written in LabView™ graphical programming language version 8.6.

[#] In the following X1, X2, X3, X4 and PID refer to the particular amplifiers in Figure 20.

The separation of the two control loops makes recalculation of sample heat capacity more difficult in comparison to the symmetric power compensation scheme as it is used in the PerkinElmer power compensation DSC, but allows us going over to higher rates with reliable average temperature control as shown below. Derivation of heat capacity out of the measured signals consists of several steps. First is the determination of heat flow rate into the sample. It will be discussed in the next chapter.

3.3. Electric scheme and power difference determination

The principal electric scheme of the device and the collected signals needed for power difference determination are shown in Figure 20.

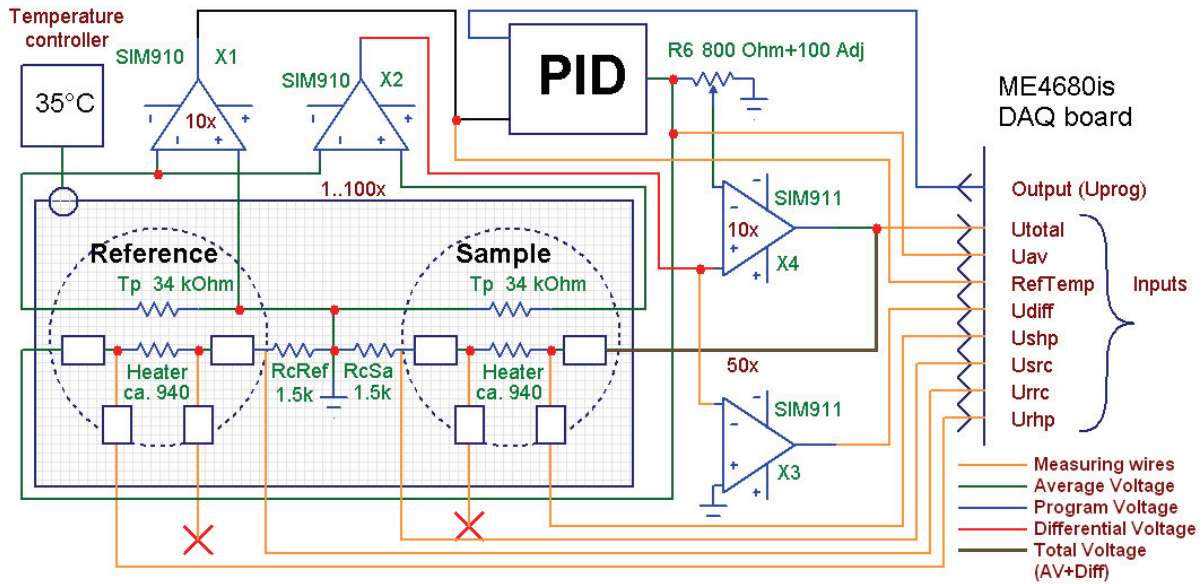


Figure 20. Scheme of differential fast scanning calorimeter with power compensation. All needed voltages for power difference and sample temperature determination are shown by orange (thin light) wires.

The power difference which we want to know is as follows:

$$P_{diff}(T) = \frac{(U_{sample}^h)^2}{R_{sample}^h} - \frac{(U_{ref}^h)^2}{R_{ref}^h} \quad (3.4)$$

where U_{sample}^h and U_{ref}^h are the voltage drops across sample and reference side heaters and R_{sample}^h and R_{ref}^h are their resistances, respectively. To avoid overloading the equations we do

not indicate the temperature dependence of the quantities used in equations (3.4) - (3.11), except the final result, $P_{diff}(T)$. From the single sensor device [48] we know that the maximum power needed to heat a XI-320 sensor loaded with a 20 ng polymer sample at 1000 K/s to 300 K above the ambient temperature is of the order of 40 mW. The power difference $P_{diff}(T)$ we are interested in is only a few μ W. Even the voltages and resistances needed could be determined from the quantities measured according to Figure 20, the problem arises that we are looking for a small difference between two large signals. Consequently, the differential signal will be rather noisy. Therefore the direct subtraction of power on both heaters was not used. Instead the small unavoidable remaining temperature difference of the proportional controller, which determines the power difference, was used. For that the sample side voltage can be written as the sum of the differential and the average part

$$U_{sample}^h = (U_{sample}^h)_{diff} + (U_{sample}^h)_{av} \quad (3.5)$$

where the summing is performed by X4. This yields:

$$P_{diff}(T) = \frac{\left((U_{sample}^h)_{diff} + (U_{sample}^h)_{av}\right)^2}{R_{sample}^h} - \frac{(U_{ref}^h)^2}{R_{ref}^h} \quad (3.6)$$

$$P_{diff}(T) = \frac{\left((U_{sample}^h)_{diff}\right)^2}{R_{sample}^h} + \frac{2(U_{sample}^h)_{diff}(U_{sample}^h)_{av}}{R_{sample}^h} + \left(\frac{\left((U_{sample}^h)_{av}\right)^2}{R_{sample}^h} - \frac{(U_{ref}^h)^2}{R_{ref}^h}\right)$$

where the last two terms in the bracket are the average powers P_0^{sample} and P_0^{ref} provided to sample and reference side by the PID controller, respectively, and

$$P_{assym} = \left(\frac{\left((U_{sample}^h)_{av}\right)^2}{R_{sample}^h} - \frac{(U_{ref}^h)^2}{R_{ref}^h}\right) \quad (3.7)$$

describes the asymmetry of power distribution from the PID between both sensors, which mainly depends on the differences in their resistances. To artificially modify P_{assym} the adjustable divider R6 was introduced before the summing amplifier X4. It can be used to correct for large asymmetries between both sensors, e.g. due to large sample surface area.

To calculate the power difference:

$$P_{diff}(T) = \frac{\left((U_{sample}^h)_{diff}\right)^2}{R_{sample}^h} + \frac{2(U_{sample}^h)_{diff}(U_{sample}^h)_{av}}{R_{sample}^h} + P_{assym} \quad (3.8)$$

heater voltages and resistances are required to be expressed via probed voltages. For determination of sample heater resistance precise high stable constant resistors (R_{cSa} , R_{cRef}) were used for the electric current measurements. To compensate the unknown wiring resistances (including wires on the sensor membrane) a 3-point probe resistance measurement was used assuming symmetric wiring. Resistance can be expressed via probed voltages as:

$$R_{sample}^h = R_C \frac{2U_{shp} - U_{src}}{U_{total} - U_{src}} \quad (3.9)$$

where R_C is the resistance of constant resistor, U_{shp} is the voltage at sample heater (3rd wire), U_{src} is the voltage drop at constant resistor and U_{total} is the total voltage across sample side (probed at the output of X4).

Knowing the resistance of the heater and all other components of the circuit we can define the ratios between the voltage drops on the heater and the measured signals $(U_{sample}^h)_{diff}/U_{diff}$ and $(U_{sample}^h)_{av}/(U_{total} - U_{diff})$, where U_{diff} is the differential voltage after amplifier X2 (probed through X3). Introducing

$$\alpha = \frac{(2U_{shp} - U_{src})}{U_{total}} \quad (3.10)$$

yields for the heater voltages $(U_{sample}^h)_{diff} = \alpha U_{diff}$ and $(U_{sample}^h)_{av} = \alpha (U_{total} - U_{diff})$ and with equation (3.8):

$$P_{diff} = \alpha^2 \left(\frac{(U_{diff})^2}{R_{sample}^h} + \frac{2U_{diff}(U_{total} - U_{diff})}{R_{sample}^h} \right) + P_{assym} \quad (3.11)$$

This will be later on used for the determination of the heat flow rate into the sample.

3.4. Hardware and software realization

The setup consists of thermostat, control electronics, ADC/DAC converter, computer and software package as schematically shown in Figure 21.

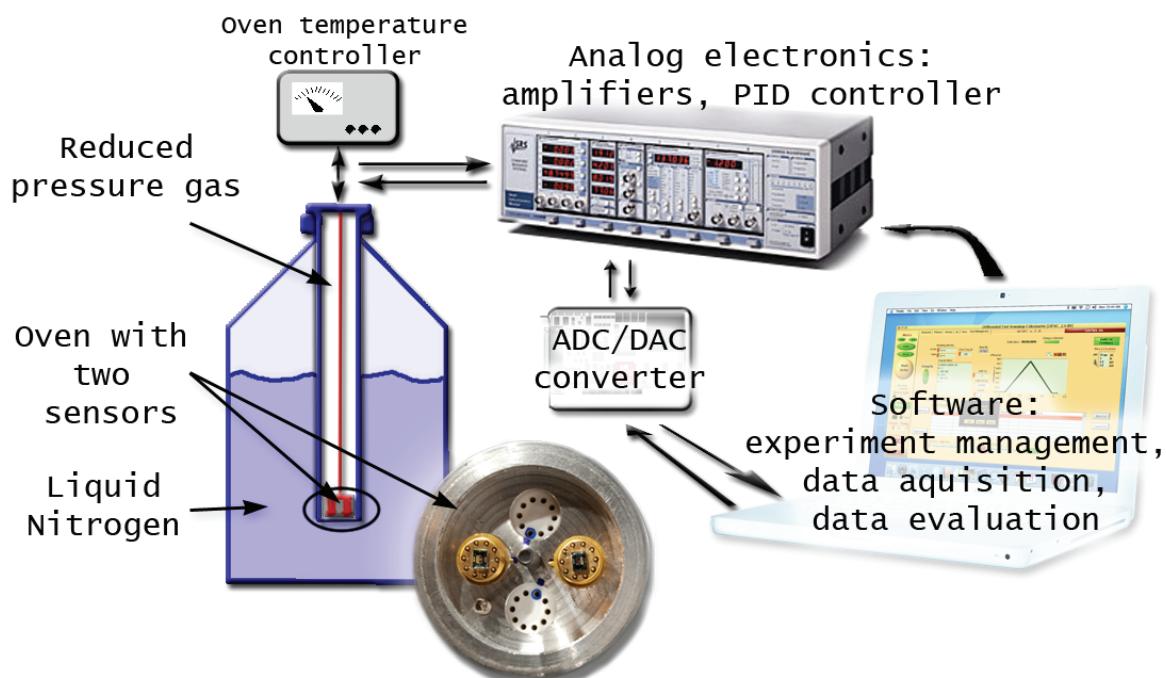


Figure 21. The Fast Scanning Calorimeter setup. Sensors are placed in an oven at the bottom of a tube in a (reduced pressure) gas environment. Heaters and thermopiles are connected to analog electronic devices. The electronics is driven from a computer by a fast ADC/DAC board (temperature set-point determination and data collection). The electronic devices are controlled by software which is also used for data collection/evaluation.

The cryostat was originally developed for an AC-calorimeter [44] and used for the single sensor fast scanning chip calorimeter [74]. It was further developed for differential AC-chip-calorimeters [75] and adapted for the fast scanning chip calorimeter described here. Both calorimeters, AC and fast scanning, are planned to be integrated and used complementary on the same sample in future.

At the bottom part of the tube is an oven with two chip sensors inside, which is kept at constant controlled temperature. The tube can be pumped and refilled with nitrogen or helium at controlled pressure (preferable 50 kPa [44]). To allow one heating of the sample from low temperatures the tube can be placed into liquid nitrogen. Therefore it should be long enough

and has to have thin walls preventing heat transfer in axial direction. This way a very effective, low liquid nitrogen consuming cryostat is realized.

Electronics

The realization of the above described scheme for scanning rates of several thousand Kelvin per second requires appropriate fast electronics. Thus it was decided to use analog amplifiers and a PID controller. Stanford Research Systems (SRS) Small Instrumentation Modules (SIM) [76] were used for that purpose. It is ready-to-use system with adjustable parameters and PC communication interface.

The signals from thermopiles are going to fast analog amplifiers with high input impedance (100 M Ω , 35 pF) and 1 MHz bandwidth (X1, X2). The amplifier (SIM 910) X1 applied to the reference sensors' thermopile signal is used in single-ended mode. The amplifier X2 is in differential mode amplifying the small temperature difference between sample and reference sensor. Shielding, gain settings and status are controlled remotely from the PC via a serial interface.

The reference temperature amplifier feeds the analog PID controller (SIM 960), which compares the voltage with the set-point received from the computer. The proportional gain is set to 1 because of the more advanced preamplifier X1. The integral gain is found to be optimal at 10⁴ s⁻¹ for the used sensors. A bandwidth of 100 kHz is the limiting factor of this temperature control unit. Larger bandwidth of 1 MHz and smaller noise level has the amplifier (SIM 911) for the proportional power compensation circuit. Same amplifiers were used for thermopile voltage and voltage difference pre-amplification.

The PID output voltage is applied via limiters and constant resistors to both heaters. These resistors are used not only for current determination but also for avoiding sensor damage by dangerous voltage spikes. For the same reason the power compensation circuit amplification is switched to maximum only during measurements.

The possibility of remote operation is widely used in the control software for the new device. This control is only used for changing parameters of the devices before and after the measurements. Because of that it does not require an extremely fast communication rate. Much faster rates are needed for the temperature set-point signal and the data acquisition.

Meilhaus DAQ

The fast Meilhaus DAQ board ME 4680is was chosen for generating and receiving signals [73]. The board has input and output rate of $500,000 \text{ s}^{-1}$ (shared between 8 channels), and 16 bit DAC/ADC converter, which make it suitable for the described device.

The output of the board generates the user defined voltage which is employed as the set-point for the PID temperature controller. The ability of generation of an arbitrary ‘set’ of points and direct temperature control gives freedom to the experimentalists in performing non-classical (non-linear) temperature treatments too.

The required voltage data are collected during the experiment by 8 inputs with “Sample&Hold” function. Fast measurements (above $1,000 \text{ K/s}$) require fast data acquisition, slow (below 100 K/s) scans should have reduced acquisition rate, avoiding data overflow.

The program voltage profile feed to the PID controller is recalculated from the chosen temperature profile using a thermopile calibration function, which can be chosen from a list depending on sensor environment [77]. The differential power is recalculated immediately as described above and from that heat capacity is determined, as will be described in the next chapters

Software

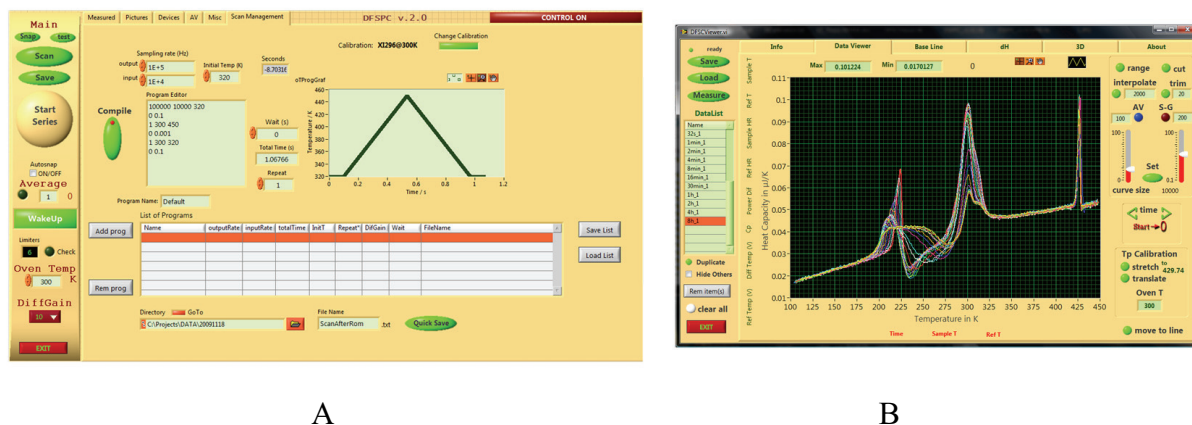


Figure 22. Screen shot from the software for the Fast Scanning Calorimeter. A – Part of the temperature profile programming tab. B - Obtained data after evaluation, including heat capacity determination. See [Appendix A2](#) for more details.

The experiment management software is used for performing one or a series of experiments one by one and saving them, see Figure 22A. Saved data contains all input raw voltage data and some recalculated values: reference and sample temperature, reference and sample heating rate and differential power. For easy evaluation and comparison of curves

collected by the measurement software and for heat capacity calculation separate viewer software was developed, see Figure 22B. The main idea was a separation of evaluation and acquisition software as well as improvement of performance of each part and possibility of additional functionality without memory overload.

The viewer software includes data manipulation like smoothing, interpolation and fitting of signals specific for this device. It was designed to be ready-to-use data evaluation software which produces final results, including specific heat capacity, avoiding the use of additional programs. The experimental results are saved into structured ASCII files which can be imported into any other software. The description of the software in more details can be found in the [Appendix A2](#). Next, some examples are presented to demonstrate the possibilities and limitations of the new device.

3.5. Solidification of metals studied by fast scanning calorimeter

For testing the device, melting and crystallization of small spherical metal particles (μm diameters) were studied. For such first order phase transitions the expected heat capacity and the resulting heat flow curves are known. Even though the particles were small the heat of fusion was large compared to the addenda heat capacity of the sensors. Therefore strong deviations of the programmed temperature profile were detected at low differential gain settings as shown below. Nevertheless, at proper gain settings the instrument is capable to handle such transitions in a very good manner.

In order to observe melting and crystallization the Sn particle was heated from room temperature up to 650 K and cooled back at 500 K/s. The temperature profile and the obtained remaining temperature difference are shown in Figure 23A. Recalculated heat capacity on heating and cooling are represented in Figure 23B and C.

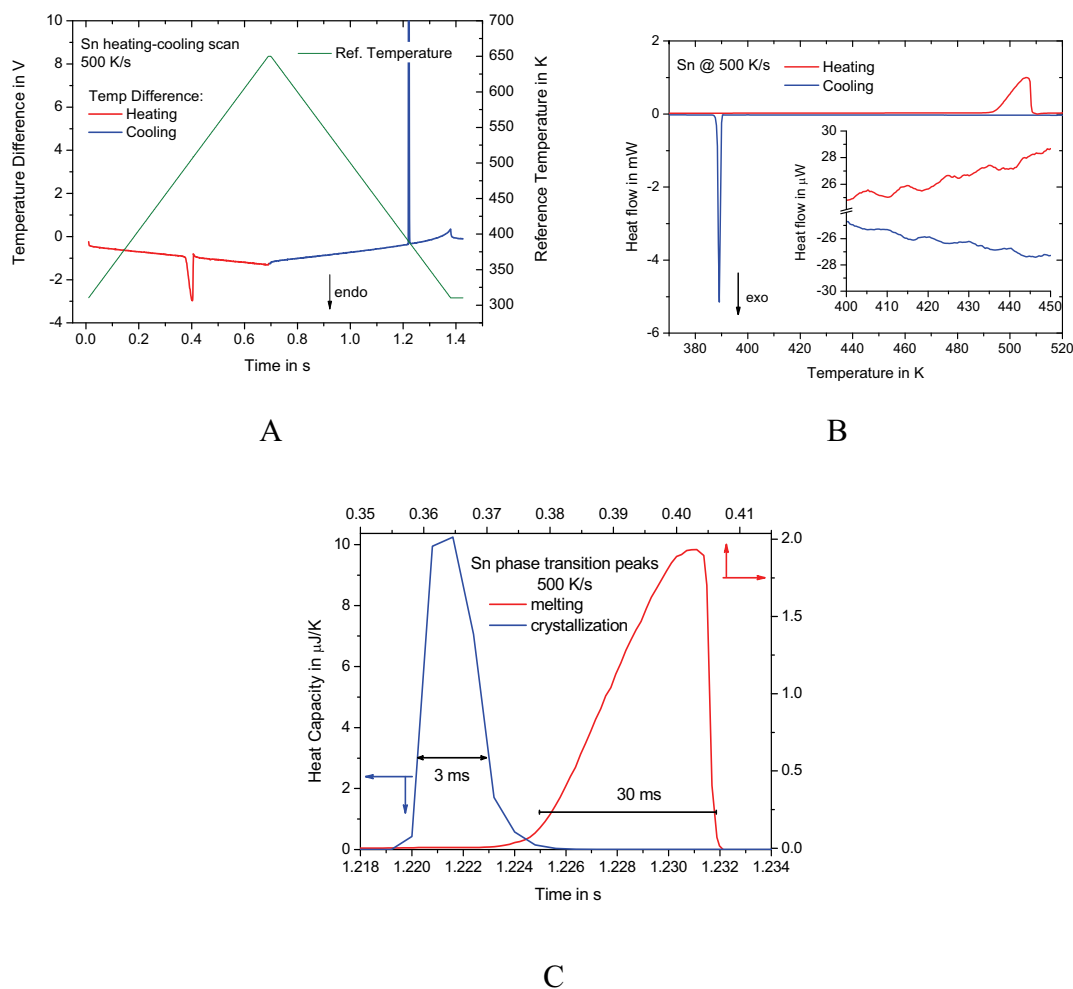


Figure 23. Heating – cooling of a tin sample of 250 ng at 500 K/s. A – Remaining temperature difference and temperature profile, B - recalculated heat capacity. The insert is a zoomed in part of the curves showing noise of about 1 μW peak-to-peak, which corresponds about 1 nJ/K and C - scaled peaks for comparison (be aware of the different scales for heat capacity as well as for time).

On heating the peak shape is determined by the heat transfer from the sensor to the relatively heavy sample. The expected linear leading edge of the peak is seen in Figure 23C. Crystallization on cooling is much faster because of about 100 K supercooling. Therefore heat flow rate during crystallization can be considered as a delta function of about 16 μJ . As shown in Figure 23C the width of the crystallization peak is only 3 ms. The sharp crystallization peak nicely demonstrates the power of the device in handling fast processes also on cooling.

The crystallization peak maximum in Figure 23B equals ca. 5 mW. For a 50 ng polymer sample with a heat capacity of about 50 nJ/K this cooling power for the sample alone allows us for a cooling rate of about 10^5 K/s. Here we show the reaction time of the device for the sensor XI-320. If one wants to study faster reactions one should use sensors with one thermopile and smaller heated area (e.g. XI-292), which is also suited for faster heating/cooling rates.

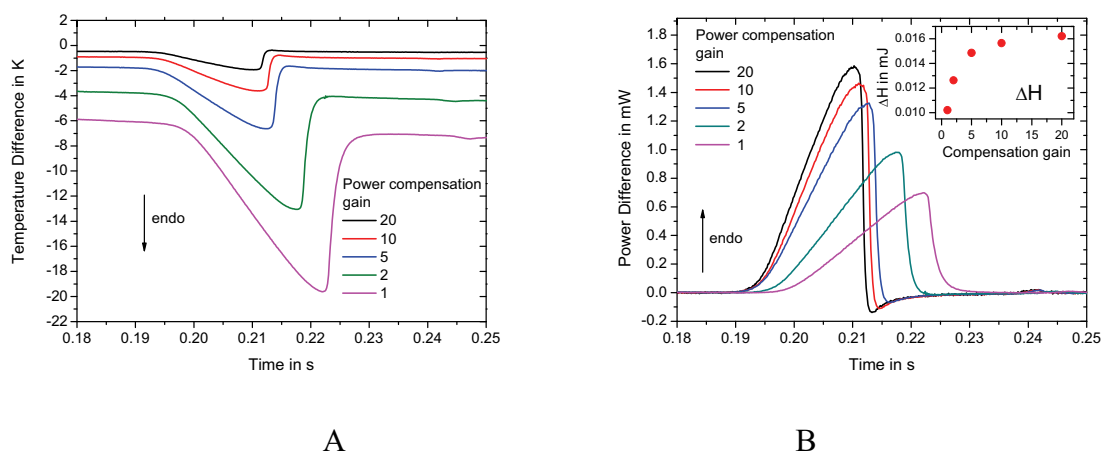


Figure 24 Influence of differential controller gain setting on the resulting curves for a tin sample of about 250 ng at 1,000 K/s heating rate. A - Remaining temperature difference during the melting transition. B - recalculated power difference and heat of fusion (inset), which saturates with higher gain settings indicating that power compensation works properly.

The effect of differential gain (gain of X4 in Figure 20) is shown in Figure 24A for a relatively large tin sample of about 250 ng. For low gain settings the melting peak is much broader than for higher ones. Not enough heat is supplied to the sample sensor, and consequently to the sample, allowing the sample to melt as fast as allowed by the heat transfer (thermal resistivity) between sensor and sample. Only at high gain settings this limit is reached and a limiting shape of the peak is seen. At low gain settings prerequisites for the power determination described above, like equal temperature for reference and sample sensor, are not fulfilled during melting. Therefore the area, see inset, is smaller and reaches the true value only for gain settings above 10. From the particle diameter of ca 20 μm a sample mass of $m_{\text{size}} = 250$ ng was estimated, which yields a heat of fusion of 17 μJ . The measured heat of fusion (Figure 24B) was 16 μJ . This rough estimation (diameter determination as a main source of error) shows that quantitative determination of heat of fusion is possible. This functionality is also realized in the FSC Viewer software (see [Appendix A2](#)).

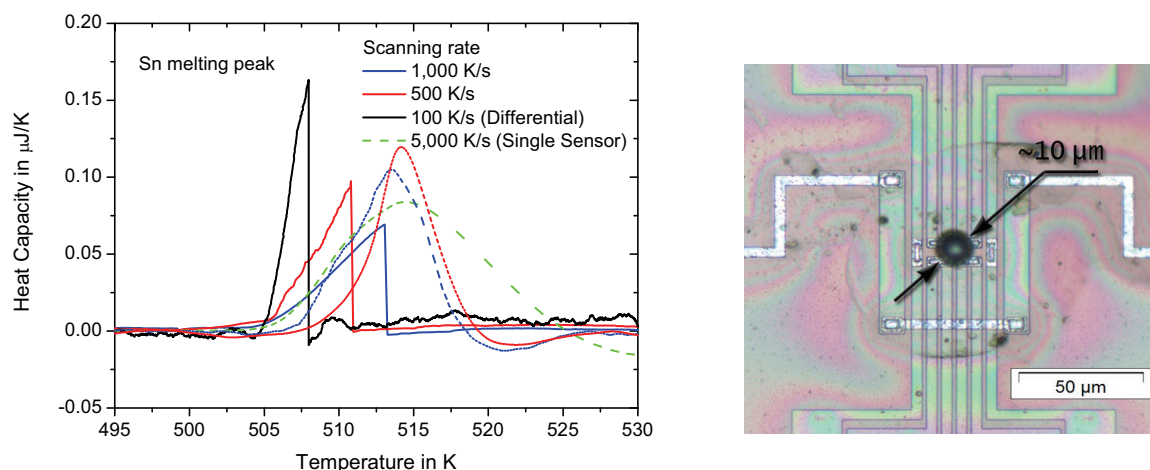


Figure 25. Heating scans of a 24 ng tin sample at different rates on sensor XI-296. Data from the single sensor device (dashed lines) and the differential setup with power compensation (solid lines) are shown for comparison. The same sample on the same sensor was measured in both devices.

Figure 25 shows a comparison of data obtained by the single sensor fast scanning calorimeter without power compensation [5] and the differential fast scanning calorimeter with power compensation. The power compensation yields much sharper peaks, which show the expected shape for a thermal resistivity limited heat flow rate to the melting sample. The estimated enthalpy of fusion from the size (ca. 10 μm) is 2.5 μJ . The measured value was 2.9 μJ which corresponds to an 11 μm particle.

3.6. Temperature calibration

The results of similar melting-crystallization scans for another metal particle (SnAgCu alloy) at different heating-cooling rates are shown in Figure 26A [78]. The melting point shifts with increasing heating rate due to the heat transfer problem (thermal lag). This problem is known from conventional DSC too and is commonly solved in the following way [79]: the peak onset temperatures are plotted as function of heating rate. A linear fit function is used to interpolate or extrapolate, e.g. to negative rates (cooling) as needed. Such a calibration measurement is shown in Figure 26B [80]. For some reasons the data points at low rate deviate from the straight line.

The origin of this effect could be an additional heat transport mechanism which becomes an important only at low rates, e.g. convection. At high rates it is assumed that sample and sensor are cooled only by thermal conduction through the gas [57]. To reduce the

influence of convection one should make the sample as flat as possible, what was not an option for the measurements of spherical particles [78, 81-82]. This undefined additional heat transfer between sample and measuring system, as it is known from two dimensional heat flux DSCs too [83], limits accuracy of the temperature measurement by the thermopile in the membrane significantly.

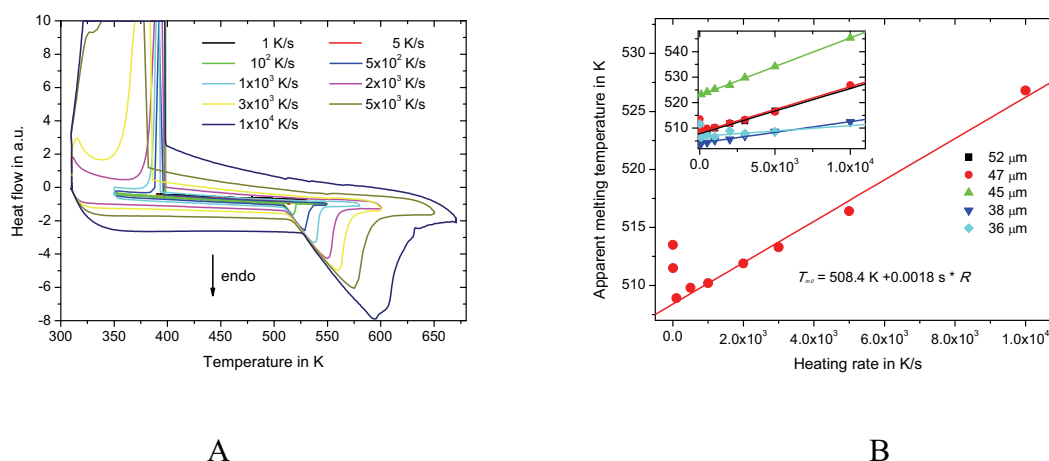


Figure 26. Metal particle melting and crystallization at different rates. A – Measured heat flow. B - Heat transfer correction by melting onset temperature [78].

To study the influence of a polymer sample on the temperature measurement a more complex sample was investigated. A first flat indium particle of ca. 18 ng was placed directly on the membrane and a second one of ca. 6 ng on top of a polymer sample, which covers the first indium particle, see Figure 27. The tiny indium particle on top of the polymer sample was used to study the additional thermal lag due to the polymer sample.

For temperature calibration we follow the procedure for temperature calibration of differential scanning calorimeters (DSC) recommended by GEFTA [79]. Figure 28 shows the peak onset temperatures of the indium melting peaks as function of heating rate. For the first indium particle which is directly placed on the sensor (Figure 27A), the linear behavior is extrapolated to zero heating rate and the obtained value allows one the calibration of temperature in the common way. Accordingly, the intersection at zero heating rate is shifted to the expected value of 429.9 K. The calibration procedure is performed with at least a second standard taking into account temperature dependencies of the calibration factors. All calibrations are performed at the same base temperature to simplify thermopile calibration [77].

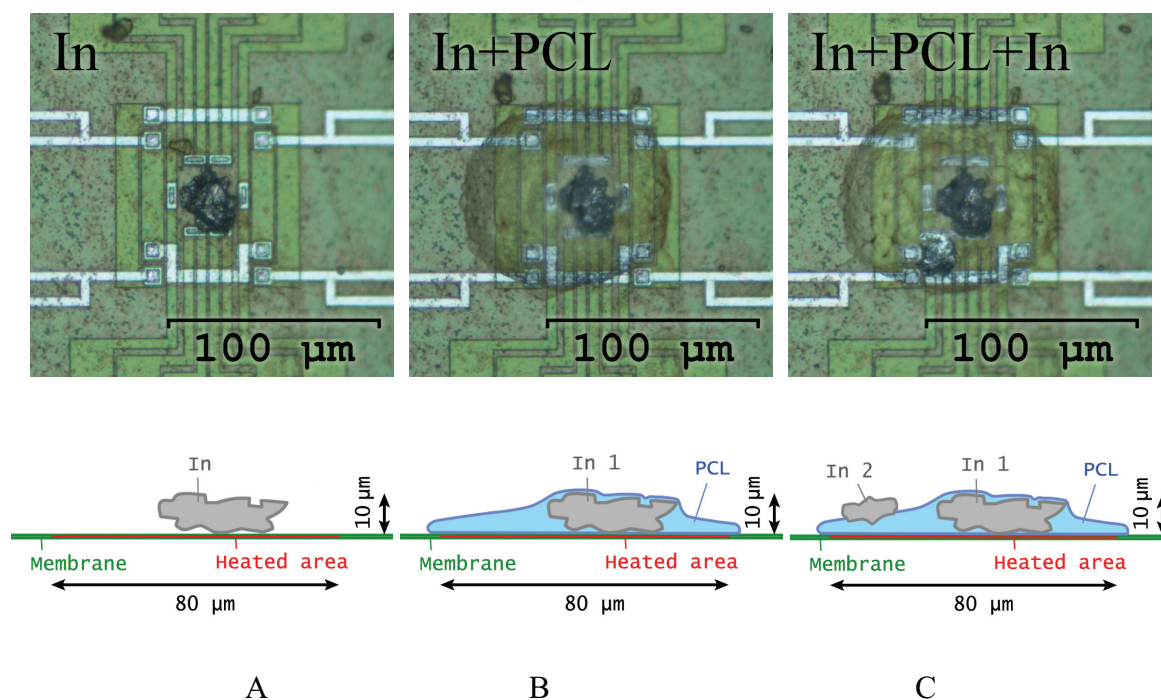


Figure 27. The three samples measured for temperature calibration purposes on a sensor XI 320. A – Indium in the center of the empty sensor. B – The same indium sample covered with poly(ϵ -caprolactone). C – The polymer covered sample from B with another indium particle on top of the polymer 30 μm away from the center.

As seen from Figure 28 the thermal lag for the particle on the membrane is practically zero ($-80 \mu\text{s}$). This unexpected negative slope is caused by the complex coupling between heater and sample and heater and thermopile, which becomes significant at the highest rate only. For the data up to $2 \cdot 10^4 \text{ K/s}$ a horizontal line (pink dashed curve in Figure 28) is obtained. This effect is not further considered here because influences would be discussed below which could cause much bigger uncertainties.

The second curve from bottom shows the peak onset data for the first indium particle covered by a polymer sample (Figure 27B). This time a thermal lag is observed, which may be caused by the addition of a heat capacity of the polymer on top of the In particle. Furthermore, due to capillary forces a polymer layer can form between the indium sample and the sensor surface which increases the thermal resistance compared to the very thin gas layer for the In particle alone. The thermal lag becomes $260 \mu\text{s}$, which is still a very small value yielding a temperature gradient of less than 3 K at 10^4 K/s . For the second indium particle on top of the polymer sample (Figure 27C) thermal lag reaches $800 \mu\text{s}$.

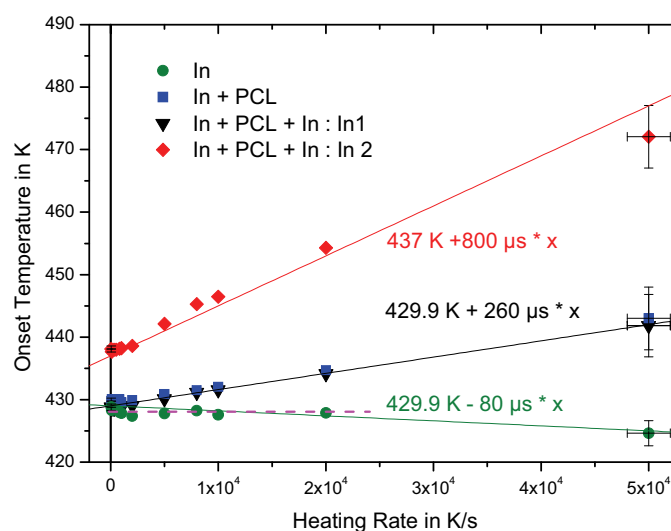


Figure 28. Melting onset versus heating rate of the two indium particles from Figure 27. The lowest curve (green dots) corresponds to the first particle as shown in Figure 27A. The middle line shows the melting onset of the first particle covered by a polymer (PCL) sample (Figure 27 B) (blue squares) and Figure 27 C (black triangles). The upper curve corresponds to the second indium particle on top of the polymer, Figure 27C (red diamonds).

This corresponds to a temperature gradient inside the polymer sample of about 8 K at 10^4 K/s. From this curve a rate dependent calibration can be obtained or the sample thickness can be adapted until an acceptable gradient is obtained. While intersects at zero heating rate for all curves of the first particle are the same, the curve for the small second indium particle intersects at a temperature about 8 K higher. Nevertheless, for both particles the line can be extrapolated to negative rates (cooling) for calibration purposes [83-84], assuming a symmetric operation of the device [78] which is justified because even at controlled cooling the heater provides the heat compensating the heat losses and needed to control temperature.

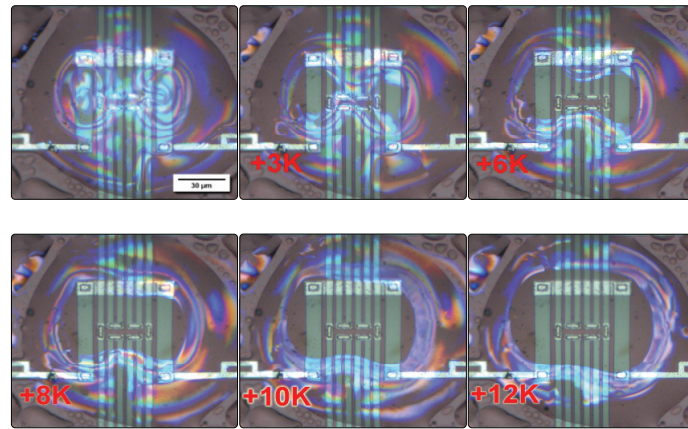
Beside the heat transfer problem (thermal lag) there is an additional problem influencing accuracy of the temperature measurement. Even if the heated area is small it is not homogeneously heated for the large sensors used here because the heater consists out of two resistive heater stripes, see Figure 29. The temperature profile around the heater was investigated by infra-red thermography and analytical modeling of the sensor - gas system [47]. The temperature gradient outside the heater area is very steep and requires a correct placement of the sample in between the two heater stripes. A more detailed analysis of the temperature profile inside the heated area became possible by watching the nematic-isotropic

transition of the liquid crystal 8OCB, which was used for temperature calibration purposes in DSC before [83, 85], by polarized optical microscopy. The contour lines of the phase transition temperature are seen in Figure 29. Temperature differences inside the heated area of several Kelvin as well as some asymmetry of the temperature distribution are detected for the sensor XI-296. These data show again how important a proper placement of the sample is. For precise heat capacity determination the placement of the sample inside the heated area is mandatory. If the sample spreads out of the heated area, e.g. for spin coated or otherwise on the sensor deposited films sample temperature is not well defined, even measurements on such samples are possible.

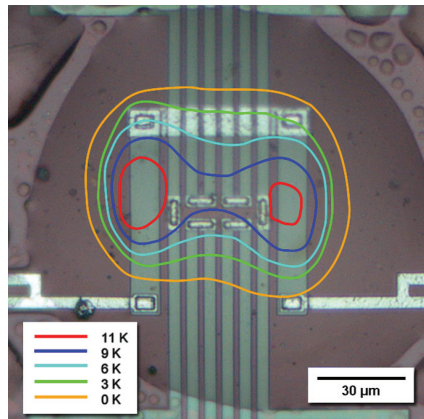
The main issue of metallic particle measurements is the small heat contact area. Especially for spherical particles heat transfer between the sensor and the sample is restricted. One solution to overcome this problem is to place grease in between sample and membrane. Depending on viscosity and surface tension it can accelerate heat transfer significantly. One should take care about the stability of the grease in the temperature range of the experiment and about symmetry of the differential system.

Furthermore the same amount of grease is placed on the reference sensor to minimize the difference in addenda heat capacity. This one can do by placing a small amount of it on the sensor and performing scans at required rates. Usually the amount of grease staying in the heated area is less than 1 ng, which is small in comparison to common sample mass above 10 ng. After several heating-cooling scans nearly the same amount of grease will remain on both sensors. The additional asymmetry in addenda heat capacity may be of the order of 0.1 nJ/K, which can be neglected in most cases. Furthermore, it is possible to perform an ‘empty’ sensor heat capacity measurement, which is then subtracted from the sample scan, in analogy to classical DSC. Nevertheless, the particle feels the temperature of the contact spot with the sensor surface and this temperature may be different from that measured by the thermopile. This also explains the vertical shift of the curves for different particles as shown in the inset of Figure 26B and in Figure 28.

The data presented here indicate that there are other effects than thermal lag influencing temperature measurement by the thermopile of the chip sensor. One effect is the lateral temperature profile in the heater area. For the sample under investigation it limits accuracy of the temperature measurement to about ± 10 K. From the slope of the curve for the indium particle on top of the polymer we see that at 1000 K/s an additional shift of about 1 K and at 10,000 K/s of 8 K has to be taken into account. While the position of the sample cannot be controlled perfectly the thermal lag effect can be corrected.



A



B

Figure 29. A -Temperature profiles of the heated sensor XI 296 probed by the nematic-isotropic transition front of the liquid crystal 8OCB by polarized optical microscopy. B – Temperature contour lines for different heater powers.

The indium particle on top of the sample allows us a temperature calibration taking into account thermal lag and other influences from the sample. Then the accuracy for temperature is ± 4 K and reproducibility ± 1 K. If temperature measurement depends on a previous calibration, uncertainty may reach ± 10 K but reproducibility is still within ± 1 K. Temperature measurement for the chip calorimeter requires improvement and the data shown above point to different possibilities. (i) The lateral temperature profile should be averaged by a good thermal conducting layer, e.g. metal film, covering heater and thermopile. (ii) Sensors with smaller heated area like XI 292 ($10 \cdot 10 \mu\text{m}^2$) minimize lateral temperature distribution. (iii) Sample thickness must be small enough to avoid thermal lag at high rates.

4. Heat capacity determination

4.1. Scheme for differential power determination

The practical realization of the control scheme described above is shown in Figure 30.

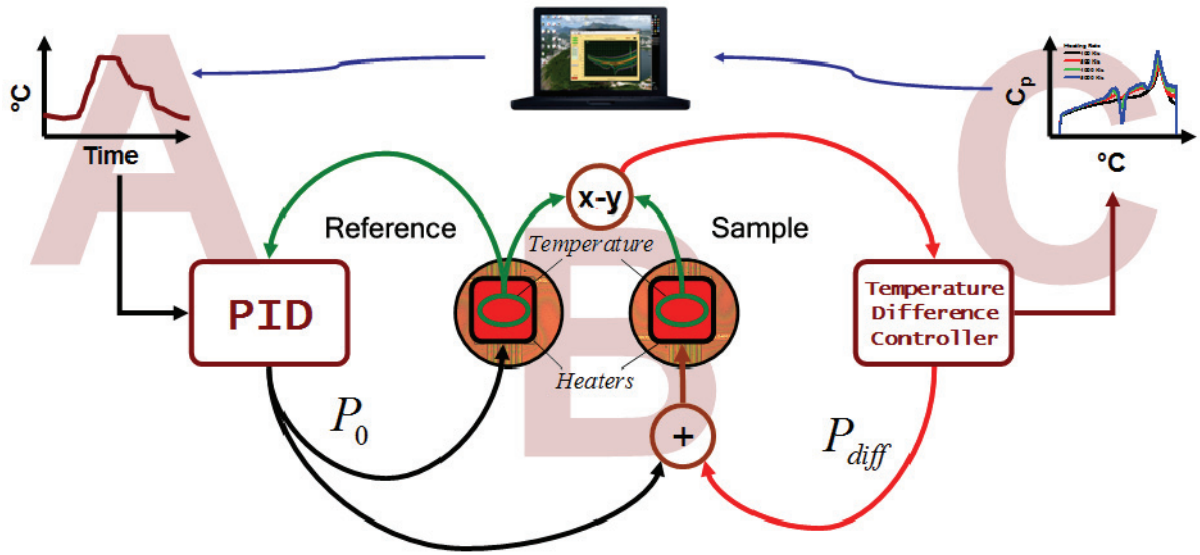


Figure 30. Scheme of the power compensated fast scanning calorimeter. A - The temperature profile is generated by the user and is provided to the PID controller through a DAC board. B - Sample temperature followed the required profile by means of control loop. C - The resulting temperature difference can be recalculated to heat flow rate and sample heat capacity as shown below.

The user defined time-temperature profile is recalculated into a voltage and provided as the set-point for the PID controller. The PID controller makes the temperature of the reference sensor to follow the experimental profile by adjusting power P_0 to its heater. The same power P_0 is applied to sample loaded sensor. The difference between the temperatures of reference and sample side is minimized by the differential controller by adding power P_{diff} to the sample side. The actual realization of this scheme using thin film chip calorimeter sensors is shown in Figure 20.

The main idea of the heat capacity determination was described in previous chapter and equations (3.1) - (3.3). Consequently, the aim was to set up a system with near to perfect power compensation, which allows one the determination of $P_{diff}(T)$ and finally to correct for unavoidable asymmetries between both sides in real measurements at high scanning rates.

4.2. Heat balance

Scanning calorimeters determine the power difference between reference and sample side during controlled temperature treatment [86]. The heat capacity of the sample during the scan can be recalculated from P_{diff} and heating rate using the heat balance equations (3.1) - (3.3), or more precisely:

reference:
$$C_0^{ref} \frac{dT^{ref}}{dt} = P_0^{ref} - P_{loss}^{ref}(T) \quad (4.1)$$

sample:
$$(C_0^{sample} + C_{sample}) \frac{dT^{sample}}{dt} = P_0^{sample} + P_{diff} - P_{loss}^{sample}(T) \quad (4.2)$$

where P_0 and P_{diff} are average and differential power generated by the heaters, C_0 and C_{sample} are heat capacity of empty sensor (addenda) and sample, respectively. dT/dt is temperature scanning rate and $P_{loss}(T)$ is heat loss to the surrounding. Superscripts *sample* and *ref* denotes sample and reference sensors, respectively.

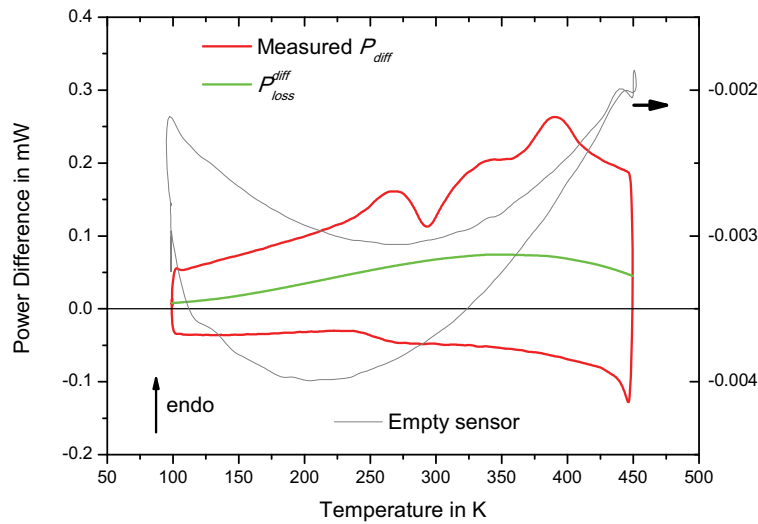


Figure 31. Power difference (red curve) on heating and cooling used for determination of heat loss difference (green center curve). iPP sample of ca. 56 ng at 1000 K/s scanning rate. The light gray curve shows the power difference from an empty sensor at a 100-fold enlarged scale (right axis).

The addenda heat capacity of the heated part of the membrane is ca. 30 nJ/K at room temperature. Using sensors from the same wafer the difference in addenda heat capacity is of the order of 0.6 nJ/K (see inset in Figure 32B). Therefore we can neglect the difference between reference and sample side addenda heat capacities compared to sample heat capacity of commonly more than 10 nJ/K and express sample heat capacity as:

$$C_{sample} \frac{dT}{dt} = P_{diff} - P_{loss}^{diff}(T), \quad (4.3)$$

Determination of P_{diff} for a fast scanning calorimeter was described in previous chapters. The differential loss function $P_{loss}^{diff}(T)$ is a smooth function of temperature containing asymmetries of the system including the difference in heat losses and P_{asym} , containing all other differences between the two sensors. The latter can be modified by hardware adjustments to minimize $P_{loss}^{diff}(T)$ and therefore the difference between P_{diff} and $C_{sample}(dT/dt)$. The influence of the heat loss difference on heat capacity determination and its correction is described next.

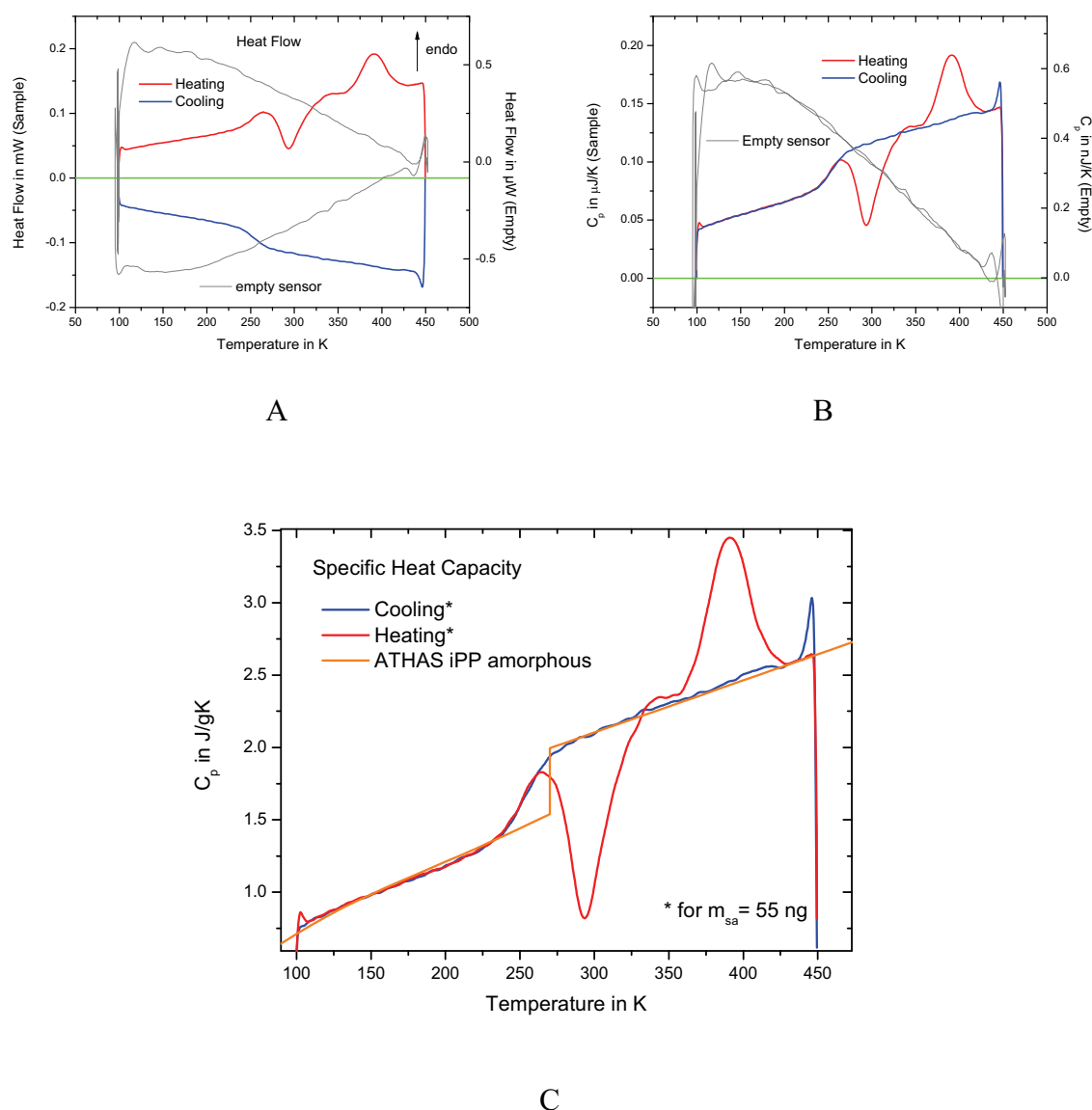


Figure 32. iPP sample of ca. 56 ng at 1000 K/s scanning rate. (A) Heat flow rate to the sample (red and blue curves, left axis) and from the empty sensor (light gray curve, right axis 100-fold magnified) recalculated by subtracting the power difference shown in Figure 31 from the measured data. (B) Sample heat capacity (red and blue curves, left axis) and addenda heat capacity difference from the empty sensors (light gray curve, right axis 100-fold magnified). (C) Specific heat capacity curve determined using liquid specific heat capacity above melting at 430 K from ATHAS databank [87].

4.3. Determination of differential loss function

The measured quantity by differential scanning calorimeters is the power difference between sample and reference sensors. To better understand interpretation of the obtained data we consider once again the different causes of the obtained signals (Figure 33). As an example a polymer sample was chosen because of its good adhesion properties and well-defined thermal contact properties. The sample heat capacity shows solid and liquid heat capacity below and above the glass transition (Figure 33A). When the sample is heated it requires a heat flow into it and the same heat flow out of it on cooling at the same rate (Figure 33B). Nevertheless, the measured power difference is the heat flow to the sample plus the smooth temperature dependent curve representing all asymmetries of the differential system (Figure 33C). This is a schematic representation of $P_{loss}^{diff}(T)$ from equation (1.6). As shown by Minakov and Schick [5] the chip sensors utilized for fast scanning calorimetry behave quasi-static up to rates of 10^5 K/s. Only at higher rates time dependence of addenda heat capacity (heated area of the membrane) and heat losses have to be considered. The same can be considered for common DSC's. Therefore the same differential loss curve is added to the heat flow signal originating from the heat capacity (Figure 33B), independent on heating rate or thermal history of the sample. Then the differential loss curve can be determined under optimal experimental conditions, e.g. if only a glass transition and no crystallization and melting occurs. This differential loss curve is then applicable for the correction of all other measurements for this particular sample as shown below.

If we are interested in sample heat capacity it requires correction of the measured data in the reverse order. The first step, determination of the heat loss difference line in the whole temperature range of interest is the main task for determining sample heat capacity. In contrast to power compensated DSC it is not possible to determine this line experimentally from an empty measurement [53, 86]. Similar to heat flux DSCs the loss function of the chip-based sensors depends on the sample under investigation. If, for example, a 50 μm diameter spherical metal sample is measured the heat exchanging surface is nearly doubled compared to the flat reference sensor [78]. Under such conditions the assumption of symmetry between both sensors is seriously violated and yields strong curvature and slope of the $P_{loss}^{diff}(T)$ symmetry line between heating and cooling as shown in Figure 31Figure 33. Furthermore, transitions on heating and cooling may occur at different temperatures and have different width. Then the symmetry line does not equal the average between both curves in the whole

temperature range but only outside the transitions. In Figure 31 and Figure 32 these transitions are glass transition, cold crystallization, and melting of isotactic polypropylene (iPP) on heating and only glass transition on cooling.

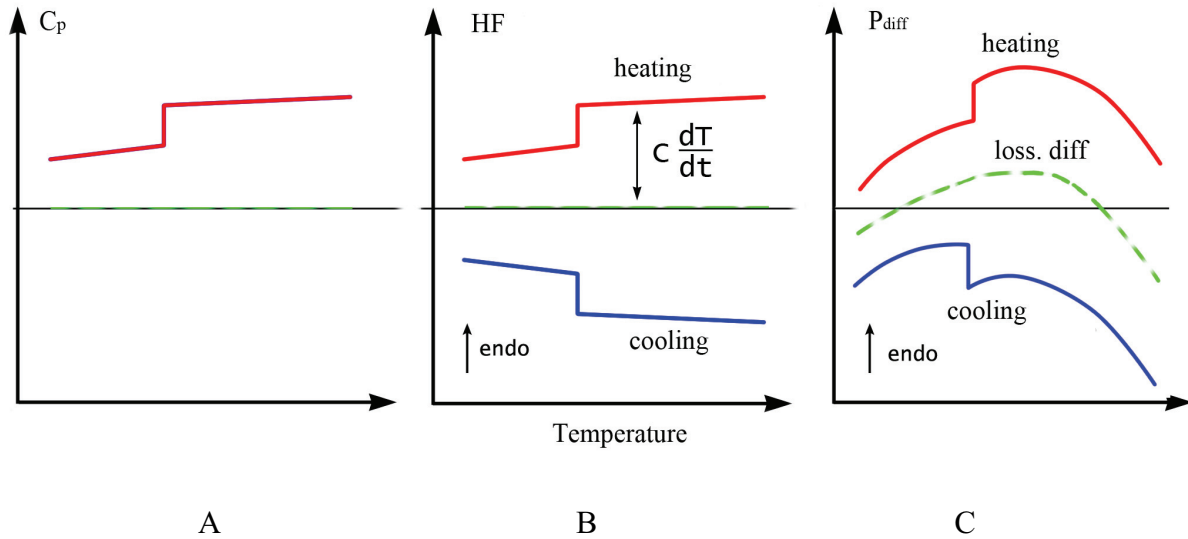


Figure 33. Origins of the measured signal. (A) Temperature dependent heat capacity including a step at T_g . (B) On heating or cooling at the same rate a positive or negative heat flow into or out of the sample is required. (C) The heat loss difference (dashed green line) is added to the heat flows from B. This sum is the finally measured power difference.

The construction of the loss curve $P_{loss}^{diff}(T)$ therefore requires inter- or extrapolation into the transition region from outside the transitions as shown in Figure 31. Because it is not a simple task to find an analytical expression for $P_{loss}^{diff}(T)$ for each sample under investigation it is recommended to search for a as smooth as possible curve describing $P_{loss}^{diff}(T)$ and yielding equal heat capacity outside the transition regions, where heat capacity is sample treatment and time independent. For polymers these regions are commonly located below glass transition and above melting temperature, as shown below.

In the differential fast scanning calorimeter measurements $P_{loss}^{diff}(T)$ can be approximated with a smooth 2nd or 3rd order polynomial. This fact and the significant reduction of $P_{loss}^{diff}(T)$ to a value comparable to the heat capacity contribution to the heat flow are the main advantages of the new device in comparison to the single sensor technique where

a 3rd to 5th order polynomial is used to describe the steeply increasing loss curve (see Figure 17). The final calculation of heat flow difference to sample heat capacity is shown in Figure 32A. First, the $P_{loss}^{diff}(T)$ curve (green center curve in Figure 31) is subtracted from the measured data. The result is shown in Figure 32A. Dividing curves for heating and cooling by the respective scanning rates yields heat capacity as function of temperature as given in Figure 32B.

The direct mass determination of the micron-sized samples is a complex task, which is better to avoid. To calculate specific heat capacity out of the data in Figure 32B one has to estimate sample mass indirectly. One possibility is to use reference specific heat capacity data for the particular material from literature or independent measurements. For most polymers specific heat capacity data can be found in ATHAS databank [88]. Knowing specific heat capacity at a temperature T^* away from phase transitions, e.g. in the melt, one can estimate sample mass by comparing measured heat capacity with the known specific heat capacity ($m_{sample} = C_{sample}(T^*) / c_{ATHAS}(T^*)$) [89]. The resulting specific heat capacity for heating and cooling of iPP by comparing with ATHAS data for liquid heat capacity at 430 K is shown in Figure 32C. For sample mass (56 ± 5) ng good agreement between measured heat capacity and expected specific heat capacity in the whole temperature range of the measurement is achieved.

To demonstrate that $P_{loss}^{diff}(T)$ depends only on temperature and not on scanning rate (time) a PCL sample was scanned at different rates from 100 to 10,000 K/s. The resulting differential power curves are shown in Figure 34. Each curve corresponds to heating and cooling at the same rate.

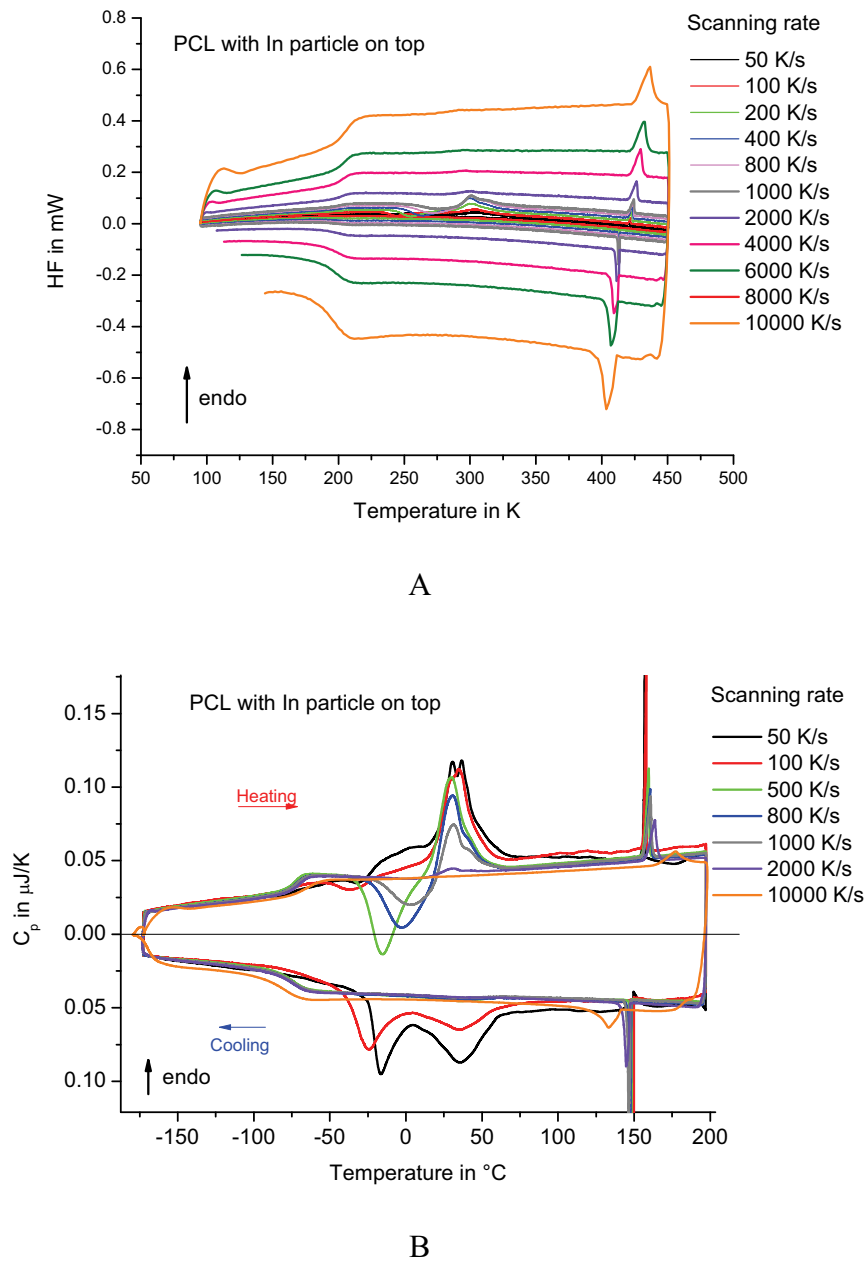


Figure 34. Cooling-heating-cooling scans of a PCL sample at different rates. (A) Power difference measured and (B) heat capacity recalculated using one common curve for heat loss correction (see chapters 4.4 for details on PCL experiments). $P_{loss}^{diff}(T)$ was determined from the measurement at 1000 K/s.

As seen from Figure 34A all curves are symmetric around one line, which corresponds to $P_{loss}^{diff}(T)$. For measurements in a wide range of scanning rates or other thermal histories it is therefore preferable to determine $P_{loss}^{diff}(T)$ under optimal conditions, e.g. at a rate where only the glass transition is seen and not crystallization and melting. Then the $P_{loss}^{diff}(T)$ curve can be determined with high confidence and applied for all other curves as long as the sample does

not change position or color (changing losses). From equation (4.3) it follows that at zero or close to zero heating rate the left side of the equation becomes zero and $P_{loss}^{diff}(T)$ equals $P_{diff}(T)$, allowing one a simple determination of $P_{loss}^{diff}(T)$. Unfortunately, this procedure does not work because at very low rates the sample commonly starts to flow and the chip may be heated as a whole, including the cold junction of the thermopile. As soon as the $P_{loss}^{diff}(T)$ curve is determined, the differential power can be recalculated into heat capacity according to (4.3). For selected rates heat capacity is shown Figure 34B. The scatter of the data at 450 K is about ± 5 nJ/K. This corresponds to a scatter of ± 8 % for scanning rates between 50 and 10^4 K/s, with the largest uncertainties for the slowest rates. Uncertainty for specific heat capacity is mainly determined by the uncertainty of the sample mass determination. It is of the order of ± 10 %, which is not perfect but sufficient for a comparison between different samples. Reproducibility of the obtained data for one sample measured under the same conditions and at the same rate is about ± 2 %. The good reproducibility of the heat capacity data allows one an accurate comparison of curves obtained after different thermal treatments. Next, an example of measurements on a polymer sample is presented.

4.4. Crystallization of polyethylene (PE)

The influence of cooling rate on the crystallization temperature of PE was studied in a wide range of scanning rates. The polymer sample commonly creates a good thermal contact with the membrane surface. But in order to improve the temperature distribution and to allow an easy replacement of the sample a gold foil (gold leave ca. 100 nm thick) was placed under the sample. In some cases the foil also helps to avoid spreading of the sample into the cold region of the membrane. In this particular case it was used to create similar experimental conditions in three different calorimeters. In case the sample-substrate interface acts as a nucleation site it should not be too different.

In DSC experiments, thought to extend cooling rate range to lower rates, we use aluminum pans as sample container. To make the substrate for the fast scanning experiments also metallic the 100 nm thick gold foil was used (Figure 35A)

Ultra high molecular weight polyethylene (UHMWPE) was chosen as a model system because of its stability, very high crystallization rate and a large number of existing studies, e.g. [90]. The resulting heat capacity on heating and cooling at different rates is shown in Figure 35B. The sample mass was ca. 5 ng which is not big enough to give a good signal at

low scanning rates. 500 K/s is the slowest rate with a reliable signal. But the low mass sample increases the highest possible rate. Crystallization and melting were observed in the scanning rate range of 100–10,000 K/s. Except for the curves at 100 K/s heat capacity is reproducible within $\pm 2\%$. As shown on Figure 35B with increasing cooling rate the crystallization peak shifts to lower temperatures. Covering such wide range in cooling rates makes peak position meaningless because even a thermal lag of 1 ms creates a serious shift for a peak with a magnitude of about 5 times that of the baseline heat capacity. The shift for the peak may be about 50 K at 10,000 K/s compared to 5 K for the onset according the data shown in [67]. Therefore the rate dependence of crystallization peak onset temperature is shown on Figure 35C.

Because non-isothermal crystallization kinetics in a wider range of scanning rates was of interest two other calorimeters were used too. A Mettler Toledo DSC 822 was measuring an 11 mg sample at slow rates down to 1 mK/s and a Perkin Elmer Pyris 1 DSC was measuring a ca. 1 mg sample from 0.05 K/s to 2 K/s. There is still a gap of two orders of magnitude in scanning rate between the Perkin Elmer DSC and the Fast Scanning setup. But the general tendency of the peak onset reveals a relatively smooth line covering 7 orders of magnitude in scanning rate. Even the fastest rates of 1 MK/s [5] can not be realized with the device and the sensor used, the benefits of the new power compensation differential scanning nano-calorimeter are feasible. The ability to perform fast controlled temperature treatments at the same sample and the advanced heat capacity determination makes it a versatile device for routine investigations of polymers [91-93] and metals [67, 78, 81-82].

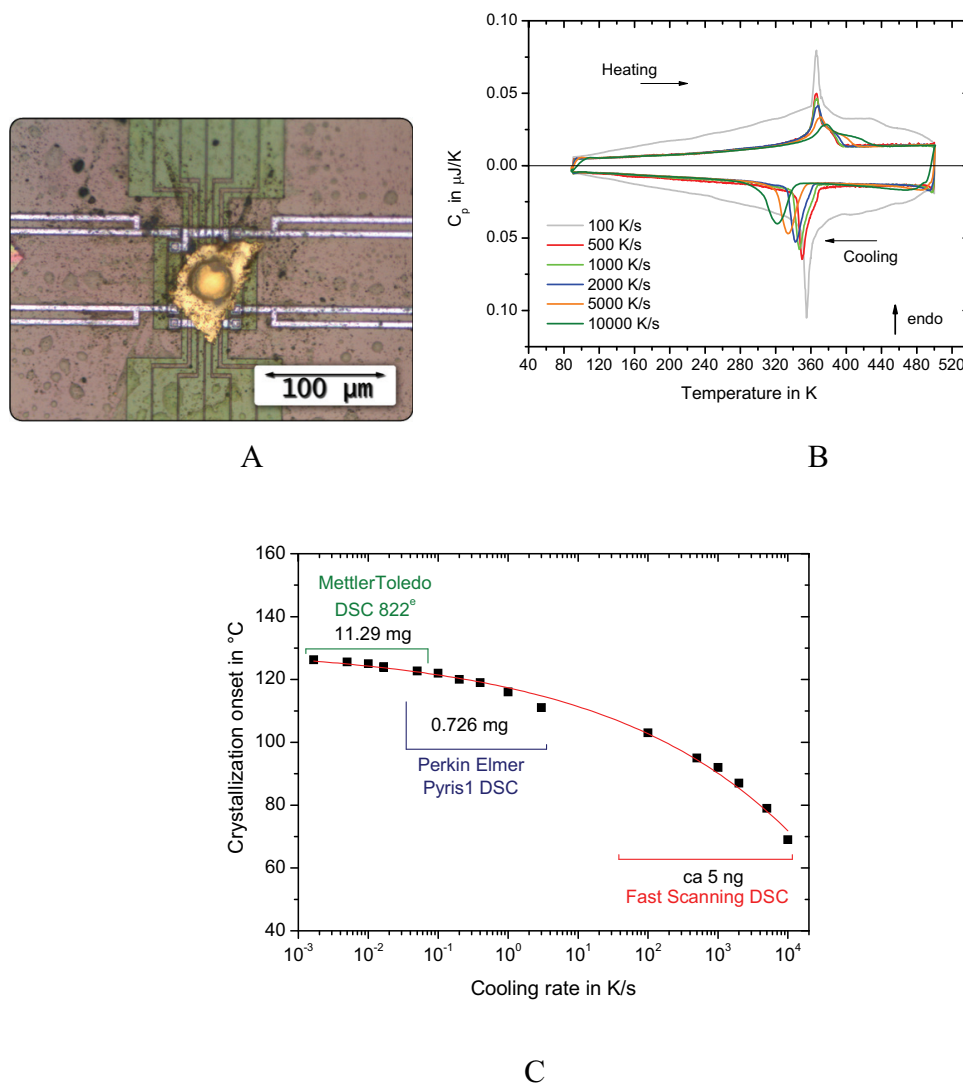


Figure 35. (A) Sample preparation on sensor XI-320 with a gold foil under the UHMWPE sample. (B) Melting and crystallization of UHMWPE at different heating and cooling rates. (C) Peak onset temperature for non-isothermal crystallization in a wide range of cooling rates achieved by combining three calorimeters. The line is a guide for the eyes.

4.5. Solidification of pure and nucleated poly(ϵ -caprolactone) (PCL)

Another industrially important polymer, poly(ϵ -caprolactone) (PCL) was investigated using the new device. Poly(ϵ -caprolactone) has much slower crystallization rate, in

comparison to polyethylene, which can be enhanced using nucleating agents. The influence of nucleating impurities on non-isothermal crystallization can be observed on cooling-heating scans at different rates.

The sample was prepared in a similar way as polyethylene, as seen in Figure 36.

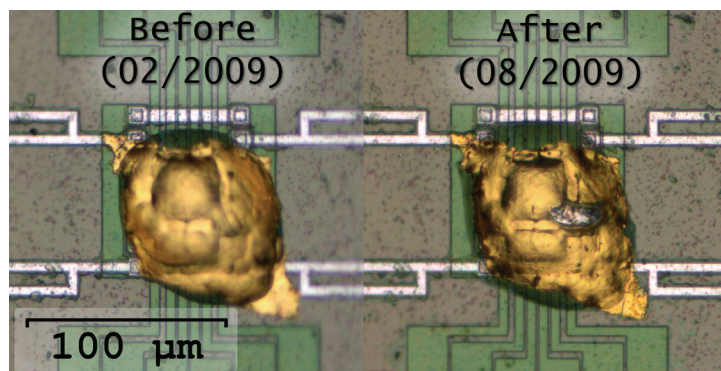


Figure 36. Sample before measurements and after all the annealing experiments described below. Indium particle was added during experiments to measure temperature of the sample at the outer surface.

The same sample was used for all subsequently described experiments. The sample stability was proved by a reference test scan at 1000 K/s after each series of measurements. In addition the small indium particle (ca. $3.5 \times 3 \mu\text{m}^3$) was placed on top of the sample to identify changes of temperature distribution in the sample. The gold foil in between the sample and the sensor was intended to restrict the flow of molten polymer out of the measuring area. In spite of the long annealing and the large number of measurements the reference scans showed no significant changes. Therefore the assumption was made that the main mass of the sample remains within measuring area. This was proved by images of the sample before and after treatments (Figure 36). In addition to that, the same material was measured on different sensor of different type and shows the same kinetics of crystallization at several temperatures. This result proves reproducibility of the experiments on different sensor types.

The results of heating-cooling experiments for pure and nucleated PCL are shown in Figure 37.

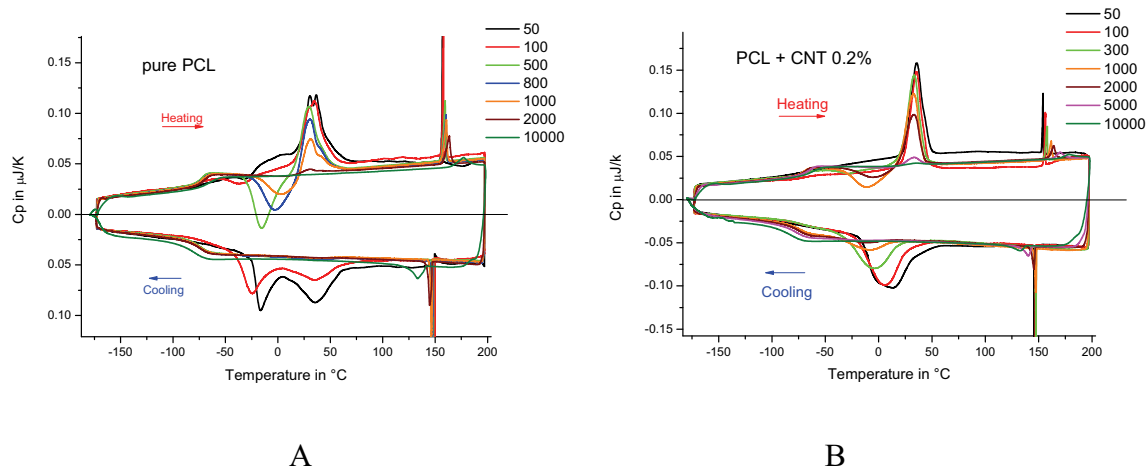


Figure 37. Symmetric heating-cooling scans at different rates of pure PCL (A) and PCL with 0.2% MW CNT (B)

Both pure and nucleated samples give a complex melting and crystallization behavior. PCL crystallization was suppressed on cooling faster than 500 K/s and on heating faster than 10,000 K/s. The nucleated PCL crystallizes much faster – up to 2000 K/s cooling and more than 20,000 K/s on heating.

Although the heating and cooling of samples of this size is possible from 1 to 50,000 K/s, a reliable data acquisition is possible only from 50 K/s. The problem of signal to noise ratio was discussed in previous chapters. Comparison of obtained results even from 50 to 10,000 K/s is complicated due to different error of heat capacity determination at different scanning rates. As seen from Figure 37, the 50 K/s and even 100 K/s has significant error in comparison to the other scans. The range of cooling rates 100 – 1000 K/s is of interest for investigation of crystallization process in pure PCL.

The stability of PCL and moderate crystallization rates makes it nice model material, but for investigation of its crystallization, the new experimental scheme is required. This new method was developed and applied for investigation of non-isothermal crystallization and thereafter isothermal crystal nucleation and growth kinetics will be described in the next chapter.

5. Crystal nucleation and overall crystallization kinetics in PCL

5.1. Influence of existing nuclei and crystals on subsequent heating

Poly(ϵ -caprolactone) was used as a model system to study the kinetics of crystal nucleation and growth processes in the full range of temperatures where they occur. The Fast Scanning Calorimeter was used to perform heat flow measurements during fast temperature treatment and the new software was employed for quantitative analysis of the measured data.

The comparison of directly measured and recalculated excess heat capacity data during crystallization has disadvantages due to increasingly high error at low cooling rates. Therefore an indirect method for quantitative characterization of the crystallization process was used. Figure 38 shows the influence of degree of crystallinity developed on cooling on the heating scan on the example of PCL. If the sample is fully crystallized on cooling the heat capacity on heating shows a reduced step at glass transition and melting, Figure 38A. In case of a fully amorphous state after cooling (Figure 38C) and moderate heating rates (Figure 37A) the pronounced step in heat capacity at T_g , cold crystallization and melting of cold crystallized phase is observed. Intermediate state of material reveals less expressed cold crystallization and melting of previously present crystals and crystals formed on cold crystallization on heating (Figure 38B).

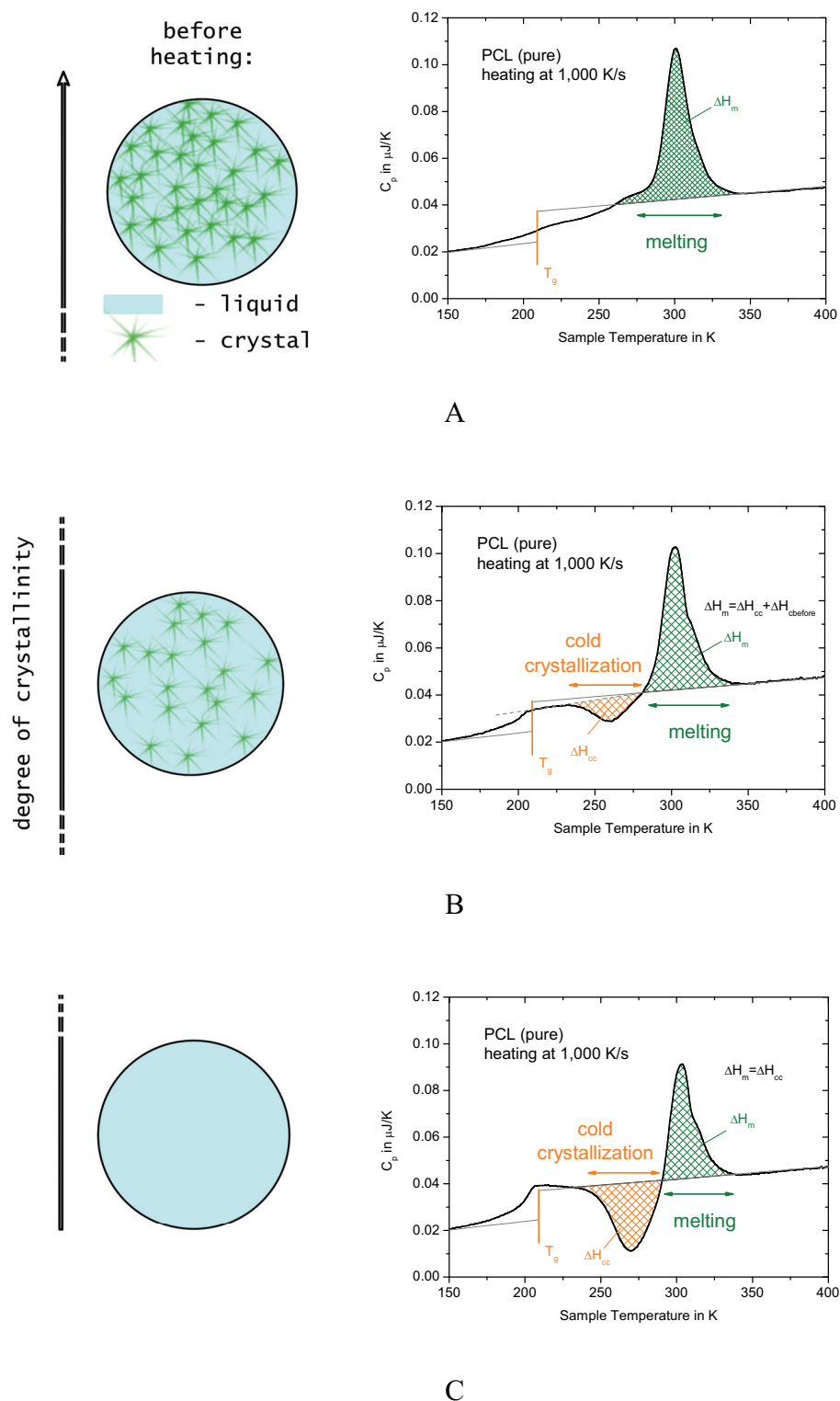


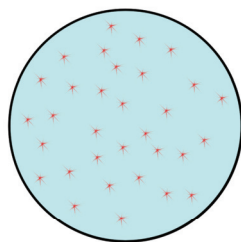
Figure 38. Heating of the sample with different degree of crystallinity (A – fully crystallized, B – partly crystallized, C – amorphous). Quantitative evaluation of corresponding melting and crystallization on heating – see text for details.

Therefore total excess enthalpy change on heating ($\Delta H_{total} = \Delta H_m + \Delta H_{cc}$ in Figure 38) could be used as a measure of overall crystallization during temperature treatment preceding the heating scan. The base line for peak integration is selected as described below, basically following Mathot's approach [94] (Figure 38). The melting peak is always integrated versus liquid heat capacity of the sample (grey line in Figure 38). The cold crystallization peak area is integrated against liquid heat capacity in case of fully amorphous sample (Figure 38C) and against some intermediate between liquid and crystalline heat capacity line for semi-crystalline sample (Figure 38B).

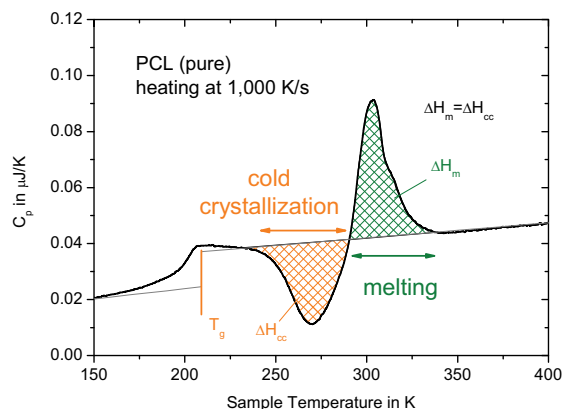
Furthermore, Oguni [2] and Mathot [1] in similar calorimetric experiments have shown that the cold crystallization peak size is also dependent on the amount of nuclei in the amorphous sample before heating. Oguni et al. demonstrated that the cold crystallization was vanished fully, in Mathot's results the reduction of cold crystallization was observed with reduction of the amount of nuclei. Schematically, using PCL data, this can be shown as in Figure 39.

Therefore the heating of the sample after temperature treatment can be used for detection of two processes which take place before heating: nucleation and overall crystallization. As long as the sample is heated always at same rate, the influence of 'addenda' nucleation on heating can be predicted and taken into account for study of the processes which takes place during preceding heat treatments only. The fixed heating rate allows one application of same data evaluation procedure for all data, therefore minimizing errors which can arise during evaluation of scans at different rates (Figure 37). In addition to that, there is no more need to evaluate tiny noisy signals during isothermal experiment (especially at long crystallization times, like in [63]). All temperature treatments which do not destroy the sample, can be performed and then investigated on successive heating scans at the same device under the same conditions.

amorphous sample
before heating

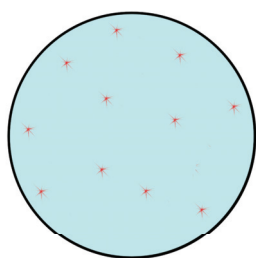


more nuclei

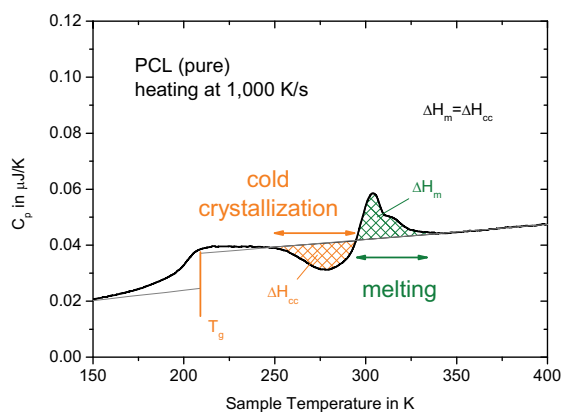


A

amorphous sample
before heating



less nuclei



B

Figure 39. Reduction of cold crystallization and corresponding melting in dependence on the amount of nuclei in the amorphous sample before heating (be aware of the different peak sizes).

For investigation of PCL crystal nucleation and overall crystallization a heating rate of 1000 K/s was chosen. First, this is the optimal scanning rate for data evaluation regarding signal to noise ratio. Second, it has pronounced cold crystallization in case of amorphous samples (Figure 37). A slower heating is less preferable as far as the nuclei created on heating superimpose nucleation that happens before heating.

To study nucleation as well as crystallization in PCL the ability to avoid crystal nucleation and growth on cooling is required as shown in the introduction. The elimination of crystallization on cooling was already shown in experiments before (Figure 37). Next the possibility to avoid homogeneous nucleation on cooling will be demonstrated. A new method of analysis of crystal nucleation and overall crystallization during heat treatments by successive heating scans at fixed rate will be described.

5.2. Elimination of homogeneous crystal nuclei formation in PCL on cooling

The temperature control system of the new device was capable to perform temperature scans of samples with a mass in the order of 10 ng from 1 K/s up to 50,000 K/s (without significant temperature lag). First, the influence of cooling rate on structure formation was studied at successive heating scans at a constant rate of 1,000 K/s. The scheme of the experiment is shown in Figure 40.

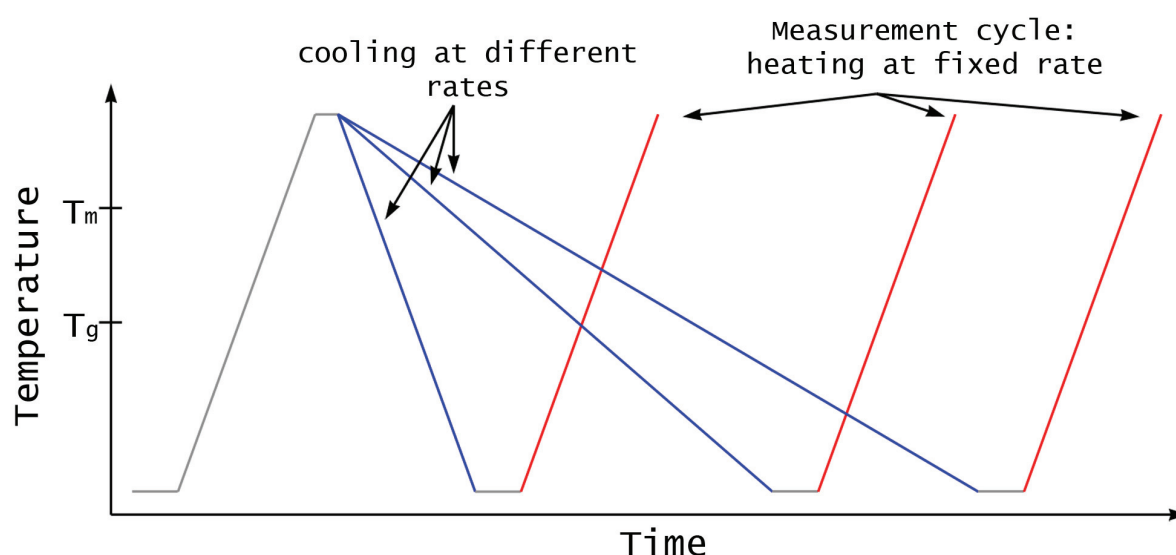


Figure 40. Time-temperature profile of the experiment for investigation of non-isothermal nucleation and overall crystallization in PCL.

The sample was molten at 470 K, ca. 130 K above the equilibrium melting temperature to erase the thermal history, and then cooled at different rates 50...50,000 K/s down to 100 K. The glass transition of PCL is about 200 K. This means that at 100 K any changes with the sample are unlikely. The heating scan at 1,000 K/s was performed after a fixed waiting time of 0.1s after each cooling. The 50 K/s cooling was slow enough to crystallize the sample on cooling and therefore slower cooling was not performed avoiding the problem of spreading of the sample from the heated area. Due to fixed conditions of the measuring cycle (heating at 1000 K/s) the observed changes were connected only with the previous cooling.

The resulting heating scans after cooling at different rates are shown in Figure 41. The observed heat capacity vs. temperature curves are similar to what was measured before at different scanning rates (Figure 37). They are all measured at the same rate and recalculated using the same procedure, which is described in [chapter 4](#). Therefore the obtained data can be better compared, not only qualitatively but also quantitatively.

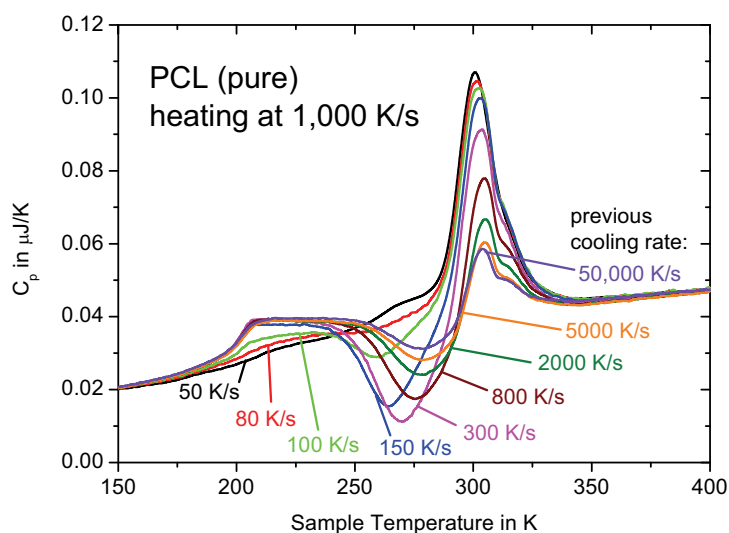


Figure 41. Heating of ca. 20 ng PCL sample at 1000 K/s after cooling at rates from 50 to 50,000 K/s.

After slow cooling the sample was fully crystallized and on heating shows relatively small glass transition step, no cold crystallization and large melting peak. With increasing cooling rate the glass transition step becomes more pronounced due to less crystallized material on cooling. At the same time a cold crystallization peak appears and grows with increasing cooling rate. The melting peak decreases resulting from less crystallinity developed during cooling. At further increasing cooling rate cold crystallization reaches a maximum at about 300 K/s and decreases at higher cooling rates. This finding is in qualitative agreement with Mathot's [1] observations which indicate an influence of cooling on nucleation.

For a quantitative discussion of the data the area of cold crystallization and melting peaks were calculated as it was discussed in previous chapter and shown in Figure 42. To probe overall crystallization on previously made cooling and, if possible, to observe influence of nucleation, the cold crystallization enthalpy and the overall excess enthalpy change on heating were needed. Corresponding values were calculated from peaks in heat capacity curves which would correspond to melting and cold crystallization. The construction of baseline for integration is shown on Figure 42A-B for different cases. All melting peaks were integrated against liquid heat capacity line (straight black line in the figures). The estimation of cold crystallization enthalpy is complicated due to superposition with melting at the end of cold crystallization. Points '1' and '2' in Figure 42B and C are designating the end of glass transition and the beginning of the melting correspondingly. The straight line inbetween these points was taken as a baseline for approximation of cold crystallization enthalpy. For an amorphous sample heat capacity above glass transition equals liquid heat capacity and this line will coincide with the extrapolated line from the melt (Figure 42 B). The overall excess enthalpy change on heating was taken as a sum of these two terms (positive melting enthalpy and negative cold crystallization). Compared to Mathot's approach [94], this yields an additional error, but does not change the overall picture. Dependency of overall excess enthalpy change (blue line) as well as cold crystallization (orange) and melting (olive) enthalpies versus previous cooling rate are shown in Figure 42 D. The error bars includes influence of variation of baseline construction on the result of integration.

Overall enthalpy on heating becomes zero within error of the measurement at previous cooling rates higher than 500 K/s. This means that no crystallization occurs on cooling under this condition. This also coincides with results of previously performed non-isothermal experiments (Figure 37).

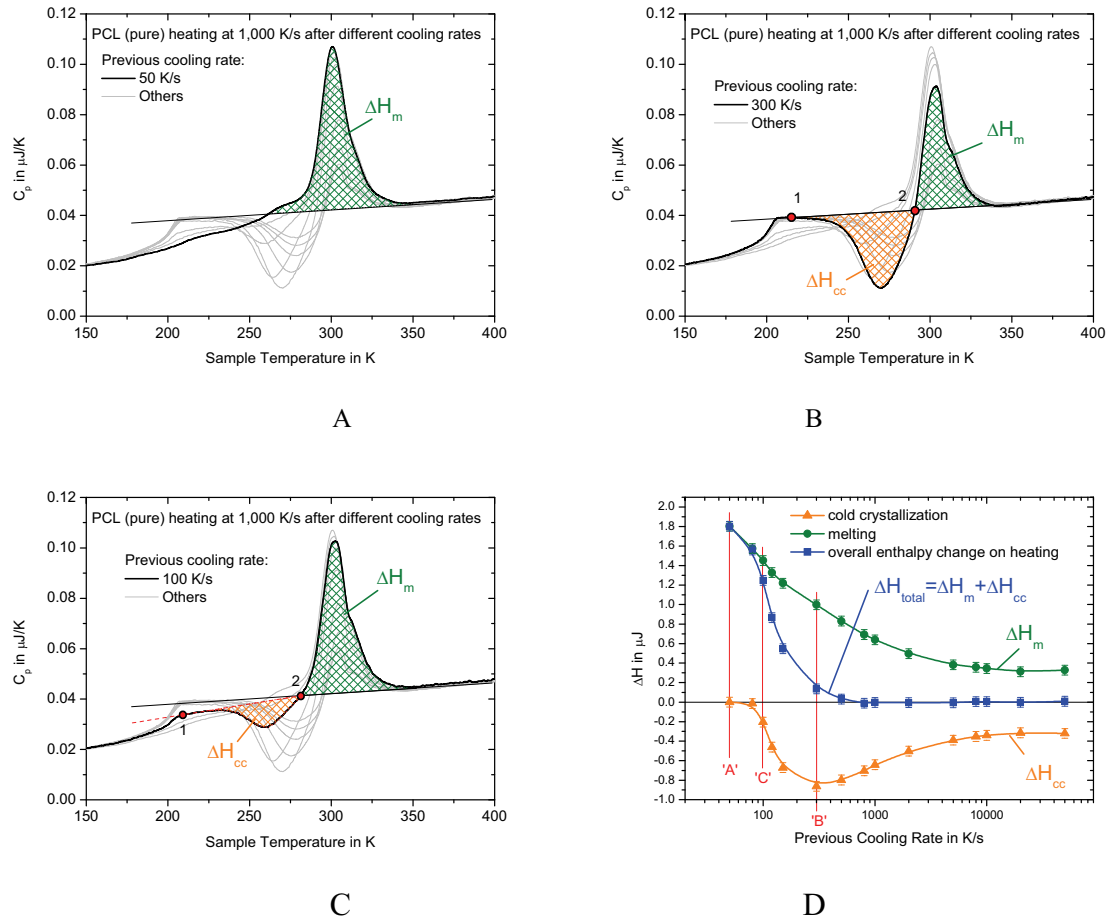


Figure 42. Determination of overall excess enthalpy change on heating and cold crystallization enthalpy after cooling at different rates. Base line construction for integration for different cases: A – melting only (fully crystallized), B – cold crystallization and melting after normal glass transition step (fully amorphous), C – cold crystallization and melting after reduced glass transition step (partly crystallized), for details see text. D – resulting enthalpies for heating after different rates.

At cooling rates higher than 300 K/s ('B' in Figure 42 D) a reduction of cold crystallization enthalpy is observed. This can be interpreted as a reduction of nucleation on cooling in analogy to Oguni et al. [2] and Mathot et al. [1] experiments (Figure 39). The reduction of cold crystallization on heating without crystallization on previous cooling was explained by a reduction of homogeneous nuclei formation and the saturation was explained by presence of unavoidable heterogeneous nuclei. To justify the latter assumption the same experiment was performed with a nucleated PCL. PCL with 0.2% MWCNT was prepared

from the same material as the first sample by melt mixing[#]. The resulting curves are shown in Figure 43.

Nucleated PCL crystallizes much faster. The overall enthalpy at heating becomes zero only after cooling at rates faster than 5,000 K/s showing that no crystallization happens before heating. The reduction of the peak after faster cooling is much less pronounced than in pure PCL. Maximum cold crystallization area for nucleated PCL is reached on heating after cooling at 2,000 K/s. It saturates at cooling faster then 50,000 K/s.

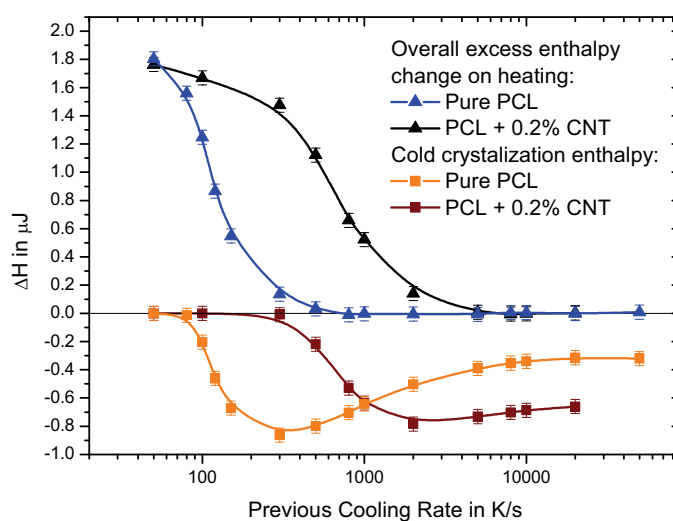


Figure 43. Overall excess enthalpy change and cold crystallization enthalpy on heating after cooling at different rates of pure (blue and orange) and nucleated (black and wine) PCL.

The fast cooling reveals a reduction of cold crystallization of pure PCL on successive heating. This reduction was explained to be caused by the absence of nuclei, which can grow into a crystal on heating. The saturation of the reduction on a non-zero value shows presence of nuclei that cannot be eliminated on cooling. The possible reason for that could be unavoidable heterogeneous nuclei (nucleation on surfaces or impurities). Even if we do not know the reason exactly, we call these nuclei heterogeneous. The effect of reduction of cold crystallization with increasing the rate was much smaller in nucleated PCL which confirms

[#] The samples were kindly provided by P. Pötschke, Leibniz-Institut für Polymerforschung Dresden e. V. Dresden, Teilinstitut Makromolekulare Chemie Abteilung Polymerreaktionen und Blends

the hypothesis of heterogeneous nucleation. The cold crystallization and overall enthalpy change on heating appears to be a good measure of the number of homogeneous nuclei and crystallinity of the material before heating.

5.3. Annealing experiments with PCL

The possibility to perform temperature treatment of the sample so fast that no homogeneous nucleation occurs was used to study the kinetics of nucleation under isothermal conditions. The scheme of the experiment performed is shown on Figure 44.

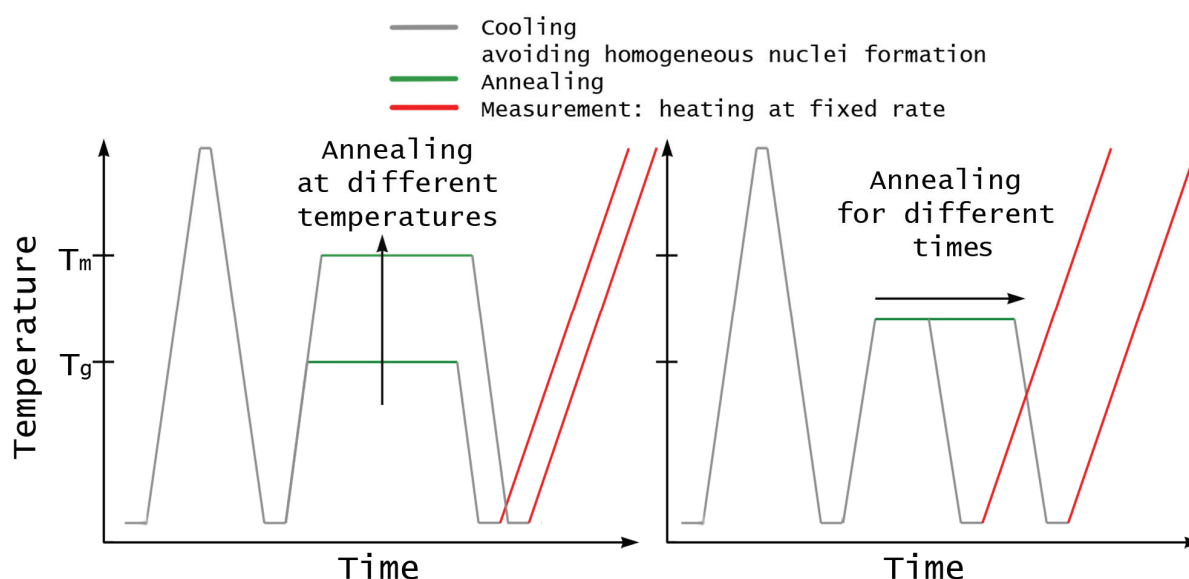


Figure 44. The annealing experimental program. Sample was melted and delivered to different annealing temperatures at high cooling and heating rates avoiding homogeneous nuclei formation (10,000 K/s). After annealing the sample was reheated from oven temperature at rate 1,000 K/s

The initial temperature was chosen 100 K which is 100 K below glass transition so that no processes can occur in the “frozen” sample within several milliseconds. To avoid even unlikely influences of annealing at this temperature the sample was held there for a fixed time of 0.1 s before annealing and before the heating scan, which was further evaluated. The sample was heated up to 470 K then cooled down to oven temperature at 10,000 K/s avoiding homogeneous nuclei formation. At the same rate it was heated to the annealing temperature and hold there for different times from 0.1 ms to 32 h. The heating at 1,000 K/s was used as

the measuring scan. Annealing was performed at fixed temperature for different times starting from 185 K ($T_g \sim 200$ K) and up to 330 K ($T_m \sim 340$ K).

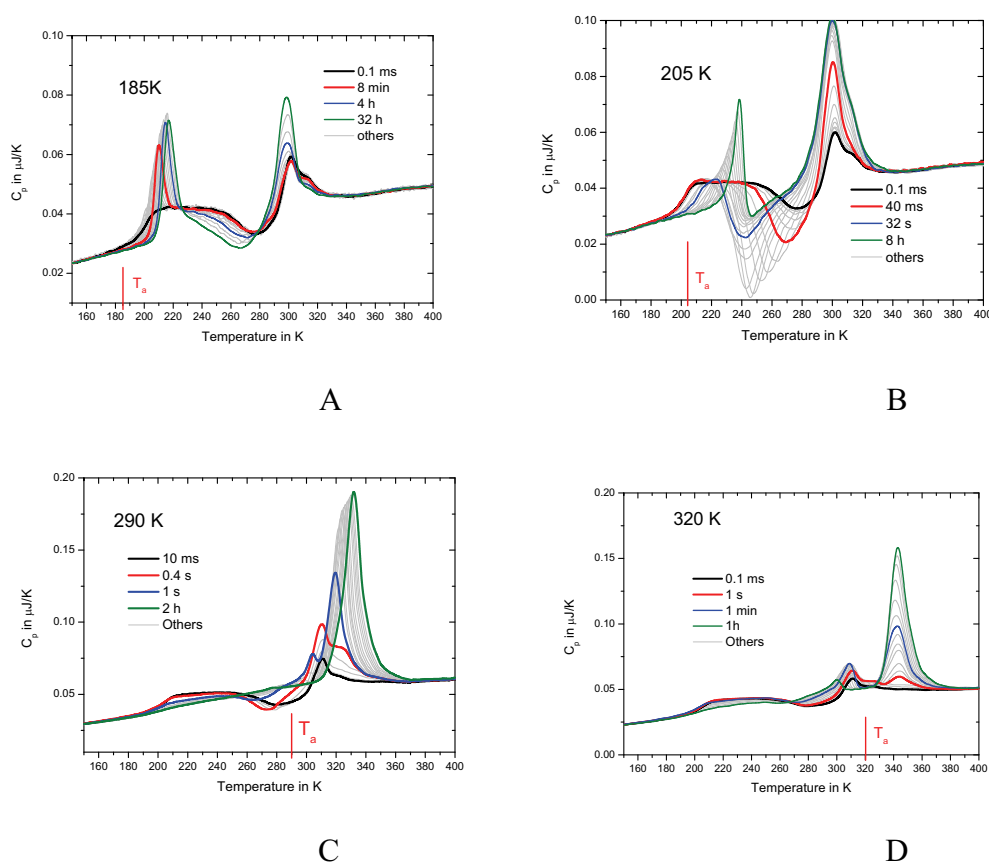


Figure 45. Series of heating curves after annealing at different temperatures for different times. Annealing close to T_g (A), near to T_m (D) and at intermediate temperatures (B and C). (All measured curves can be found in the [Appendix A1](#))

The resulting heating scans after annealing at several temperatures are shown in Figure 45. The development of nuclei and crystallization during annealing was traced by changes of glass transition, annealing peak, cold crystallization and melting on heating in analogy to the previously described experiments. The only difference to the experiment described in the previous chapter is that here the nuclei and crystal development is studied at particular temperatures for particular times, and under isothermal conditions.

The resulting total excess enthalpy change and cold crystallization enthalpy on heating for each annealing temperature was calculated and plotted versus annealing time in Figure 46.

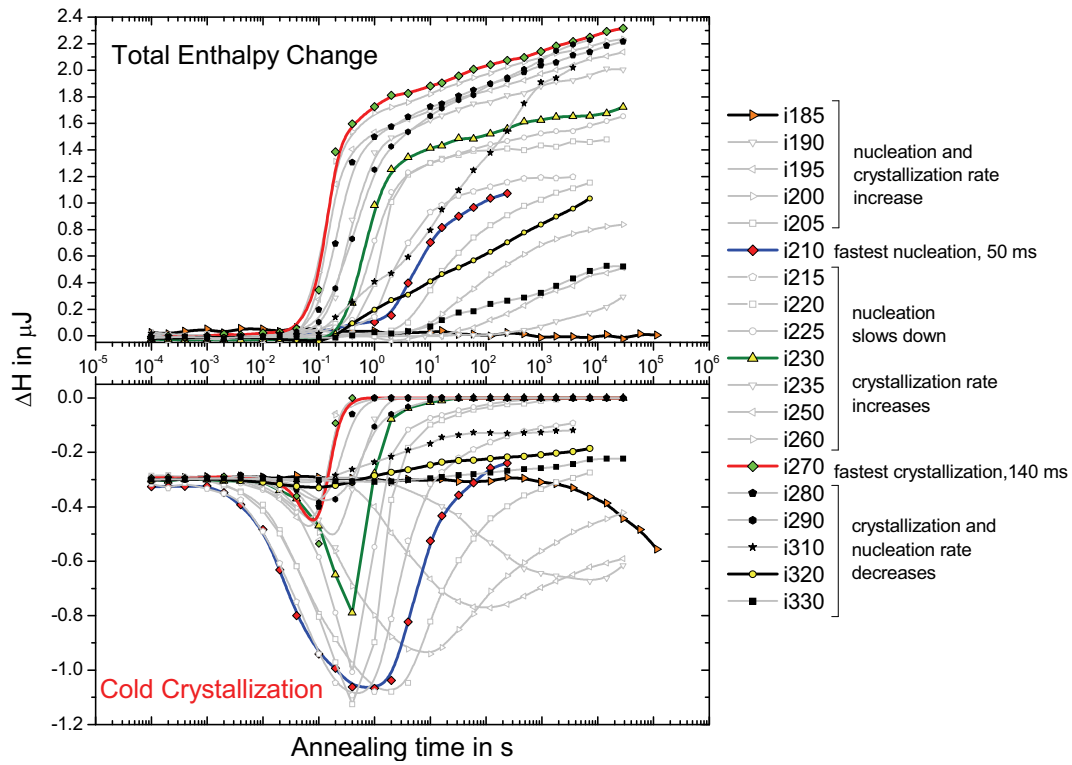


Figure 46. Cold crystallization and overall enthalpy change on heating for the annealing series. Each pair of curves corresponds to one annealing temperature (each point corresponds to a single measurement). The red curve shows the temperature with the highest crystallization rate (270 K). Curves with opened symbols were taken at temperatures below 270 K, filled symbols – above 270 K.

The overall enthalpy changes show the typical crystallization kinetics. When there is nothing crystallized on cooling everything that is crystallized on heating also melts after that making total enthalpy change on heating, $\Delta H_{heating} = \Delta H_{cc} + \Delta H_{melting_cc} = 0$. When the sample crystallizes during annealing $\Delta H_{heating}$ becomes positive due to additional melting of isothermally crystallized material:

$$\Delta H_{heating} = (\Delta H_{cc} + \Delta H_{melting_cc}) + \Delta H_{melting_iso} \quad (5.1)$$

The presence of additional melting is supported by the observation of an additional enhancement of melting peak on heating. Therefore, following $\Delta H_{heating}$ one can indirectly observe isothermal crystallization kinetics.

In general, the cold crystallization peak area shows first always a constant value due to unavoidable heterogeneous nucleation then growth due to the formation of homogeneous nuclei during annealing and then it decays due to crystallization on annealing. The presence of a ‘nucleation’ peak in the cold crystallization enthalpy curves is visible up to 290 K, being a

measure of time separation between nuclei creation and the growth processes. For the temperature range up to 230 K the nucleation saturates even before crystallization is seen in the total enthalpy change.

Assuming two independent processes are seen in the curves allows us to study their kinetics and to compare them in an activation diagram.

5.4. Characteristic time of nucleation and crystallization at different temperatures

For the description of both processes, nucleation and crystallization, an Avrami function was used. It is traditionally applied to describe the formation of a new phase inside the material. The volume fraction of converted material at any moment after starting the process is

$$\alpha = 1 - \exp(-Kt^n) \quad (5.2)$$

where K – transformation rate and n – Avrami coefficient including the dimensionality of the process. Assuming the half time of the process as $\tau = (\ln 2 / K)^{1/n}$, the resulting expression of process kinetics via half time is

$$\alpha = 1 - \exp(-\ln 2 (t / \tau)^n) \quad (5.3)$$

The enthalpy change on heating, which equals the enthalpy change during isothermal crystallization, ΔH_c , can be expressed then as

$$\Delta H_c = \Delta H_{\infty} \left(1 - \exp \left(-\frac{t}{\tau_c} \ln 2 \right)^{n_c} \right) \quad (5.4)$$

where ΔH_{∞} is final enthalpy of crystallization at infinite time, t is annealing time, τ_c – crystallization half time and n_c – Avrami coefficient of crystallization. Taking into account a linear increase of enthalpy due to secondary crystallization yields:

$$\Delta H_c = \Delta H_{\infty} \left(1 - \exp \left(-\frac{t}{\tau_c} \ln 2 \right)^{n_c} \right) + A_2 (\ln(t - \tau_c)) \left(\frac{1}{2} \left(\frac{|t - \tau_c|}{t - \tau_c} + 1 \right) \right) \quad (5.5)$$

where ΔH_{∞} – total increase of enthalpy due to crystallinity that can be developed during primary crystallization and A_2 – secondary crystallization parameter.

The homogeneous nucleation process for the first approximation can also be described using an Avrami equation.

$$\Delta H_n = \Delta H_{\text{nhom}\infty} \left(1 - \exp \left(- \frac{t}{\tau_n} \ln 2 \right)^2 \right) + \Delta H_{\text{nhet}} \quad (5.6)$$

where τ_n – nucleation half time, ΔH_{nhet} – enthalpy change during cold crystallization at this heating rate on heterogeneities, $\Delta H_{\text{nhom}\infty}$ – total enthalpy change of homogeneous crystallization.

The development of the cold crystallization peak represents the kinetics of nuclei formation (first increase of the peak with annealing time) and crystallization during isothermal treatment (decrease of the peak at longer annealing time). Therefore the peak area can be considered as the sum of two parts of opposite sign:

$$\Delta H_{cc} = -\Delta H_n + \Delta H_c \quad (5.7)$$

The second term is the same as for the overall enthalpy change (crystallinity) and consequently ΔH_n can be obtained from a simultaneous fit of both curves. Such simultaneous fit of two measured curves with two functions is shown in Figure 47. For simplicity of representation the secondary crystallization term is not shown on the bottom part although it was used in the real fit.

Several assumptions are used to improve fitting convergence. First n_n and n_c were restricted in between 2 and 4 because it denotes the dimensionality of the process plus one. The total cold crystallization enthalpy limit ($\Delta H_{\text{nhom}\infty} + \Delta H_{\text{nhet}}$) was restricted to ΔH_{∞} manually at the first fitting iterations as well as A_2 was restricted to 0. After several iterations, when the parameters τ_n and τ_c were determined, the parameters of the fit were released and the fit repeated until convergence.

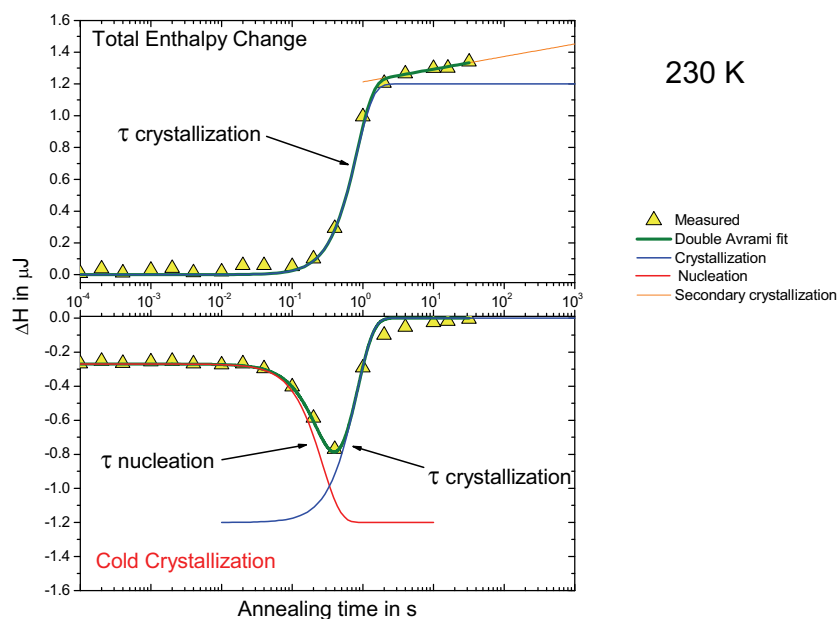


Figure 47. Simultaneous fit of overall excess enthalpy change and crystallization enthalpy on heating by a double Avrami fit, for details see text.

For 185 K the nucleation time constant was determined using a simple Avrami kinetics and $(\Delta H_{\text{nhom}\infty} + \Delta H_{\text{nhet}}) = 2 \mu\text{J}$ as final crystallization enthalpy. The crystallization time constant was extrapolated using the achieved nucleation time and previous results for crystallization time. The correspondingly expected large error is indicated in the final results below.

The obtained time constants of crystal nucleation and overall crystallization (growth) were plotted on an activation diagram (Figure 48).

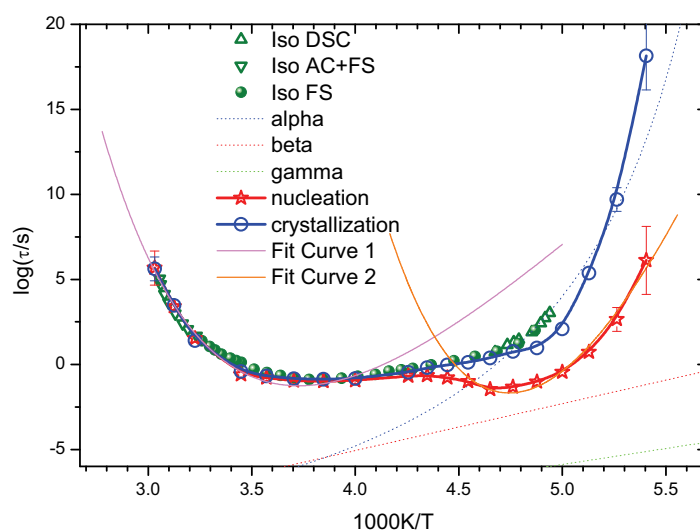


Figure 48. Activation diagram for nucleation and crystallization processes at temperatures from below glass transition up to melting temperature and 20 orders of magnitude time range. They are compared to dielectric relaxation data (dashed curves) and isothermal experiments [25] on single sensor device (green spheres) [63].

As seen from the picture the nucleation at low temperatures is ca. 2 orders of magnitude faster than crystallization, but still both processes follow the α -relaxation curve tendency. At higher temperatures crystallization occurs immediately when nucleation occurs.

The cold crystallization and overall enthalpy change on heating were used as a measure of crystal nucleation and growth respectively. The cold crystallization peak area as a superposition of effects due to crystal nucleation and growth during annealing was found to be sensitive to the time delay between these two processes. The time separation is followed up to 290 K after that crystallization happens almost immediately after nucleation.

A double Avrami function was used to find the time constants of each of the two processes. The final results cover the full temperature range where crystallization occurs: from 185 K ($T_g = 209$ K) to 340 K ($T_m = 342$ K). The estimated time constants covers the range from $3 \cdot 10^{-2}$ s (nucleation at 215 K) to $3 \cdot 10^9$ s (crystallization at 185 K).

6. Discussion

The aim of the study was to investigate simultaneously nucleation and overall crystallization under isothermal conditions in a wide range of temperatures using the ability of a fast temperature scanning device to avoid both nucleation and crystallization on cooling from the melt. The newly developed fast scanning calorimeter was able to perform fast enough temperature scans avoiding crystallization and homogeneous nuclei formation on cooling to far below the glass transition.

Cold crystallization enthalpy at a constant intermediate heating rate was used as a measure for the number of previously formed nuclei and the overall excess enthalpy change on heating – as a measure of crystallinity formed on preceding cooling. If the sample was amorphous it would show zero overall enthalpy change on heating but cold crystallization enthalpy as well as melting enthalpy then depend on the number of over-critical nuclei in the sample. Because of the same heating rate was used for all experiments the rate-dependent errors were minimized and only the changes due to the different thermal histories were detected and compared.

To understand what exactly was detected on heating the overall excess enthalpy change and cold crystallization enthalpy on heating is shown in Figure 49 versus cooling rate of the preceding cooling from the melt. The cooling itself is shown schematically in Figure 50 in respect to half-time of crystal nucleation and overall crystallization which are the final aim of our investigation.

Depending on previous heat treatment (cooling at different rates in this case) the next heating shows distinct regions which allow an assignment of different processes occurring, which were depending on cooling rate. Three different regions can be identified: 1 – the sample was fully crystallized during previous heat treatment (here slow cooling, region 1 in Figure 49 and Figure 50), 2.1 – the sample was only partly crystallized but over-critical nuclei were formed on previous heat treatment and started to grow on heating (cold crystallization), 2.2 – the sample remained amorphous after the previous heat treatment and only homogeneous nuclei were formed before heating, and 3 – no crystals and no over-critical nuclei were formed during the previous heat treatment.

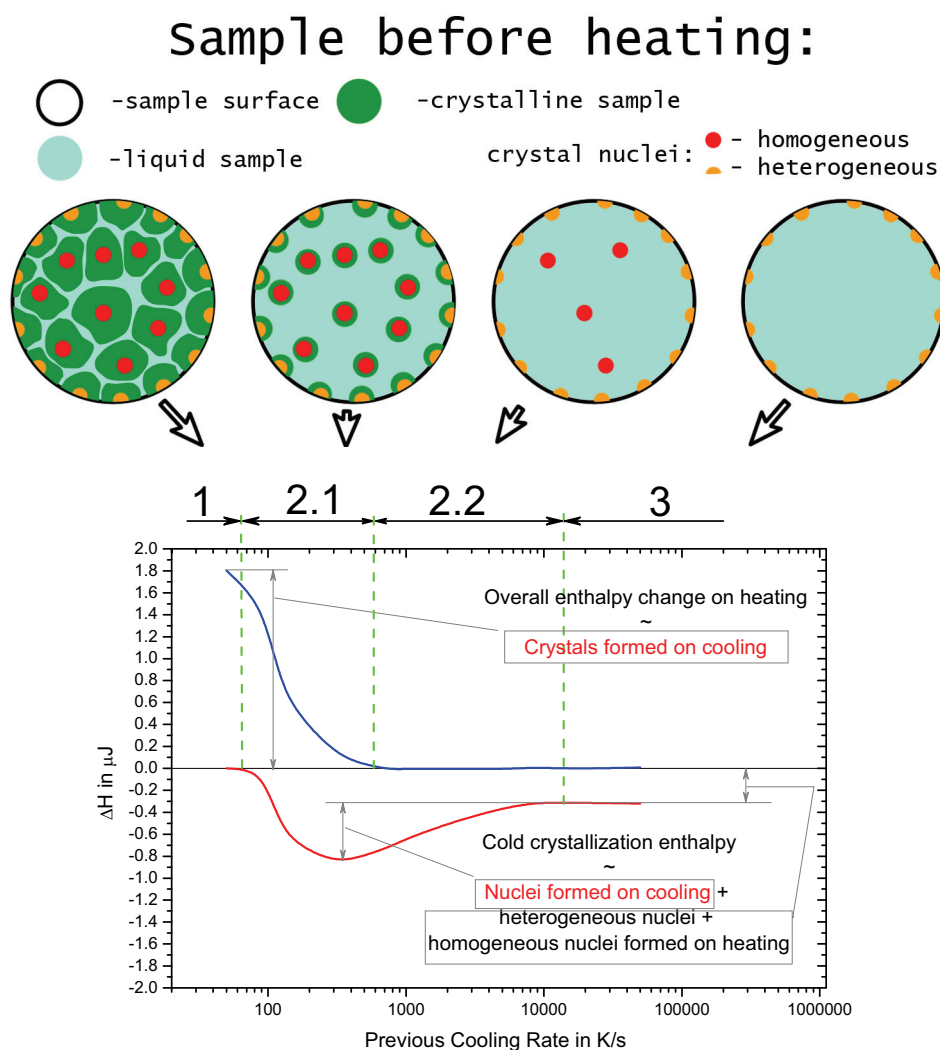


Figure 49. Overall excess enthalpy change and cold crystallization enthalpy on heating at 1,000 K/s as a function of preceding cooling rate, see Figure 42. For details see text.

Before heating, the material was fully amorphous with only a few unavoidable heterogeneous nuclei. In zone 2.2 the sample has zero total enthalpy change on heating, which means no crystallinity was formed on previous cooling, but the cold crystallization peak undergoes a reduction with increasing cooling rate. The reduction of the cold crystallization peak with increasing cooling rate supports the idea of a reduction of the number of homogeneous nuclei formed on previous heat treatment. The saturation of the reduction at a certain level, different from zero, (zone 3, Figure 49 and Figure 50) shows the presence of unavoidable nuclei that includes heterogeneous nuclei (including surface nucleation) and homogeneous nucleation that occurs on heating. This allows us to study the formation of homogeneous nuclei, which we were able to avoid on cooling on further heat treatment.

Saturation in zone '3' shows that this group of nuclei is finite and constant in this sample under the chosen experimental conditions. Since this group of nuclei is formed by homogeneous nucleation, we will be able to study homogeneous nucleation on further heat treatments.

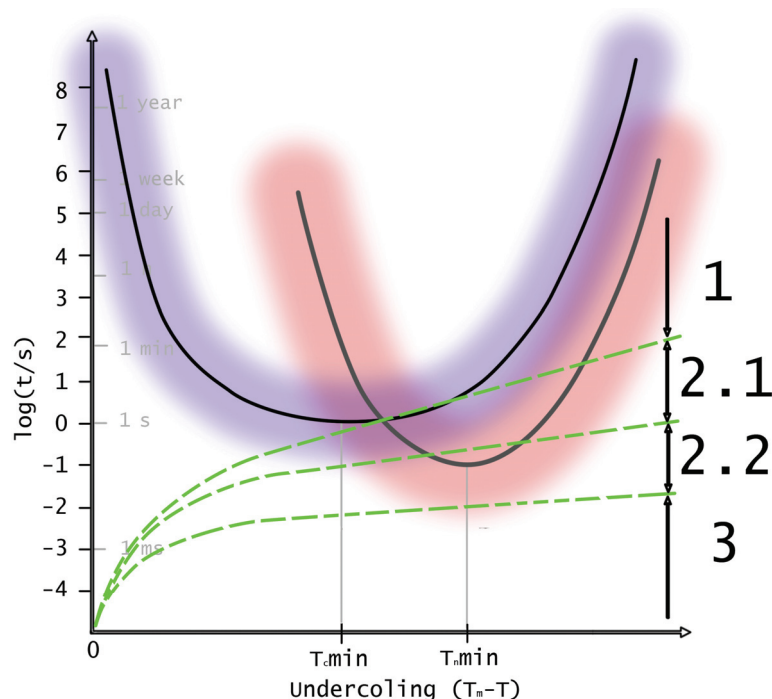


Figure 50. Nucleation (grey curve) and overall crystallization (black curve) half-time versus under-cooling temperature and curves showing linear cooling from the melt (dashed green curves). Region 1 – 3 corresponds to same regions in Figure 49.

Two major results, which were important for this study, were taken from this experiment:

- The heating scan can be used as a relative measure of the number of previously formed overcritical homogeneous nuclei and sample crystallinity by evaluating cold crystallization and total excess enthalpy change on heating, respectively.
- The system allows one to perform temperature scan avoiding not only crystallization, but also homogeneous nucleation on cooling for PCL.

Being able to avoid formation of overcritical nuclei at fast cooling allows us to study isothermally homogeneous nuclei formation and crystallization, both at the same temperature, by evaluating the heating scans, which were always collected at the same rate as shown in Figure 44 above.

Isothermal annealing experiments were performed in the temperature ranging from below glass transition up to melting temperature. The aim was to determine half-time of the processes of nucleation and overall crystallization at these temperatures. The Avrami equation, commonly applied for crystallization processes, was used to fit the overall excess enthalpy change curves in order to determine the crystallization half-time for each annealing temperature. The resulting parameters were simultaneously used to fit the cold crystallization enthalpy curve, which includes both nucleation and overall crystallization kinetics (Figure 47). Nucleation half-time was determined also using Avrami equation, which was based on the fact that this equation describes transformation of the material in the finite volume and assuming constant nucleation rate. The obtained nucleation and crystallization time constants were shown in the activation diagram in Figure 48 and again versus annealing temperature in Figure 51.

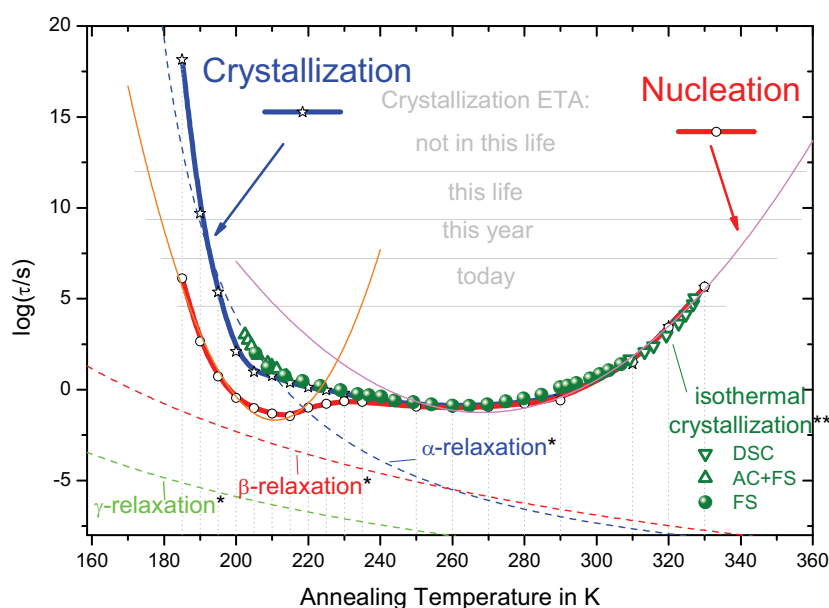


Figure 51. Crystal nucleation (thick red curve) and overall crystallization half-time (thick blue curve) at different temperatures. Data (**) measured previously by Adamovsky [63] using AC and single sensor fast scanning calorimeter – green symbols. Dashed curves (*) designates dielectric relaxation data from e.g. [25].

It is shown in Figure 51 that the newly measured crystallization kinetics coincides nicely with the previous study showing the kinetics discontinuity around 230-235 K [63]. The new data illustrates the faster kinetics in the low temperature region. The reason for faster crystallization at low temperatures can be homogeneous nucleation which dominates at low

temperatures (see red curve below 230 K). The low temperature part of the nucleation curve is connected with homogeneous nucleation whereas the high temperature part corresponds to the activation time of heterogeneous nuclei. In the high temperature region, where the thermodynamic force for crystallization is low but mobility is high, the sample crystallizes as soon as nucleation occurs. Even the separation between nucleation and crystallization is seen up to 290 K (Figure 46), it became significantly separated at low temperatures only.

Special attention requires the crystallization at temperatures below the glass transition. In Figure 52A the heating after annealing at 195 K for different times is shown. The peak that is normally referred as enthalpy relaxation is shown in Figure 52B. The peak and corresponding glass transition step evolution with annealing time showed that what is seen could be not only the enthalpy relaxation, but also superposition of enthalpy relaxation and melting. The suppression of the glass transition step was also observed for long annealing times.

A quantitative evaluation of the peak area was performed for a better understanding of the effect. The peak was integrated vs. heating without annealing (black curve in Figure 52B). The result of integration versus annealing time is shown in Figure 52C. For comparison the maximum value of enthalpy relaxation at this temperature is given ($\Delta H_{\max} = \Delta C_p (T_g - T_m)$, black horizontal line in Figure 52C). It is clearly seen that after 1000 s the area of the peak becomes larger than possible due to enthalpy relaxation, therefore melting must be considered too.

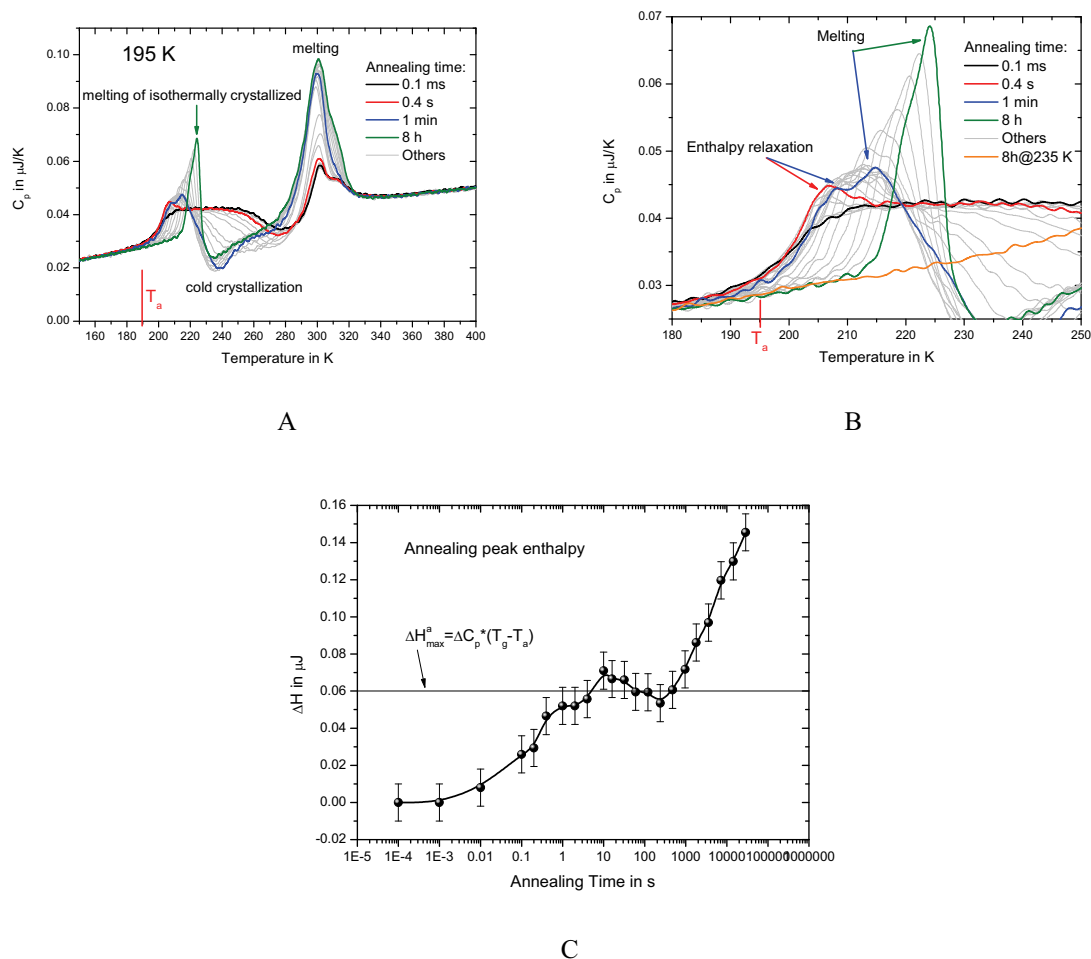


Figure 52. The heating after annealing at 195 K (A). Evolution of annealing peak with annealing time – B. For comparison the curve of material crystallized for 8 h at 235 K is given. The annealing peak enthalpy – C (integrated against heating of fully amorphous material without annealing, see black curve on B).

Superposition of enthalpy relaxation and melting occurs on heating. The presence of a relatively small melting peak (ca. 4 % crystallinity) depresses the glass transition in a way as it is observed for the fully crystalline material. This confirms the creation of a large amount of rigid amorphous material around a large number of tiny crystals. After annealing at 185 K (Figure 45A), which is lower than glass transition, the enthalpy relaxation peak is also observed. For longer annealing times it is superimposed by melting of isothermally formed crystals.

The temperature of the first melting peak was plotted versus temperature of crystallization (Figure 53B). The data are not in an agreement with common understanding and DSC data (black point in Figure 53 B). The blue line, along which the melting points are situated is in parallel to the line $T_m = T_c$, which was also observed previously for PET and iPP

(Figure 53 C, D). According to classical theory this line (blue) should intersect with the black line at the equilibrium melting temperature (Hoffman-Weeks plot [95]), which is commonly observed for DSC data. The observed effect could not be explained by the size of the sample, which was 50 – 80 μm . The discrepancy between DSC and fast scanning melting data is not yet understood and needs further investigation. Most probably, this is connected with the size effects in terms of relation between surface and bulk volume of the sample.

There is another unexpected observation in this data, while isothermally formed crystals for longer annealing times at low temperatures melt before the cold crystallization peak, it seems that the nuclei formed at small annealing times survive until cold crystallization. This causes significant changes in the enthalpy of cold crystallization, and may be explained by a stabilization of the nuclei that should occur much faster than stabilization of crystals. This needs further investigations, especially for other polymers. Similar observations were made by Kanaya et al. [96-97] where they studied shear induced nucleation in iPS by depolarized light scattering (DPLS) and polarized optical microscopy (POM). It was found that an anisotropic oriented structure on an μm scale was formed even above the equilibrium melting temperature and survives at least for 1 h.

Using the new technique we were able to follow crystallization kinetics in a wide range of temperatures and times. The nucleation kinetics was measured simultaneously at the same temperature as crystallization. The crystallization follows the α -relaxation in the activation diagram at low temperatures confirming that crystallization is diffusion controlled there. The nucleation at low temperatures is assumed to have homogeneous origin and is two orders of magnitude faster than crystallization. It is positioned in-between α - and β -relaxation in agreement with Oguni's observations [40] but in contradiction to them it follows the trace of the α -process.

The classical polymer crystallization theory does not give an insight in the processes taking place during very early stages of crystallization. One of the new models on this subject was proposed by Muthukumar [16]. Based on molecular simulation data he showed that the organization of the nucleus occurs in several steps and requires significant time before crystal growth starts. This was found to be in agreement with our data. The crystallization shows significant, up to 2 orders of magnitude, delay after nucleation occurs. It is seen from e.g. Figure 47 that when the nucleation is almost finalized, the crystallization is just begins. In this way the newly developed instrument allows verifying existing theories for polymer nucleation and crystallization and may contribute to further improvements of the theory.

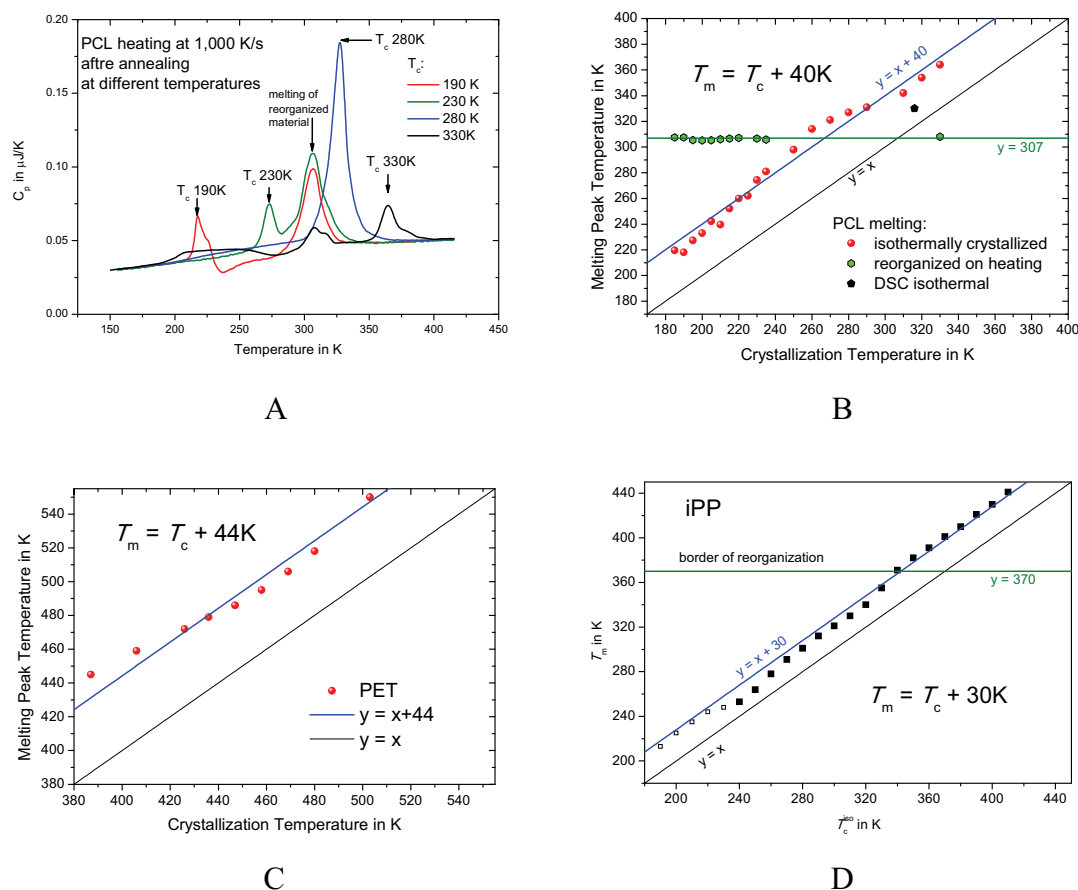


Figure 53. Melting peak temperature of isothermally grown crystals (B – D) and the way it was determined on heating at 1000 K/s after annealing (A).

For the further research it will be of high interest to obtain similar activation diagrams for nucleated samples especially in the low temperature region where homogeneous nucleation dominates in the pure PCL.

Estimations of physical properties of the observed structures are of interest as well. Taking into account the fact that the nuclei are more stable than some crystals (annealing at 195 K in Figure 52) the experimental observation should be possible. For that one need the combined setup that can perform scattering or spectroscopic observations in nanogram samples and at the same time allows advanced temperature treatment of the sample.

7. Summary

Crystallization, as well as in polymers, is commonly considered as nucleation followed by a growth process. Nevertheless, a complete description of polymer crystallization is far from being achieved. Several theories are in contradiction with experiments. Often a decisive conclusion regarding the validity of a theory is not possible because of a lack of appropriate experiments. Therefore one should also think about the development of appropriate instrumentation. In this work a new experimental technique for temperature control of the sample and determination of its heat capacity during temperature treatment at high cooling and heating rates was developed. Both, crystal nucleation and growth characteristic times were determined simultaneously in the range of temperatures where crystallization occurs – from below glass transition up to equilibrium melting temperature.

The setup developed in this work has opened new possibilities to shed light on the processes of polymer crystal nucleation and growth. The fast scanning calorimeter possesses a large dynamic range in combination with the possibility of an extended quantitative interpretation of the measured data. In this work it was utilized for the investigation of both crystal nucleation and growth kinetics of poly(ϵ -caprolactone) in a wide range of temperatures and times. The measurement of nucleation as a part of crystallization was of special interest in this work.

The crystallization was studied starting from below glass transition up to melting temperature, for time scale from 10^{-2} to 10^5 s. The homogeneous nucleation was studied simultaneously with crystallization in the same range of temperatures. The study provides new information about crystal nucleation and overall crystallization in the polymer which was not available before.

8. References

- [1] M. SalmeronSanchez, V.B.F. Mathot, G. VandenPoel, J.L. GomezRibelles, Effect of the Cooling Rate on the Nucleation Kinetics of Poly(L-Lactic Acid) and Its Influence on Morphology, *Macromolecules*, 40 (2007) 7989-7997.
- [2] N. Okamoto, M. Oguni, Discovery of Crystal Nucleation Proceeding Much Below the Glass Transition Temperature in a Supercooled Liquid, *Solid State Commun.*, 99 (1996) 53-56.
- [3] S. Vyazovkin, I. Dranca, Effect of Physical Aging on Nucleation of Amorphous Indomethacin, *Journal of Physical Chemistry B*, 111 (2007) 7283-7287.
- [4] I. Gutzow, J. Schmelzer, *The Vitreous State, Kinetics of Homogeneous Nucleation* (1995).
- [5] A.A. Minakov, C. Schick, Ultrafast Thermal Processing and Nanocalorimetry at Heating and Cooling Rates up to 1 MK/s, *Rev. Sci. Instr.*, 78 (2007) 073902-073910.
- [6] J.W.P. Schmelzer, Crystal Nucleation and Growth in Glass-forming Melts: Experiment and Theory, *J. Non-Crystal. Solids*, 354 (2008) 269-278.
- [7] V.V. Slezov, J. Schmelzer, Y.Y. Tkatch, Number of Clusters Formed in Nucleation-Growth Processes, *Chem. Phys.*, 105 (1996) 8340-8351.
- [8] P. Sajkiewicz, M.L.D. Lorenzo, A. Gradys, Transient Nucleation in Isothermal Crystallization of Poly(3-hydroxybutyrate), *e-Polymers*, 085 (2009) 1-16.
- [9] I. Gutzow, J. Schmelzer, A. Dobрева, Kinetics of Transient Nucleation in Glass-forming Liquids: a Retrospective and Recent Results, *J. Non-Cryst. Solids*, 219 (1997) 1-16.
- [10] B. Lotz, Crystallographic and Structural Roots of Variation in Polymer Morphology, *Phil. Trans. R. Soc. Lond. A*, 348 (1994) 19-28.
- [11] J.D. Hoffman, G.T. Davis, J.I. Lauritzen, *Crystalline and Noncrystalline Solids*, Plenum Press, 1976.
- [12] J.P. Armistead, J.D. Hoffman, Direct Evidence of Regimes I, II, and III in Linear Polyethylene Fractions As Revealed by Spherulite Growth Rates, *Macromolecules*, 35 (2002) 3895-3913.

- [13] J.D. Hoffmann, Regime III Crystallization in Melt-crystallized Polymers: the Variable Cluster Model of Chain Folding, *Polymer*, 24 (1983) 3-26.
- [14] D.M. Sadler, G.H. Gilmer, Rate-Theory Model of Polymer Crystallization, *Phys. Rev. Lett.*, 56 (1986) 2708-2712.
- [15] G. Strobl, A Multiphase Model Describing Polymer Crystallization and Melting, in: *Progress in Understanding of Polymer Crystallization*, 714 (2007) 481-502.
- [16] M. Muthukumar, Modeling Polymer Crystallization, *Adv Polym Sci*, 191 (2005) 241-274.
- [17] M. Avrami, General Theory, *J. Chem. Phys.*, 7 (1939) 1103-1112.
- [18] A.T. Lorenzo, M.L. Arnal, J. Albuérne, A.J. Müller, DSC Isothermal Polymer Crystallization Kinetics Measurements and the Use of the Avrami Equation to Fit the Data: Guidelines to Avoid Common Problems, *Polymer Testing*, 26 (2007) 222-231.
- [19] T. Ozawa, Kinetics of Non-isothermal Crystallization, *Polymer*, 12 (1971) 150-158.
- [20] T. Albrecht, G. Strobl, Observation of the Early Stages of Crystallization in Polyethylene by Time-Dependent SAXS: Transition from Individual Crystals to Stacks of Lamellae, *Macromolecules*, 29 (1996) 783-785.
- [21] B. Heck, T. Hugel, M. Iijima, E. Sadiko, G. Strobl, Steps in the Transition of an Entangled Polymer Melt to the Partially Crystalline State, *New J. Phys.*, 1 (1999) 17.11-17.29.
- [22] T. Hippler, S. Jiang, G. Strobl, Block Formation during Polymer Crystallization, *Macromolecules*, 38 (2005) 9396-9397.
- [23] T.Y. Cho, G. Strobl, Temperature Dependent Variations in the Lamellar Structure of Poly(L-lactide), *Polymer*, 47 (2006) 1036-1043.
- [24] L. Kailas, C. Vasilev, J.N. Audinot, H.N. Migeon, J.K. Hobbs, A Real-Time Study of Homogeneous Nucleation, Growth, and Phase Transformations in Nanodroplets of Low Molecular Weight Isotactic Polypropylene Using AFM, *Macromolecules*, 40 (2007) 7223-7230.
- [25] A. Wurm, R. Soliman, C. Schick, Early Stages of Polymer Crystallization – A Dielectric Stud, *Polymer*, 44 (2003) 7467-7476.
- [26] M. Imai, K. Kaji, T. Kanaya, Structural Formation of Poly(ethylene terephthalate) during the Induction Period of Crystallization. 3. Evolution of Density Fluctuations to Lamellar Crystal, *Macromolecules*, 27 (1994) 7103-7108.

- [27] M. Imai, K. Mori, T. Mizukami, K. Kaji, T. Kanaya, Structural Formation of Poly(ethylene terephthalate) During the Induction Period of Crystallization: 1. Ordered Structure Appearing Before Crystal Nucleation, *Polymer*, 33 (1992) 4451-4456.
- [28] G. Matsuba, K. Kaji, K. Nishida, T. Kanaya, M. Imai, Conformational Change and Orientation Fluctuations Prior to the Crystallization of Syndiotactic Polystyrene, *Macromolecules*, 32 (1999) 8932-8937.
- [29] V. Brucato, S. Piccarolo, V. La Carrubba, An Experimental Methodology to Study Polymer Crystallization under Processing Conditions. The Influence of High Cooling Rates, *Chem. Eng. Sci.*, 57 (2002) 4129-4143.
- [30] O. Zia, R. Androsch, H.J. Radusch, S. Piccarolo, Morphology, Reorganization and Stability of Mesomorphic Nanocrystals in Isotactic Polypropylene, *Polymer*, 47 (2006) 8163-8172.
- [31] A. Gradys, P. Sajkiewicz, A.A. Minakov, S. Adamovsky, C. Schick, T. Hashimoto, K. Saijo, Crystallization of Polypropylene at Various Cooling Rates, *Mater. Sci. Eng. A*, 413-414 (2005) 442-446.
- [32] A. Gradys, P. Sajkiewicz, S. Adamovsky, A. Minakov, C. Schick, Crystallization of poly(vinylidene fluoride) during ultra-fast cooling, *Thermochim. Acta*, 461 (2007) 153-157.
- [33] F. De Santis, S. Adamovsky, G. Titomanlio, C. Schick, Scanning Nanocalorimetry at High Cooling Rate of Isotactic Polypropylene, *Macromolecules*, 39 (2006) 2562-2567.
- [34] F. De Santis, S. Adamovsky, G. Titomanlio, C. Schick, Isothermal Nanocalorimetry of isotactic polypropylene, *Macromolecules*, 40 (2007) 9026-9031.
- [35] V.V. Ray, A.K. Bantia, C. Schick, Fast Isothermal Calorimetry of Modified Polypropylene Clay Nanocomposites, *Polymer*, 48 (2007) 2404-2414.
- [36] C. Silvestre, S. Cimmino, D. Duraccio, C. Schick, Isothermal Crystallization of Isotactic Poly(propylene) Studied by Superfast Calorimetry, *Macromol. Rapid Commun.*, 28 (2007) 875-881.
- [37] P. Supaphol, J.E. Spruiell, Isothermal Melt- and Cold-crystallization Kinetics and Subsequent Melting Behavior in Syndiotactic Polypropylene: a Differential Scanning Calorimetry Study, *Polymer*, 42 (2001) 699-712.
- [38] G. Tammann, *Der Glaszustand*, Leopold Voss, Leipzig, 1933.
- [39] F. Paladi, M. Oguni, Anomalous Generation and Extinction of Crystal Nuclei in Nonequilibrium Supercooled Liquid o-benzylphenol, *Phys. Rev. B: Condens. Matter Mater. Phys.*, 65 (2002) 144201-144206.

- [40] M. Oguni, Intra-Cluster Rearrangement Model for the Alpha-Process in Supercooled Liquids, as Opposed to Cooperative Rearrangement of Whole Molecules Within a Cluster, *J. Non-Cryst. Solids*, 210 (1997) 171-177.
- [41] D.W. Denlinger, E.N. Abarra, K. Allen, P.W. Rooney, M.T. Messer, S.K. Watson, F. Hellman, Thin-film Microcalorimeter for Heat Capacity Measurements from 1.5-K TO 800-K, *Rev. Sci. Instrum.*, 65 (1994) 946-958.
- [42] S.L. Lai, G. Ramanath, L.H. Allen, P. Infante, Z. Ma, High-speed (10(4)-degrees-C/S) Scanning Microcalorimetry with Monolayer Sensitivity (J/M(2)), *Appl. Phys. Lett.*, 67 (1995) 1229-1231.
- [43] Y. Efremov, E.A. Olson, M. Zhang, S.L. Lai, F. Schiettekatte, Z.S. Zhang, L.H. Allen, Thin-Film MEMS Differential Scanning Nanocalorimetry: Heat Capacity Analysis, *Thermochim. Acta*, 412 (2004) 13-23.
- [44] A.A. Minakov, S.A. Adamovsky, C. Schick, Non Adiabatic Thin-film (Chip) Nanocalorimetry, *Thermochim. Acta*, 432 (2005) 177-185.
- [45] A.F. Lopeandia, L.I. Cerdo, M.T. Clavaguera-Mora, L.R. Arana, K.F. Jensen, F.J. Munoz, J. Rodriguez-Viejo, Sensitive Power Compensated Scanning Calorimeter for Analysis of Phase Transformations in Small Samples, *Rev. Sci. Instr.*, 76 (2005) 065104-065105.
- [46] A. Minakov, S. Adamovsky, C. Schick, Ultra Fast Calorimetry on Controlled Cooling and Heating up to 10,000 K/s and Isothermally with Millisecond Time Resolution (Poster), *e-Polymers*, P001 (2003).
- [47] A. Minakov, J. Morikawa, T. Hashimoto, H. Huth, C. Schick, Temperature Distribution in a Thin-film Chip Utilized for Advanced Nanocalorimetry, *Meas. Sci. Technol.*, 17 (2006) 199-207.
- [48] S.A. Adamovsky, A.A. Minakov, C. Schick, Scanning Microcalorimetry at High Cooling Rate, *Thermochim. Acta*, 403 (2003) 55-63.
- [49] A.A. Minakov, D.A. Mordvintsev, C. Schick, Melting and Reorganization of Poly(ethylene Terephthalate) on Fast Heating (1,000 K/s), *Polymer*, 45 (2004) 3755-3763.
- [50] A.A. Minakov, D.A. Mordvintsev, C. Schick, Isothermal Reorganization of Poly(ethylene terephthalate) Revealed by Fast Calorimetry (1000 K s⁻¹; 5 ms), *Faraday Discuss.*, 128 (2005) 261-270.
- [51] A.A. Minakov, D.A. Mordvintsev, R. Tol, C. Schick, Melting and Reorganization of the Crystalline Fraction and Relaxation of the Rigid Amorphous Fraction of Isotactic Polystyrene on Fast Heating (30,000 K/min), *Thermochim. Acta*, 442 (2006) 25-30.

- [52] A. Krumme, A. Lehtinen, S. Adamovsky, C. Schick, J. Roots, A. Viikna, Crystallization Behavior of Some Unimodal and Bimodal Linear Low-density Polyethylenes at Moderate and High Supercooling, *Journal of Polymer Science Part B: Polymer Physics*, 46 (2008) 1577-1588.
- [53] C. Schick, Differential Scanning Calorimetry (DSC) of Semicrystalline Polymers, *Analytical and Bioanalytical Chemistry*, 395 (2009) 1589 - 1611.
- [54] M. Pyda, E. Nowak-Pyda, J. Heeg, H. Huth, A.A. Minakov, M.L. Di Lorenzo, C. Schick, B. Wunderlich, Melting and Crystallization of Poly(butylene Terephthalate) by Temperature-modulated and Superfast Calorimetry, *J. Polymer Sci., Part B: Polymer Phys.*, 44 (2006) 1364-1377.
- [55] R.T. Tol, A.A. Minakov, S.A. Adamovsky, V.B.F. Mathot, C. Schick, Metastability of Polymer Crystallites Formed at Low Temperature Studied by Ultra Fast Calorimetry* Polyamide 6 Confined in Sub-micrometer Droplets vs Bulk PA6, *Polymer*, 47 (2006) 2172-2178.
- [56] A. Minakov, A. Wurm, C. Schick, Superheating in Linear Polymers Studied by Ultrafast Nanocalorimetry, *Eur. Phys. J. E Soft Matter*, 23 (2007) 43-53.
- [57] A.A. Minakov, A.W. van Herwaarden, W. Wien, A. Wurm, C. Schick, Advanced Nonadiabatic Ultrafast Nanocalorimetry and Superheating Phenomenon in Linear Polymers, *Thermochim. Acta*, 461 (2007) 96-106.
- [58] A.W. van Herwaarden, Overview of Calorimeter Chips for Various Applications, *Thermochim. Acta*, 432 (2005) 192-201.
- [59] H. Janeschitz-Kriegl, *Crystallization Modalities in Polymer Melt Processing, Fundamental Aspects of Structure Formation*, Springer, Wien, New York, 2010.
- [60] E.S. Watson, M.O. O'Neill, J. Justin, N. Brenner, A Differential Scanning Calorimeter for Quantitative Differential Thermal Analysis, *Anal. Chem.*, 36 (1964) 1233-1238.
- [61] A. Sepúlveda, A.F. Lopeandía, R. Domènech-Ferrer, G. Garcia, F. Pi, J. Rodríguez-Viejo, F.J. Muñoz, Microchip Power Compensated Calorimetry Applied to Metal Hydride Characterization, *International Journal of Hydrogen Energy*, 33 (2008) 2729-2737.
- [62] W. Chen, D. Zhou, G. Xue, C. Schick, Chip Calorimetry for Fast Cooling and Thin Films: a Review, *Front. Chem. China*, 4 (2009) 229-248.
- [63] S. Adamovsky, C. Schick, Ultra-fast Isothermal Calorimetry Using Thin Film Sensors, *Thermochim. Acta*, 415 (2004) 1-7.

- [64] M.Y. Efremov, E.A. Olson, M. Zhang, S.L. Lai, F. Schiettekatte, Z.S. Zhang, L.H. Allen, Thin-film Differential Scanning Nanocalorimetry: Heat Capacity Analysis, *Thermochim. Acta*, 412 (2004) 13-23.
- [65] A.F. Lopeandia, J. Valenzuela, J. Rodríguez-Viejo, Power Compensated Thin Film Calorimetry at Fast Heating Rates, *Sensors and Actuators A: Physical*, 143 (2008) 256-264.
- [66] M. Merzlyakov, Method of Rapid (100,000 K/s) Controlled Cooling and Heating of Thin Samples, *Thermochim. Acta*, 442 (2006) 52-60.
- [67] E. Zhuravlev, C. Schick, Fast Scanning Power Compensated Differential Scanning Nano-Calorimeter: 1. The Device, *Thermochim. Acta*, 505 (2010) 1-13.
- [68] E. Zhuravlev, C. Schick, Fast Scanning Power Compensated Differential Scanning Nano-Calorimeter: 2. Heat Capacity Analysis, *Thermochim. Acta*, 505 (2010) 14-21.
- [69] M.J. O'Neill, The analysis of a Temperature-controlled Scanning Calorimeter, *Anal. Chem.*, 36 (1964) 1238-1245.
- [70] M.J. O'Neill, Measurement of Specific Heat Functions by Differential Scanning Calorimetry, *Anal. Chem.*, 38 (1966) 1331-1336.
- [71] E.S. Watson, M.J. O'Neill, Differential Microcalorimeter, The Perskin-Elmer Corporation, Norwalk, Conn., 1966,
- [72] E. Zhuravlev, C. Schick, Patent pending, USA, 2009,
- [73] Meilhaus ADC/DAC board, 2009.
<http://www.meilhaus.de/fileadmin/upload/download/products/manuals/ME-4600%202.0E.pdf>
- [74] A.A. Minakov, S.A. Adamovsky, C. Schick, Advanced Two-channel AC Calorimeter for Simultaneous Measurements of Complex Heat Capacity and Complex Thermal Conductivity, *Thermochim. Acta*, 403 (2003) 89-103.
- [75] H. Huth, A. Minakov, C. Schick, High Sensitive Differential AC-Chip Calorimeter for Nanogram Samples, *Netsu Sokutei*, 32 (2005) 70-76.
- [76] SRS Small Instrumentation Module, 2009. <http://www.thinksrs.com/products/SIM.htm>
- [77] V.A. Drebuschak, Universality of the emf of Thermocouples, *Thermochim. Acta*, 496 (2009) 50-53.
- [78] Y.L. Gao, E. Zhuravlev, C.D. Zou, B. Yang, Q.J. Zhai, C. Schick, Calorimetric Measurements of Undercooling in Single Micron Sized SnAgCu Particles in a Wide Range of Cooling Rates, *Thermochim. Acta*, 482 (2009) 1-7.

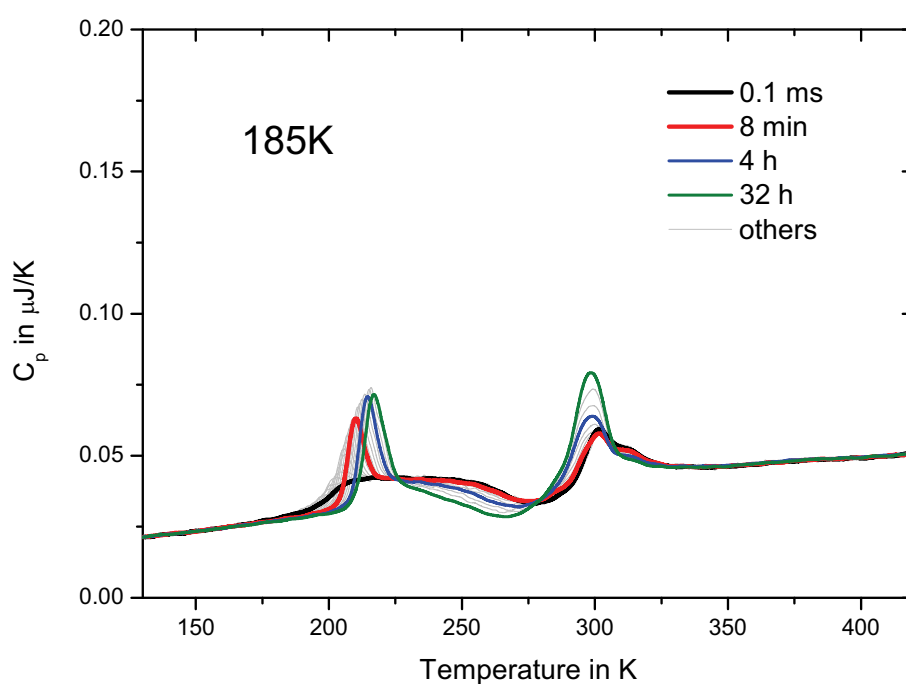
- [79] G.W.H. Hohne, H.K. Cammenga, W. Eysel, E. Gmelin, W. Hemminger, The Temperature Calibration of Scanning Calorimeters, *Thermochim. Acta*, 160 (1990) 1-12.
- [80] S.M. Sarge, W. Hemminger, E. Gmelin, G.W.H. Hohne, H.K. Cammenga, W. Eysel, Metrologically Based Procedures for the Temperature, Heat and Heat Flow Rate Calibration of DSC, *J. Therm. Anal.*, 49 (1997) 1125-1134.
- [81] G. YuLai, Z. ChangDong, Y. Bin, Z. QiJie, Fast Calorimetric Scanning of Micro-sized SnAgCu Single Droplet at a High Cooling Rate, *Sci China Ser E-Tech Sci*, 52 (2009) 1707-1711.
- [82] B. Yang, Y.L. Gao, C.D. Zou, Q.J. Zhai, E. Zhuravlev, C. Schick, Repeated Nucleation in an Undercooled Tin Droplet by Fast Scanning Calorimetry, *Materials Letters*, 63 (2009) 2476-2478.
- [83] S. Neuenfeld, C. Schick, Verifying the Symmetry of Differential Scanning Calorimeters Concerning Heating and Cooling Using Liquid Crystal Secondary Temperature Standards, *Thermochim. Acta*, 446 (2006) 55-65.
- [84] S.M. Sarge, G.W.H. Hohne, H.K. Cammenga, W. Eysel, E. Gmelin, Temperature, Heat and Heat Flow Rate Calibration of Scanning Calorimeters in the Cooling Mode, *Thermochim. Acta*, 361 (2000) 1-20.
- [85] C. Schick, U. Jonsson, T. Vassilev, A. Minakov, J. Schawe, R. Scherrenberg, D. Lőrinczy, Applicability of 8OCB for Temperature Calibration of Temperature Modulated Calorimeters, *Thermochim. Acta*, 347 (2000) 53-61.
- [86] W. Hemminger, G.W.H. Hohne, *Calorimetry - Fundamentals and Practice*, Vch, Weinheim, 1984.
- [87] B. Wunderlich, The ATHAS Database on Heat Capacities of Polymers, <http://athas.prz.edu.pl/Default.aspx?op=db>, *Pure Appl. Chem.*, 67 (1995) 1019-1026.
- [88] B. Wunderlich, Precision Heat Capacity Measurements for the Characterization of Two-phase Polymers, *J. Therm. Anal.*, 30 (1985) 1217-1221.
- [89] E.A. Olson, M.Y. Efremov, M. Zhang, Z.S. Zhang, L.H. Allen, The Design and Operation of a MEMS Differential Scanning Nanocalorimeter for High-speed Heat Capacity Measurements of Ultrathin Films, *J. Microelectromech. Syst.*, 12 (2003) 355-364.
- [90] S. Rastogi, Y. Yao, D.R. Lippits, G.W.H. Höhne, R. Graf, H.W. Spiess, P.J. Lemstra, Segmental Mobility in the Non-crystalline Regions of Semicrystalline Polymers and its Implications on Melting, *Macromolecular Rapid Communications*, 30 (2009) 826-839.

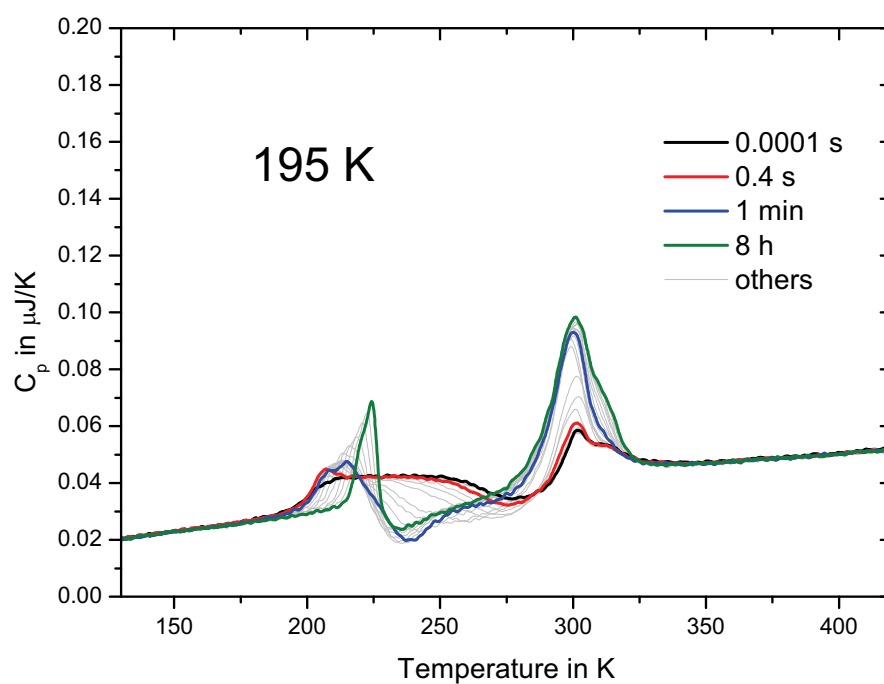
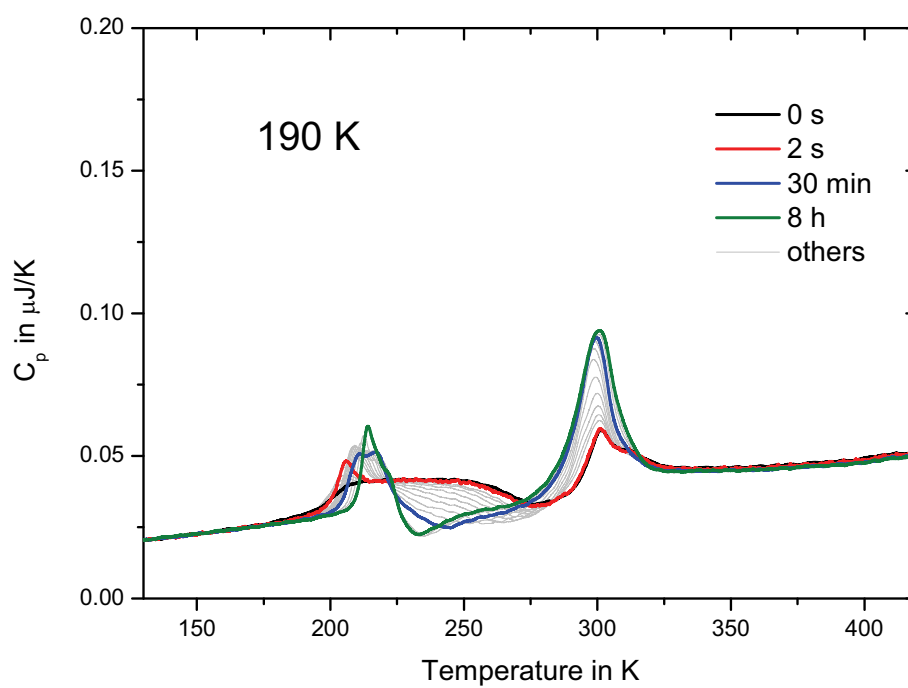
-
- [91] D. Mileva, R. Androsch, E. Zhuravlev, C. Schick, Temperature of Melting of the Mesophase of Isotactic Polypropylene, *Macromolecules*, 42 (2009) 7275–7278.
- [92] D. Mileva, R. Androsch, E. Zhuravlev, C. Schick, Critical Rate of Cooling for Suppression of Crystallization in Random Copolymers of Propylene with Ethylene and 1-butene, *Thermochim. Acta*, 492 (2009) 67-72.
- [93] S. Guns, P. Kayaert, M.J. A., V.H. Jan, V. Mathot, T. Pijpers, E. Zhuravlev, C. Schick, V.d.M. Guy, Characterization of the Copolymer Poly(ethyleneglycol-g-vinylalcohol) as a Potential Carrier in the Formulation of Solid Dispersions, *European Journal of Pharmaceutics and Biopharmaceutics*, 74 (2) (2009) 239-247.
- [94] V.B.F. Mathot, *Calorimetry and Thermal Analysis of Polymers*, Hanser Publishers, München, 1994.
- [95] J.D. Hoffman, J.J. Weeks, Melting Process and the Equilibrium Melting Temperature of Polychlorotrifluoroethylene, *Journal of Research of the National Bureau of Standards - A. Physics and Chemistry*, 66A (1962) 13-28.
- [96] T. Kanaya, Y. Takayama, Y. Ogino, G. Matsuba, K. Nishida, Precursor of Primary Nucleation in Isotactic Polystyrene Induced by Shear Flow, *Lecture Notes in Physics*, 714 (2007) 87-96.
- [97] K. Kaji, K. Nishida, T. Kanaya, G. Matsuba, T. Konishi, M. Imai, Spinodal Crystallization of Polymers: Crystallization from the Unstable Melt, *Adv Polym Sci*, 191 (2005) 187-240.

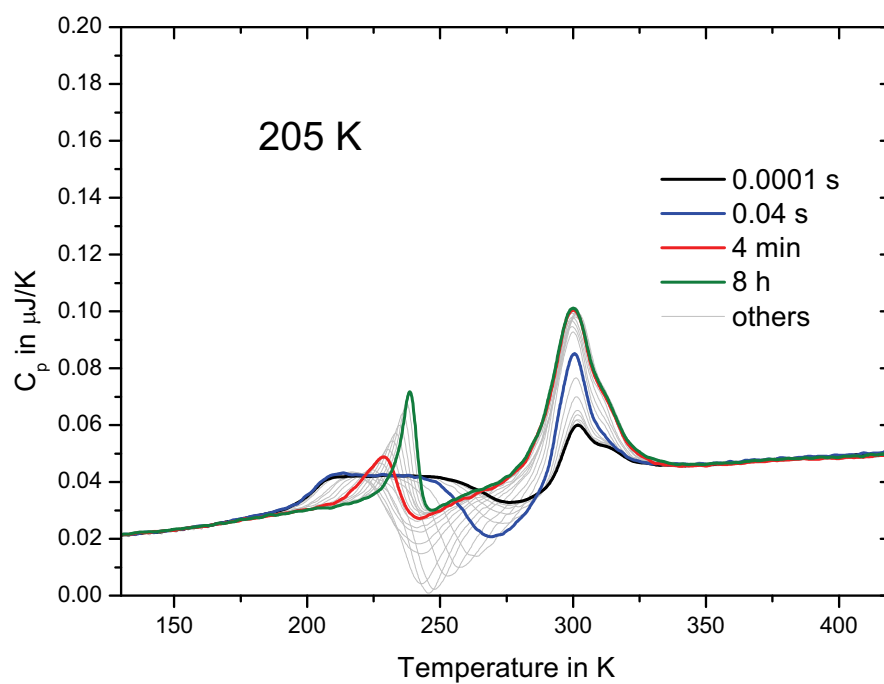
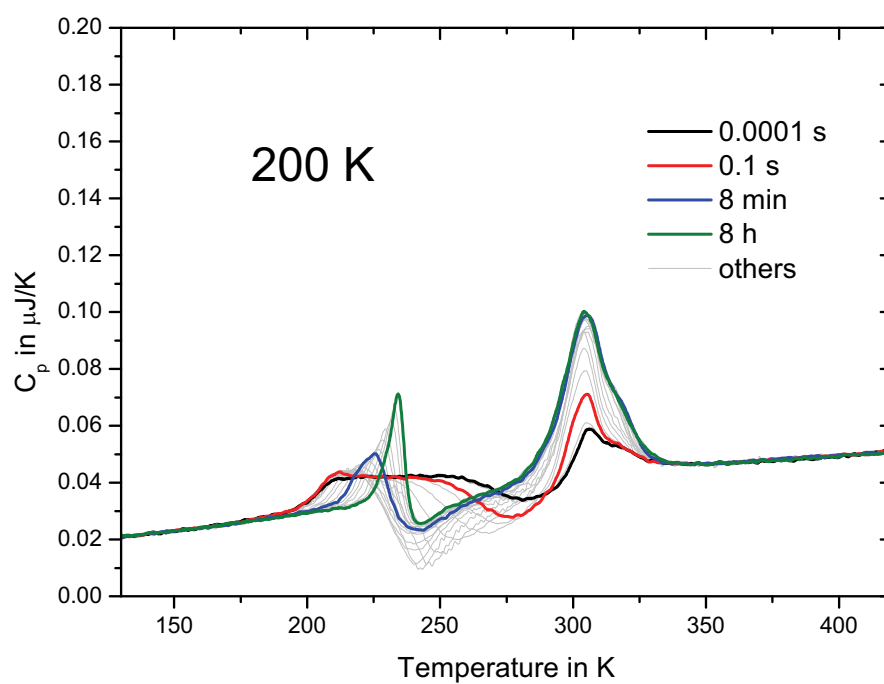
Appendix

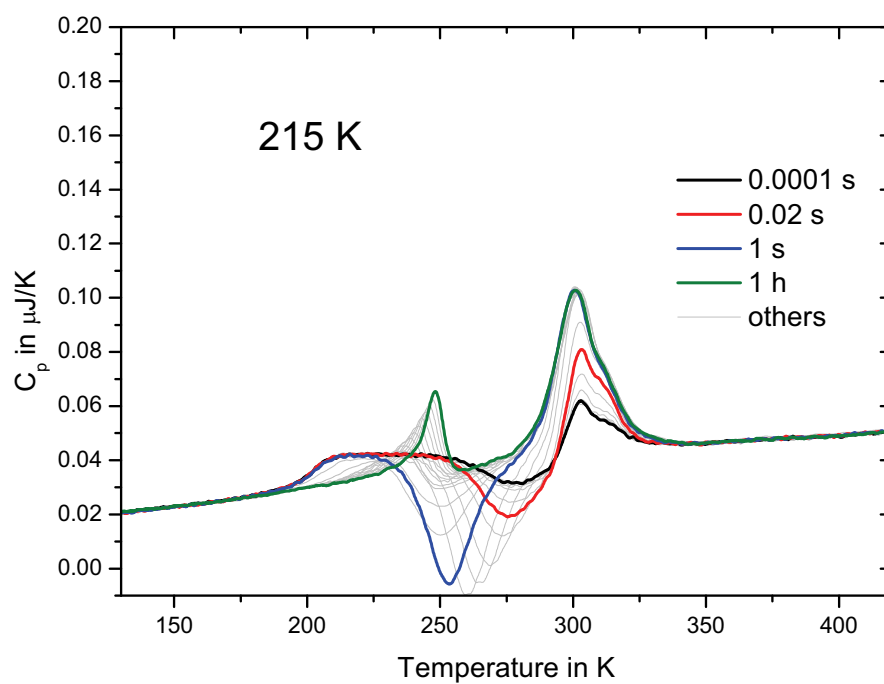
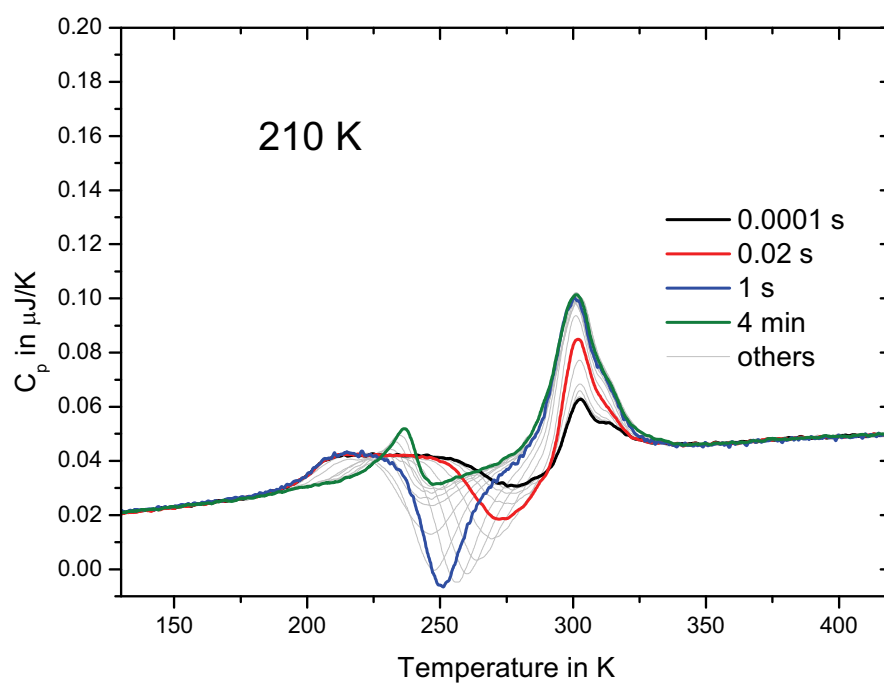
A1. Experimental data for all heating curves after annealing

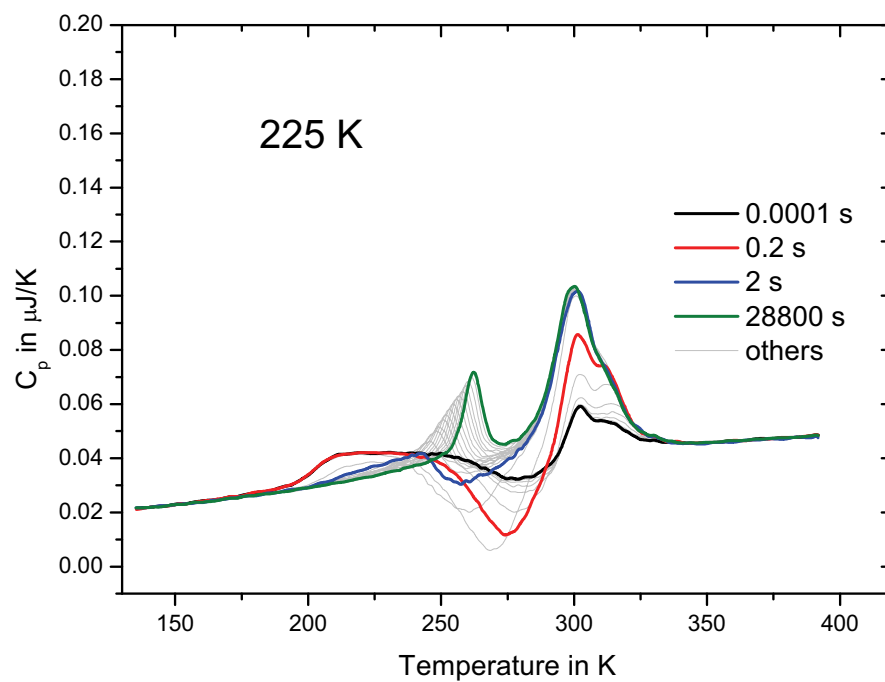
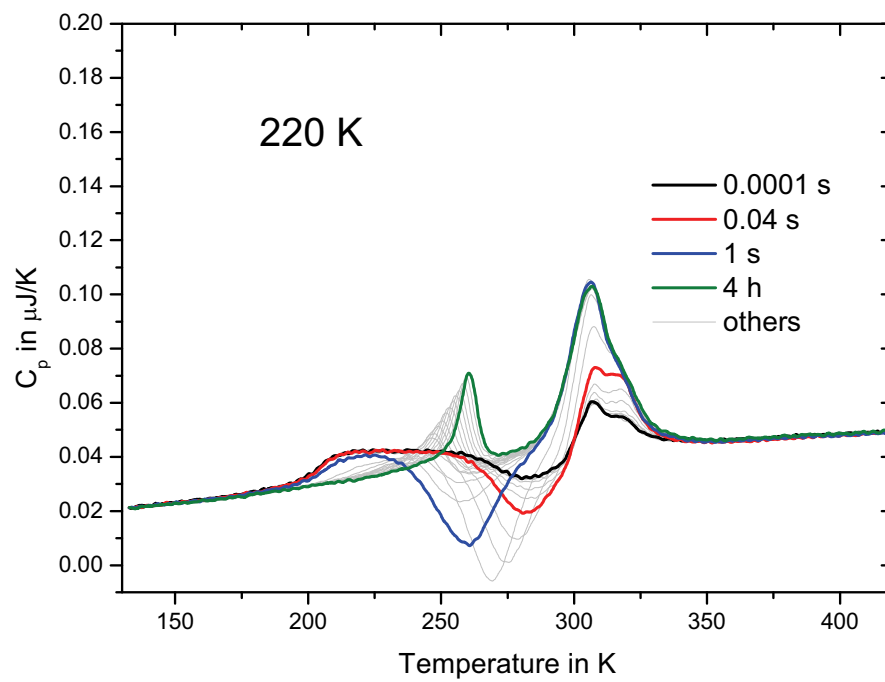
The following are figures of obtained data which were used for determination of cold crystallization and overall excess heat capacity on heating in [chapter 5](#). Each curve is heating of PCL at 1000 K/s after annealing at particular temperature for particular time.

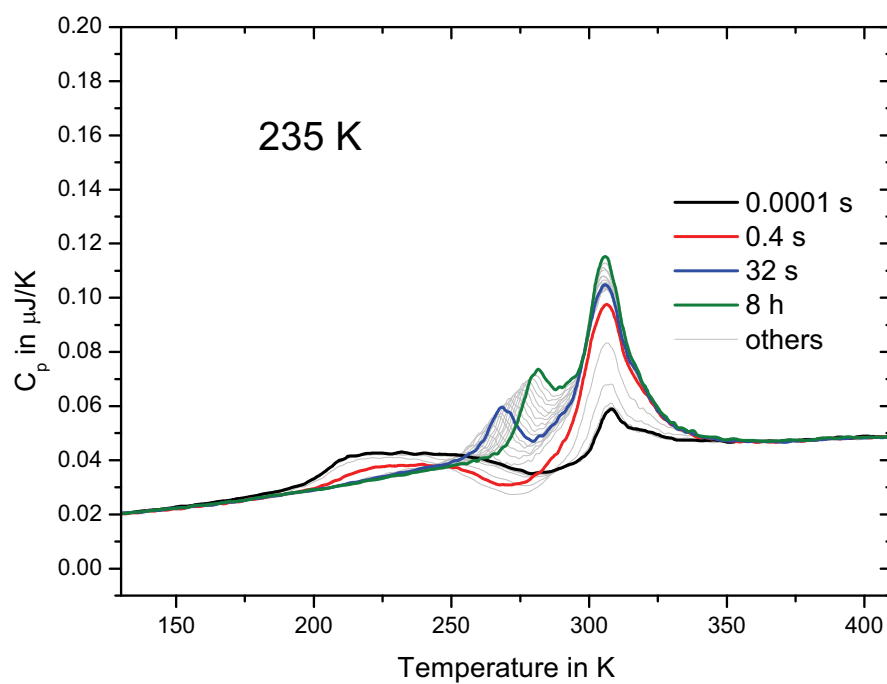
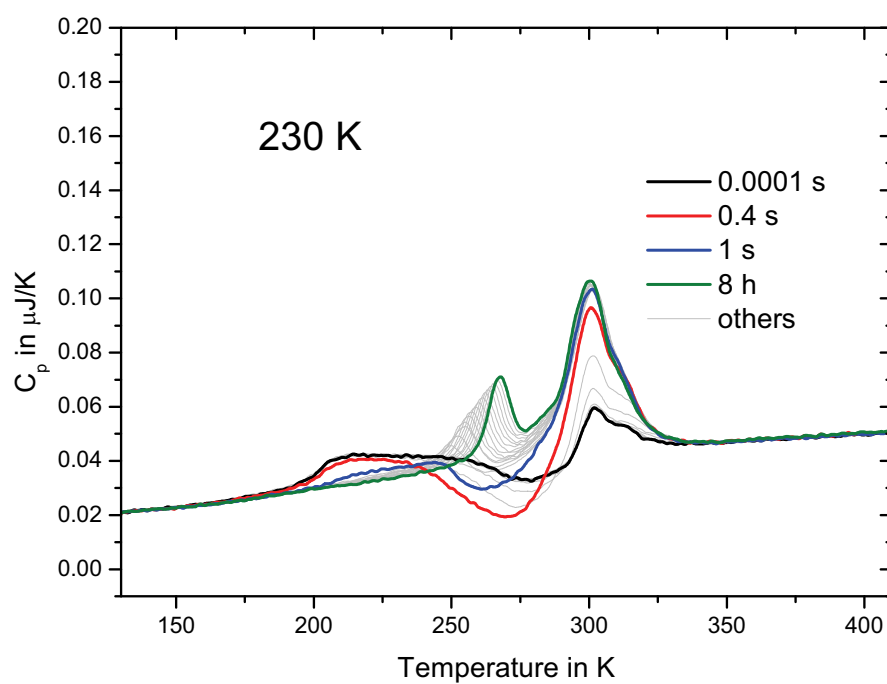


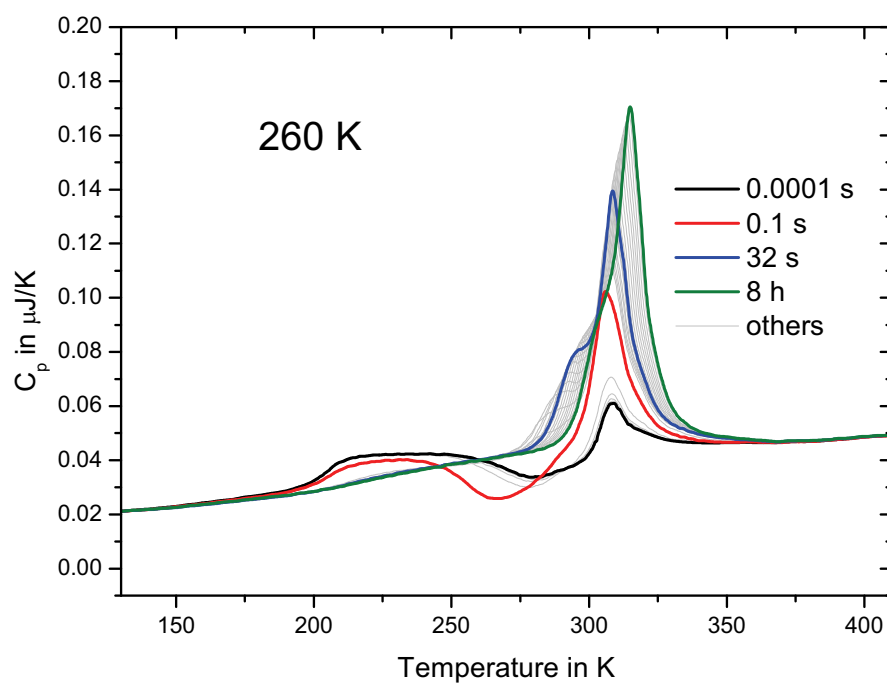
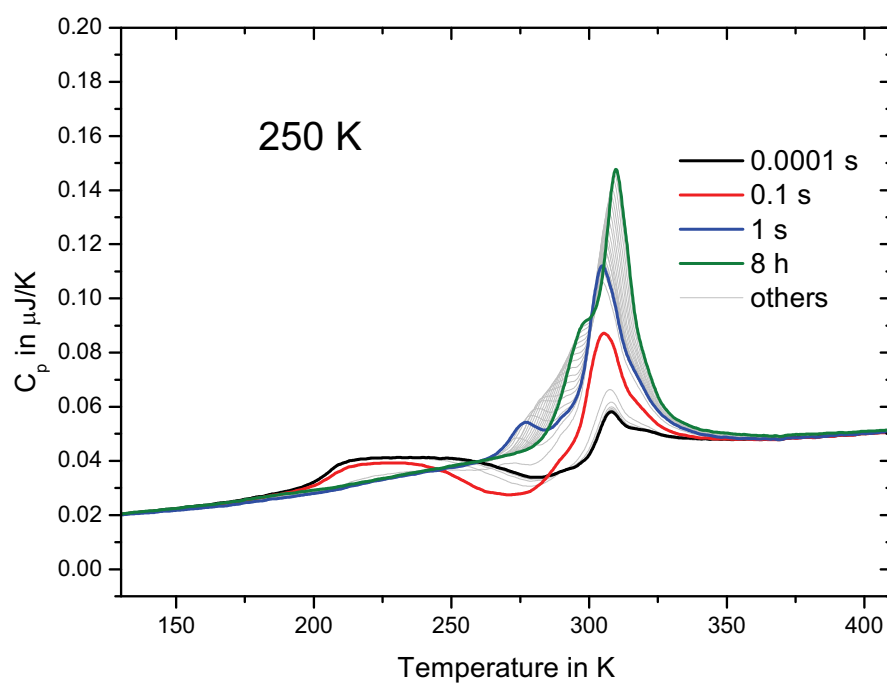


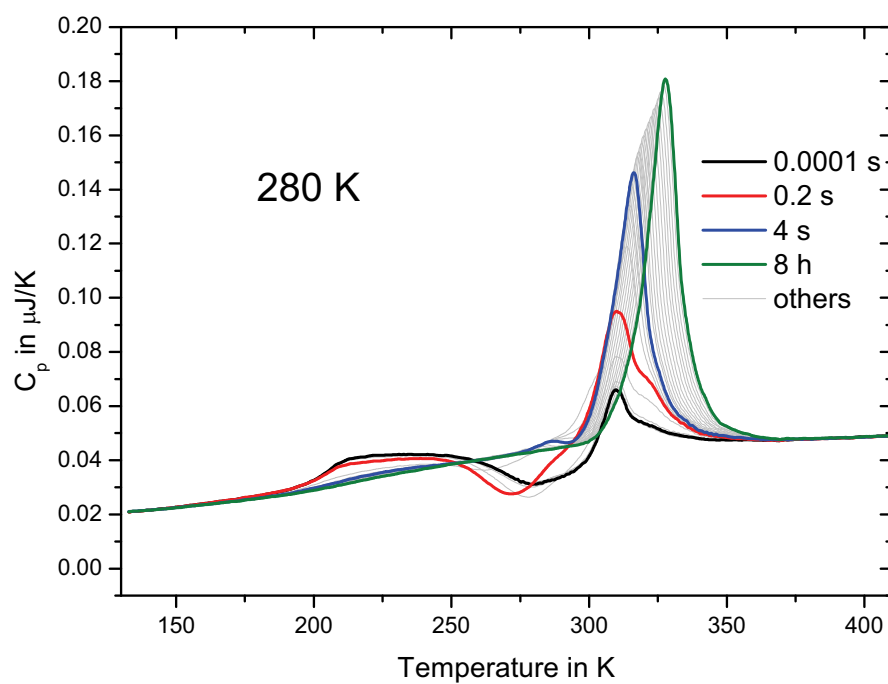
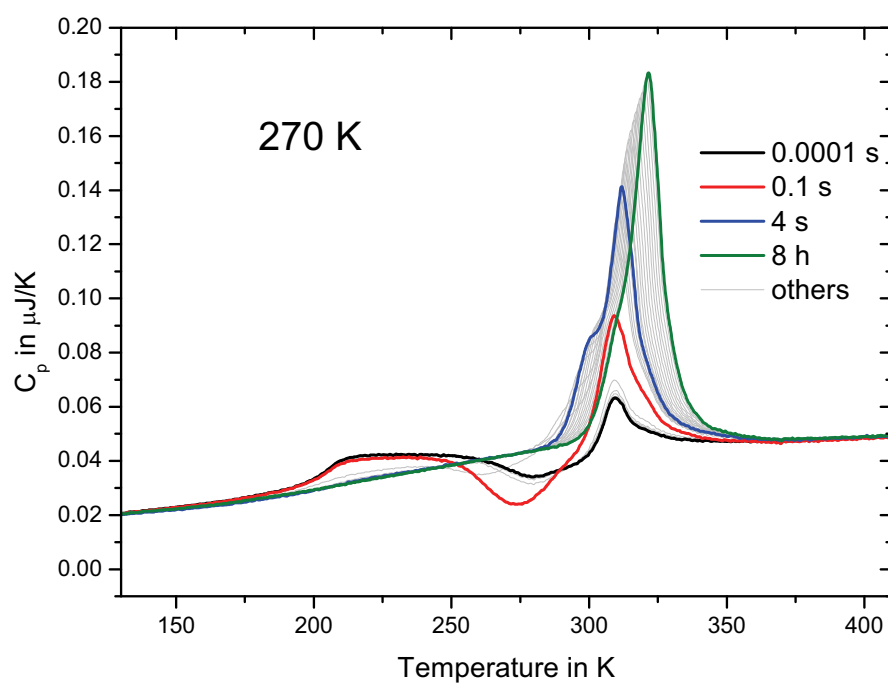


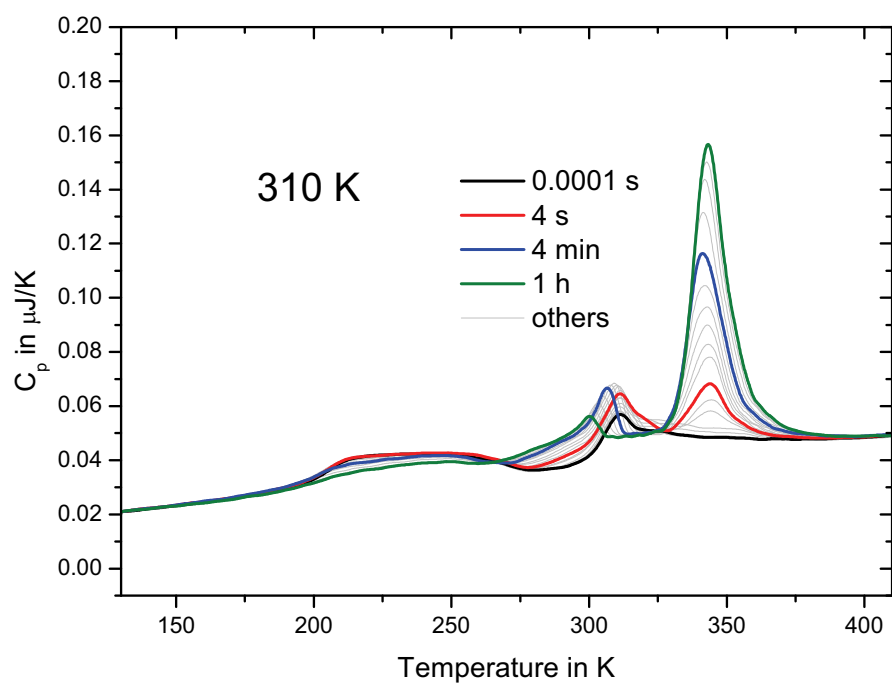
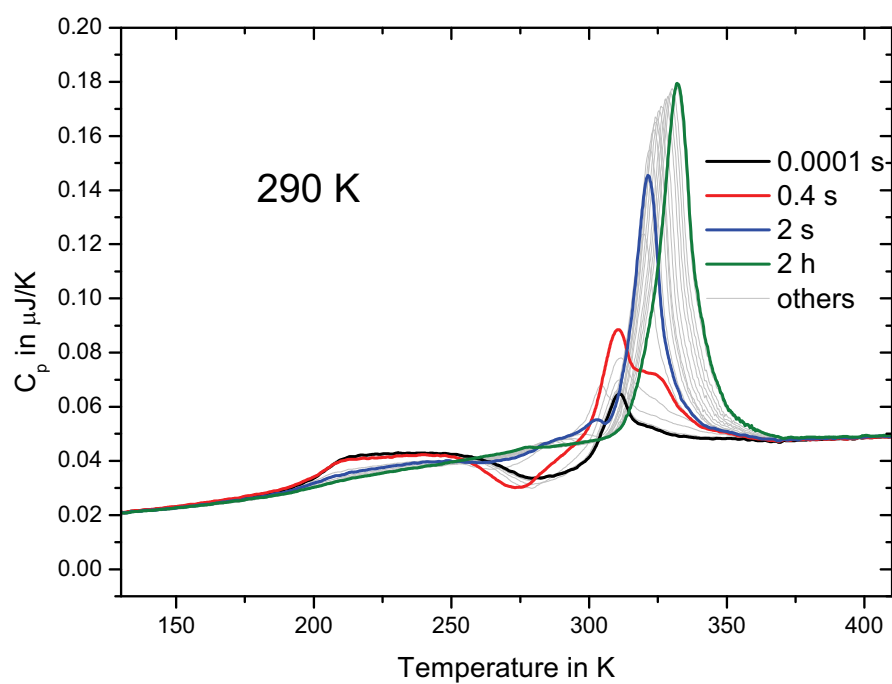


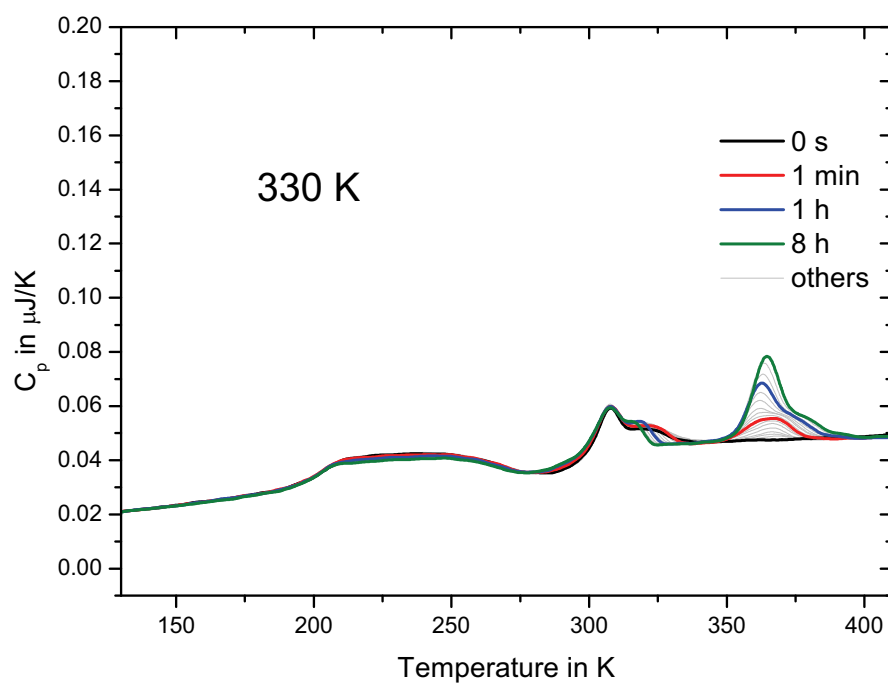
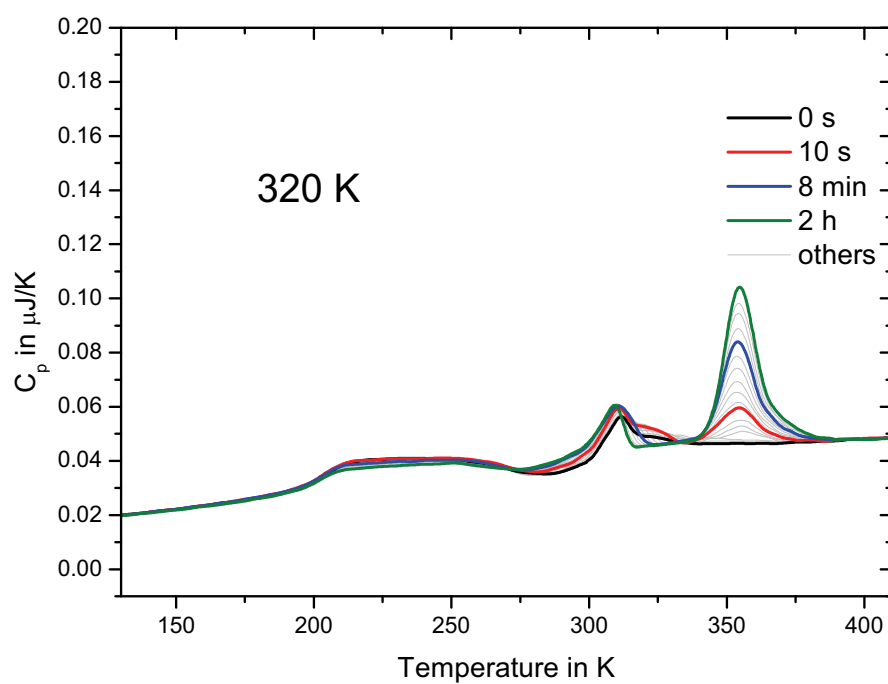


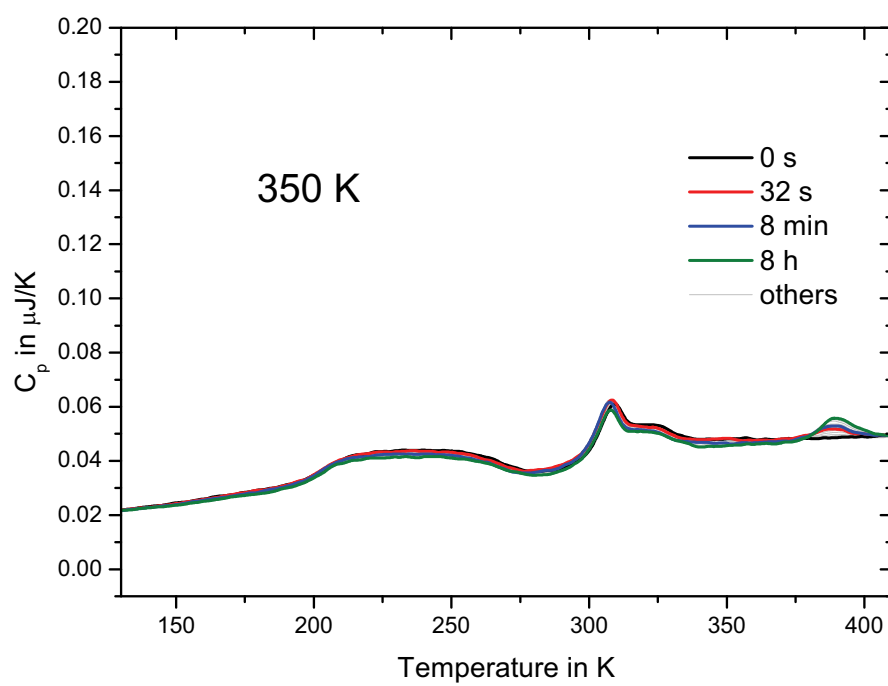












A2. Fast scanning calorimeter software

A2.1. Measurement software

System requirements and main

The software requires Windows XP or higher operating system, a PC with at least 1 GHz processor and 2 GB RAM. LabView 8.6 or higher, professional version, as well as NI VISA drivers for the NI GPIB-USB-HS converter for communication with the SRS modules and the drivers for the Meilhaus board ME 46xx series. Basic knowledge of LabView user interface is also required to start the program and to use the built in controls. When all the drivers and software are installed, the program can be started in order to perform a measurement. It is assumed in this manual that all electronics is assembled according to the schemes represented in Figure 20 and Figure 30 and is working properly.

Starting the program

The main measurement program is a top level program in the LabView library file, e.g. FS_3.llb. To start it double click on the FS_3.llb and then double click on the top level program (FS_3_Measurement.vi). The program will start and in the case of no mistakes in driver installation and peripheral device connections, it will be ready for measurement.

The front panel (Figure 54) of the program consists of controls (buttons, text control, menu rings and list-boxes), indicators ('lamps', graphs, text indicators) and Tab page which is used to group controls and indicators according to their functionality. The difference between controls and indicators is that the value of the indicators the user cannot change directly. Both control and indicator values can be changed by the program. Text controls are often not updating while typing – to apply changes the 'Enter' or Ctrl+'Enter' buttons should be used, or click away with the mouse (don't click while typing in some other control, their values can change unexpectedly and cause a program error). Depending on LabView setup, 'Enter' or Ctrl+'Enter' are used to accept changes or to switch to next line in text control.

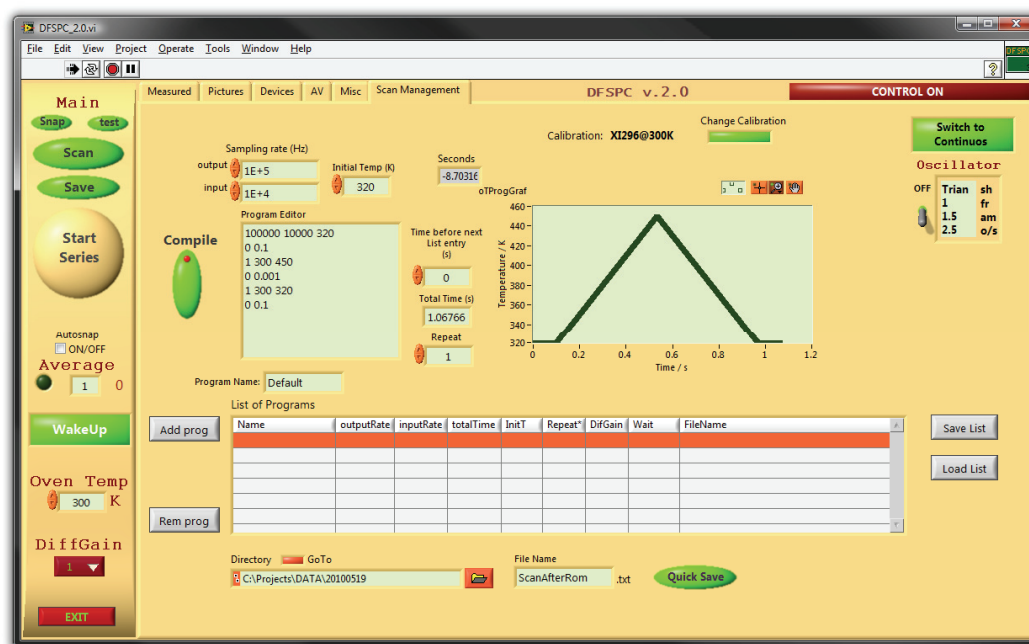


Figure 54. Front panel of the measurement program.

In tab control there are six pages. In ‘Measured’ page one can find measured voltages. ‘Pictures’ displays recalculated temperatures and power values, as well as heating rate. ‘Devices’ page allows controlling of SRS modules parameters. The ‘AV’ and ‘Misc’ pages contain advanced settings for testing and are commonly not needed. In ‘Scan Management’ the parameters of a single measurement and measurement series can be programmed. The most important parameters, which then will be used for all measurements are thermopile calibration, oven temperature and power compensation gain settings. They can be controlled as described below.

After the program is started, the thermopile calibration selection window appears where the user can choose a calibration according to the sensor type and actual oven temperature. It could be changed any time later on in the ‘Scan Management’ page by pressing ‘Change Calibration’ button.

Next the oven temperature should be entered in the corresponding control in Kelvin. After that power compensation gain settings should be chosen as 10 or 5, depending on the noise of the signal, from the drop-down list ‘DiffGain’.

The program can stop working if some errors occur. In this case, after correction of the errors, the ‘Run’ button in common LabView vi toolbar in the front panel of the program should be pressed in order to start the program again. The most common reason for a program error is a memory overflow. This happens due to mistakes during modification of the

temperature program or due to too large number of points in the measurement. In this case it is recommended to correct the temperature program in the corresponding control in the front panel before starting the program again. In case of this mistake appears constantly, quit LabView and start the program from the beginning.

In order to avoid sensor damage due to malfunction of the device, e.g. applying high voltage to the heater, strict safety precautions should be taken.

Sensor safety precautions

The system temperature control loop can go to saturation or produce dangerous voltage spikes in case of disconnection of one of the connections in the sensors. This can cause damage to the sample under investigation and in worst case to sensors. To avoid this during sensor exchange and while not performing a measurement several precautions should be taken. First – in case of emergency, the sensors heaters should be disconnected using corresponding knob on the additional module embedded in the SRS block. Second – if program is working properly, the maximum voltage generated into the system can be limited by the internal limiter of the PID controller and an additional limiter for the sample heater control circuit. Both can be modified from the front panel using the corresponding control, ‘A’ in Figure 55 .

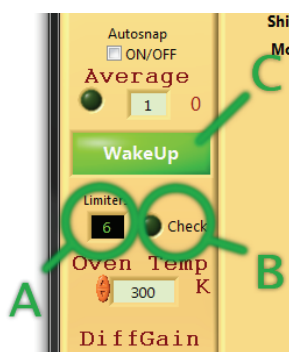


Figure 55. Heater voltage limiters control (‘A’) and sensor test button (‘B’). Standby/Wake up button (‘C’).

When the system is not used, it can be set into ‘Standby’ mode by pressing corresponding button on the front panel (‘C’ in Figure 55). This sets the limiters maximum voltage to 1 V, which is not dangerous for the sensors.

Before making a first test with newly connected sensors, or after some changes in the connection of the system, the presence of the sensors and their connection can be probed using the ‘Check’ button on the front panel (‘B’ in Figure 55). In this case, 0.5 V will be

introduced in the system without ‘opening’ the limiters and the heater resistivity and thermopile voltage will be measured. The reading, which depends on the sensor type, should be similar for sample and reference sensor and 500 – 1500 kOhm for heater resistances and more than 0.1 mV for thermopile signal. If the sensor connection is correct, the first trial measurement can be performed. To compensate possible asymmetry of the sensors it is useful to perform first scan to some low temperatures, 20-50 K above oven temperature, using a small limiter setting (2 V). Only if everything is working properly, the limiters can be set to higher values, the system can be switched to normal operating mode by pressing ‘Wake up’ button and the measurement can be performed.

Avoid touching connecting wires and movement of the system while in working mode. When pressing ‘Scan’ or ‘Scan series’ button the system first goes to working mode and then starts the measurement. After all programs in the temperature program list are finalized the system automatically goes to standby mode by switching limiters to low voltage (1 V).

The system can be tested without opening the sample side limiter. This could help before making a final scan for samples which can be scanned only once. To do so, the ‘test’ button shown later in Figure 58 should be pressed.

Configuration of temperature scans and series of scans

All settings for the current experimental temperature program can be done from ‘Program Editor’ text control (Figure 56).

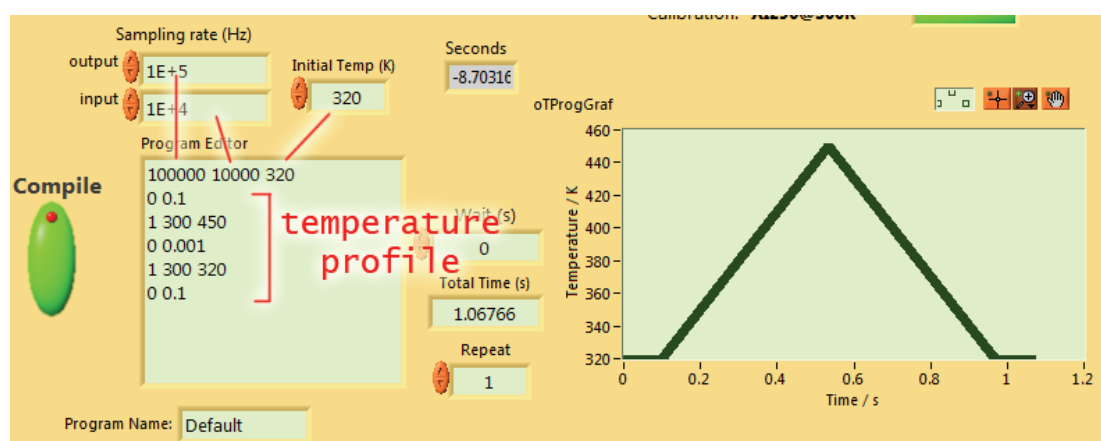


Figure 56. Temperature profile controls and indicators.

The control text consists of one header line and temperature profile lines. The new line is created by pressing Ctrl + ‘Enter’ (‘Enter’ depending on LabView setup) and can be scrolled using the arrow keys. The header line consists of DAC and ADC sampling rate in

samples per second and the starting temperature of the experiment. Be aware that sampling rate is for all channels.

Depending on the length of the experiment the sampling rate should be chosen such that not more than 100,000 points per experiment are generated, otherwise a memory overflow can occur. If high sampling rate is required for long-lasting experiments, it is better to find a way to separate the experiment in several parts, e.g. first heating, second heating and so on. The maximum sampling rate both for input and output is 500,000 samples per second.

After modification of the 'Program Editor' text it should be accepted by pressing 'Enter' (Ctrl + 'Enter') or clicking away with the mouse. After short delay the program will be evaluated. The resulting temperature profile and its parameters could be seen in the other indicators in the 'Scan Management' page.

Before performing a scan the hardware should be prepared for voltage generation and signal acquisition. This could be done by pressing the 'Compile' button (Figure 56). Compilation takes some time, depending on the amount of memory that should be reserved for data acquisition and generation. Compilation time should be taken into account while programming series of measurements.

The software allows performing several measurements in serial with a conditional pause in between. All available programs are shown in the 'List of Programs' list-box (Figure 57). The whole list can be saved and loaded. The saved list file can be edited as plain text.

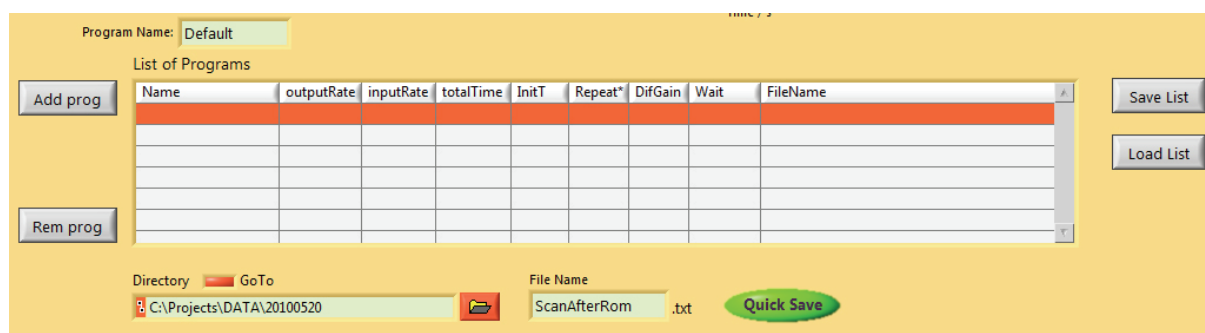


Figure 57. List of measurement programs and corresponding controls.

Before starting a program list the data file output directory should be selected and names checked for consistence (they will be overwritten without confirmation after starting the series of measurements). The waiting time before starting the corresponding program is shown in 'Wait' column and can be modified in the 'Wait' control (Figure 56).

Starting a temperature scan program and acquisition of data

To start the temperature scan program or program list the corresponding button should be pressed in the 'Main' panel (Figure 58). 'Scan' starts a single currently active scan and 'Start Series' starts a series of scans from the beginning of the list.

After the button is pressed the software set the limiters to working voltage, compiles the temperature program (if not yet compiled) and performs the measurement. All measured and some of the recalculated curves can be seen from pages 'Measured' and 'Pictures' in the tab control, Figure 54.



Figure 58. Starting the temperature scan program.

After finalizing a series of measurements the software will automatically switch into 'Standby' mode. The collected series of files can be found in the location designated in the 'Directory' control (Figure 57). The same measurement can be repeated several times and averaged using the 'Average' button and the numeric control shown in Figure 58. It can be adjusted for each temperature scan program in the list.

After each single measurement the data can be exported into the evaluation program or saved to disk by pressing the 'Snap' or 'Save' button, correspondingly.

The data are saved in a text file consisting of columns with names corresponding to the signals or recalculated values and time. They can be exported in any data evaluation software, or can be sent to the software described below.

A2.2. Data evaluation

Loading and saving data

Data evaluation software (DFSCViewer.vi) allows heat capacity determination and basic treatment of data collected by the measurement software described above. It can be started as the measurement software from the DFSCViewer.llb library.

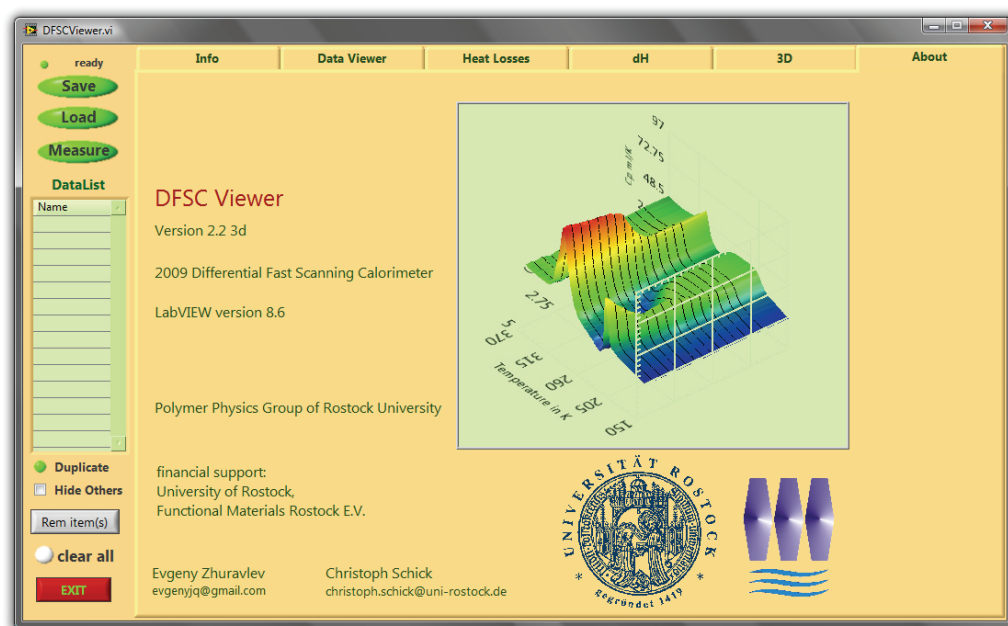


Figure 59. Data evaluation software front panel.

The front panel (Figure 59) of the software is similar to the measurement program and consists of main controls on the left and tab pages in the center. The main controls are used to load, save, select from loaded list, duplicate selected, delete, and hide not selected data and to switch to the measurement software.

The 'Save' button is used to save data, selected in 'DataList' with location prompt. The 'Load' button open a normal windows file selection dialog, where the user can chose one or several files to load.

The 'Load' and 'Save' buttons have extended functionality by means of combination of auxiliary keys. Pressing Ctrl + 'Load' allows apply smoothing filters and interpolation to curves which will be loaded. This could be especially useful for loading large number of big files each of which can be smoothed with known parameters. Smoothing is done by averaging

of the selected curves before interpolation. After filling in parameters shown in Figure 60 the user can select files from the usual dialog that will appear after pressing the ‘Next’ button.

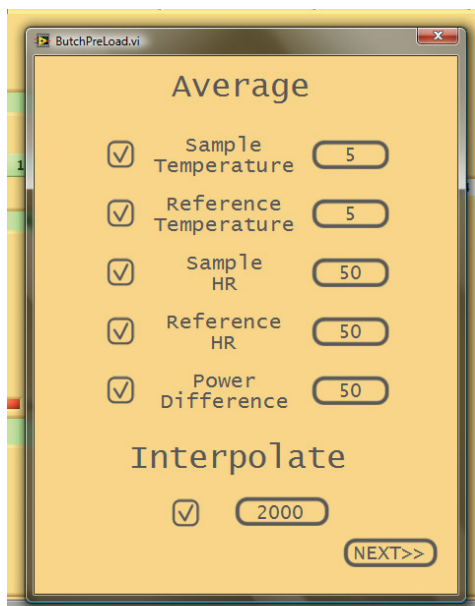


Figure 60. Ctrl + ‘Load’ menu for loading interpolated and smoothed curves from the files.

The combination Shift + ‘Load’ allows a partial data import. As shown in Figure 61, ‘Start’ and ‘End’ cursors are used to select part of the measured curve which will be loaded. The ‘Next’ button will load the next file selected from the previous ‘Load files’ dialog.

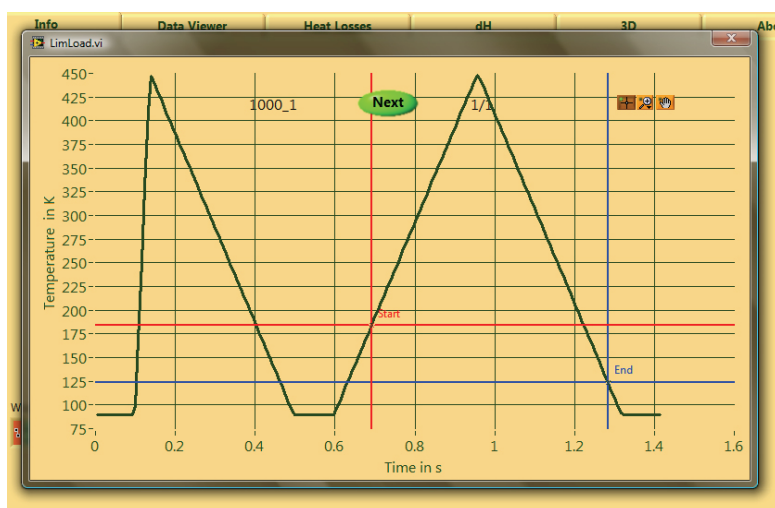


Figure 61. Shift + ‘Load’ allows partial data input for each curve selected.

Combination Shift + ‘Save’ saves all files, selected in ‘DataList’ under their names in the location ‘Working folder’ (Figure 62) in ‘Info’ page of tab control.

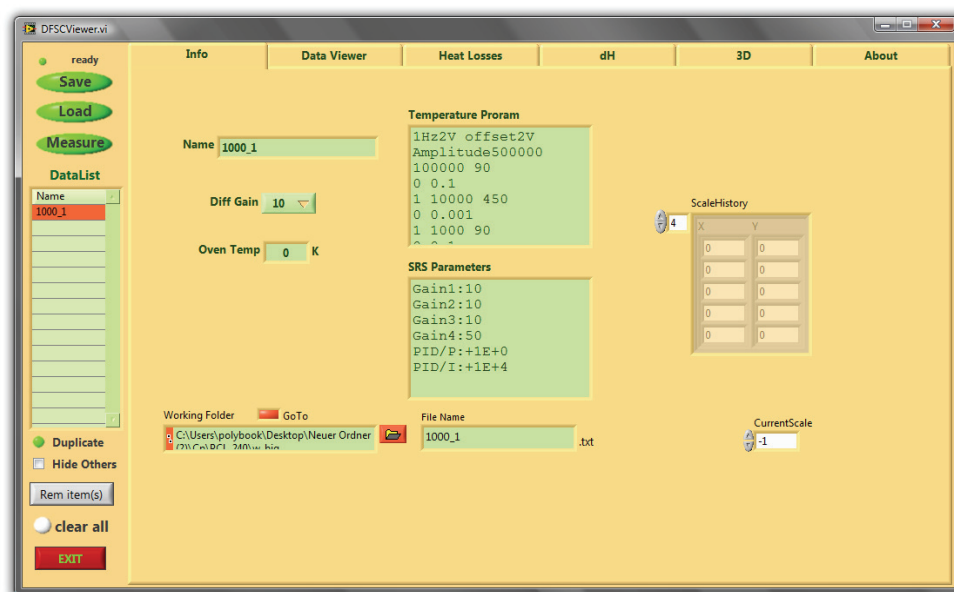


Figure 62. File information page of the software.

The measurement conditions of one file selected from 'DataList' can be seen from the 'Info' page in tab control.

Basic data treatments

The main page in the software is the 'Data Viewer' shown in Figure 63. It consists of the graph, X axes selector ('A' in Figure 63), Y axes selector ('B' in Figure 63), scaling tools ('C' in Figure 63) and basic data treatment tools ('D' in Figure 63).

All modifications with data are done in the current memory of the program, they can not be undone or auto-saved. Always save intermediate steps of the work using the 'Save' and Shift + 'Save' buttons. Before performing possible dangerous operations with the curves it is recommended to duplicate the selected data by pressing the 'Duplicate' button in the left panel below the 'DataList'.

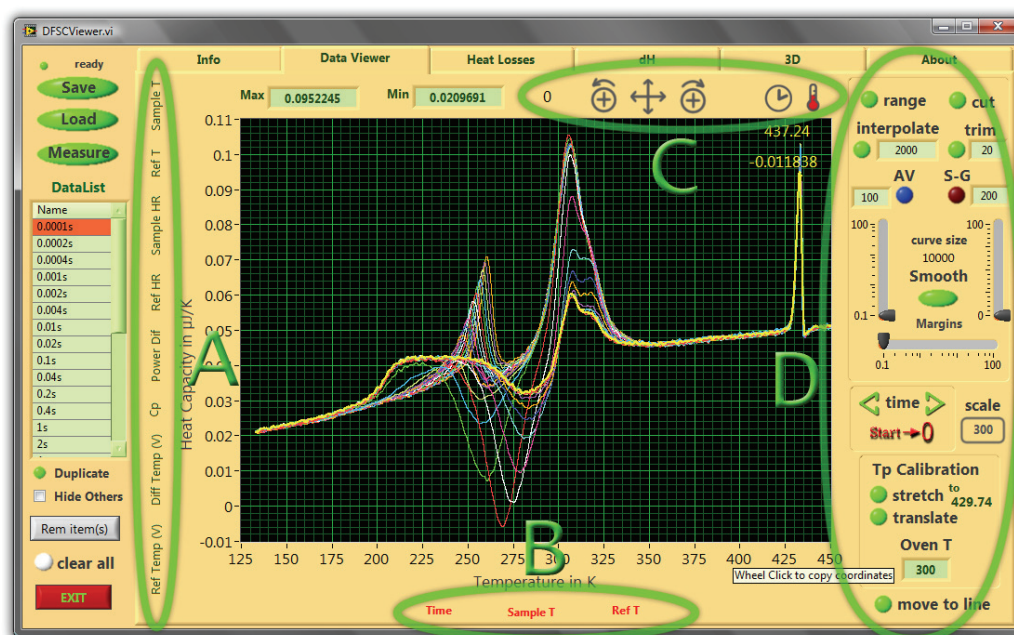


Figure 63. The 'Data Viewer' page of the tab control and its controls: Y axis selector ('A'), X axis selector ('B'), scaling tools ('C') and basic data treatment tools ('D').

The graph in the main page can show either selected data from the 'DataList' or all data as thin and the selected as thick line, depending on the 'Hide Others' checkbox value. The coordinates are chosen by clicking the corresponding name in the axes selector shown in Figure 63A-B.

The mouse pointer can be used in 'Zoom' and 'Cursor' mode – to switch between them click right mouse button in the graph. Current coordinates of the pointer are traced and seen in the top right corner of the graph, they could be copied into the clipboard by pressing the middle button (mouse wheel).

Figure 63C shows the tools, which allow quick switching between time and temperature for X scale ('C' in Figure 63) and rescaling the graph to see all data.

The tools in the right part of the page ('D' in Figure 63) allow making basic treatments of the curves and correction of time and temperature axes. To cut the curve select margins using the cursors, which appear after pressing the 'range' button. To move cursors use the mouse in 'Cursor' mode. What is placed between 'start' and 'end' cursor will stay in the graph after cutting. Smoothing ('D' in Figure 63) can be applied to the whole curve or to a selected part of it. After all treatments are done with the curve it is useful, from memory consumption point of view, to interpolate it with a smaller number of points. Instead of

normally collected 20,000 points for one heating or cooling curve 2000 points are usually enough. Note that after interpolation the smoothing is not efficient any more. Be aware that interpolation can also cause smearing of the curve.

Sometimes big samples with bad thermal contact can cause deviation of temperature inside the sample from the measured value. In this case a reference metal particle can be placed on the sample to probe its temperature independently by the melting peak. The correction of temperature scale for this peak can be done using the corresponding tools shown in section 'D' of Figure 63.

All other buttons are still in test mode and therefore will not be discussed here.

Heat losses curve determination and heat capacity recalculation

To calculate heat capacity as was described in [chapter 4](#) above the heat losses curve should be subtracted from the power difference and further divided by scanning rate. Determination of the heat losses curve can be performed from a symmetric heating-cooling scan on the page 'Heat Losses' of the software (Figure 64).

When the data are transferred from the measuring program or does not have a heat capacity column inside the file, heat capacity is replaced by power difference values. For determination of sample heat capacity the power difference should be divided by temperature scanning rate. The corresponding value of scanning rate is selected in the 'HR' tools in Figure 64.

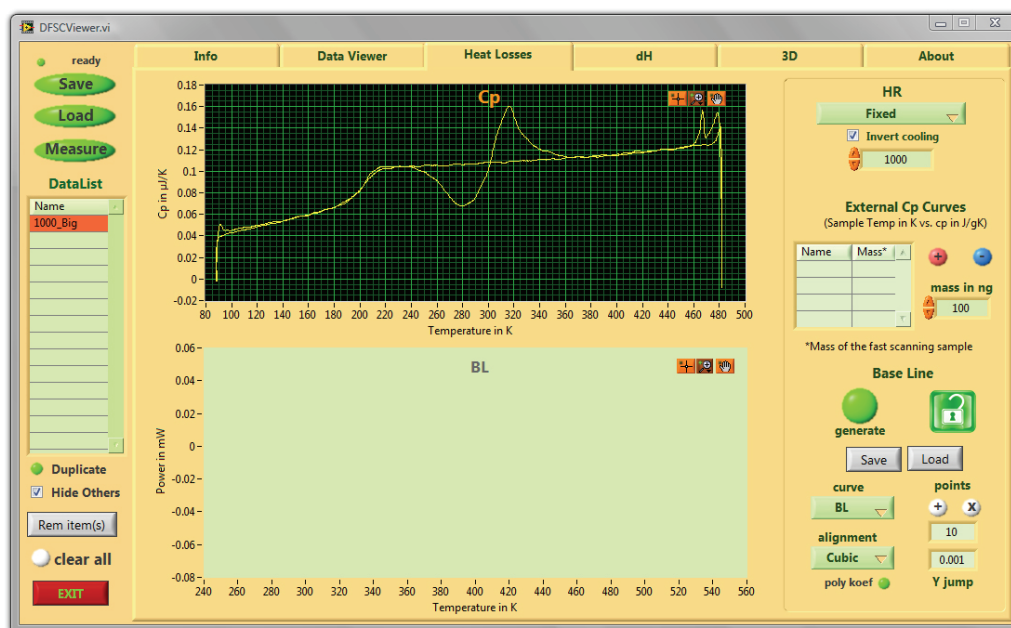


Figure 64. Heat losses subtraction page.

For determination of the heat losses curve a heating-cooling scan with the same heating and cooling rate should be selected. After the scan is selected, press the ‘Generate’ button and in the appearing window (Figure 65) select cooling and heating using cursors.

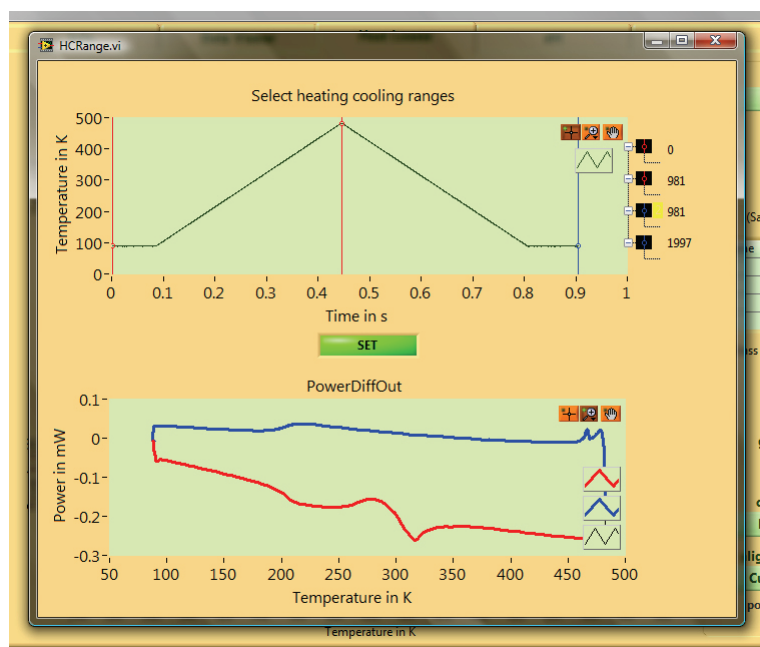


Figure 65. Selection of cooling and heating scan at the same rate for generating the heat losses function.

The selected cooling and heating will be used to generate guide-lines for determination of the symmetry line which will finally be the heat losses curve. The guide-lines and the symmetry line just after generating them are shown in Figure 66. They can be influenced by effects in the sample due to phase transitions and therefore should be corrected.

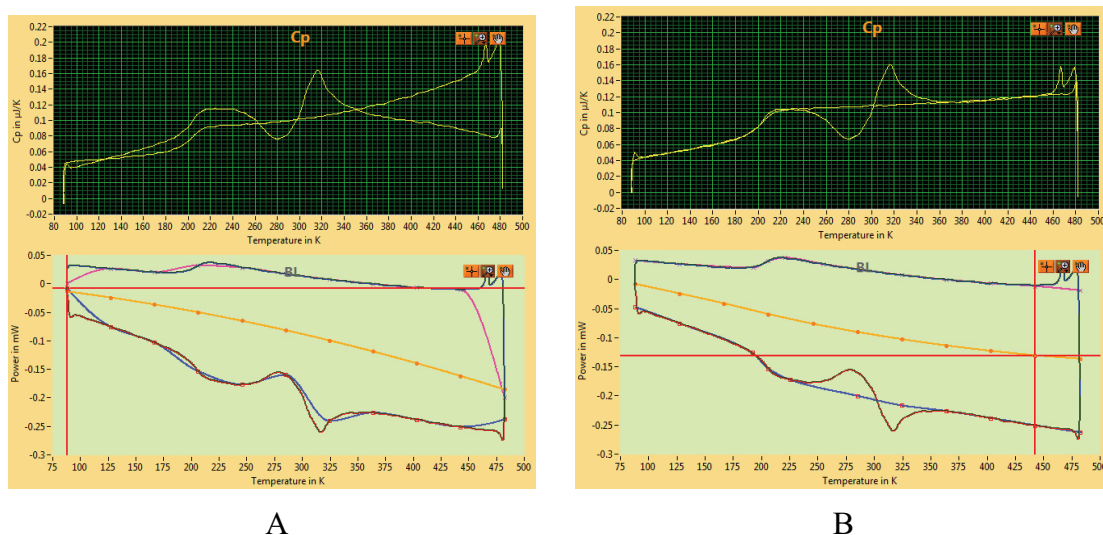


Figure 66. Generated heat losses function before (A) and after corrections (B).

For correction of the guide-lines and the heat losses curve the moving points are used. The number of moving points by default is 10, but can be modified before generating of the guide-lines (Figure 64 'points').

For correct determination of the symmetry line the heating and cooling guidelines should be corrected to coincide with the measured heating or cooling curve without phase transition peaks. For correction select the corresponding curve by the 'curve' selector (Figure 64). The curve can be moved by moving the points. The active point is designated by the red cursor (Figure 66). To switch between points use Ctrl + 'Keyboard arrows'. Just pressing keyboard arrows will move current active point, reconstruct the active curve and recalculate the symmetry line. The distance of movement of the point for a single arrow key press is determined by the values in the 'points' control (Figure 64). To make long jumps (10 times normal jump) use Shift + 'Keyboard arrow'. To avoid artificial peaks in the heat losses curve the polynomial alignment can be used from the 'alignment' control (Figure 64). The final result for the correct heat losses curve construction is shown in Figure 66B.

The main ideas of heat losses function determination can be found in [corresponding chapter](#). After determination of the heat losses curve for the particular sample it could be saved (Figure 64 ‘Save’ in ‘BL’ section) and applied for all the measurements from the same sample for the same heating rate (Figure 64 ‘HR’ section). To apply the heat loss function to other data loaded, chose the ‘Heat Losses’ page, set ‘Y jump’ to 0 and go through the ‘Data List’ using the up and down keyboard arrow. Do not forget to change heating rate in ‘HR’, if it is fixed.

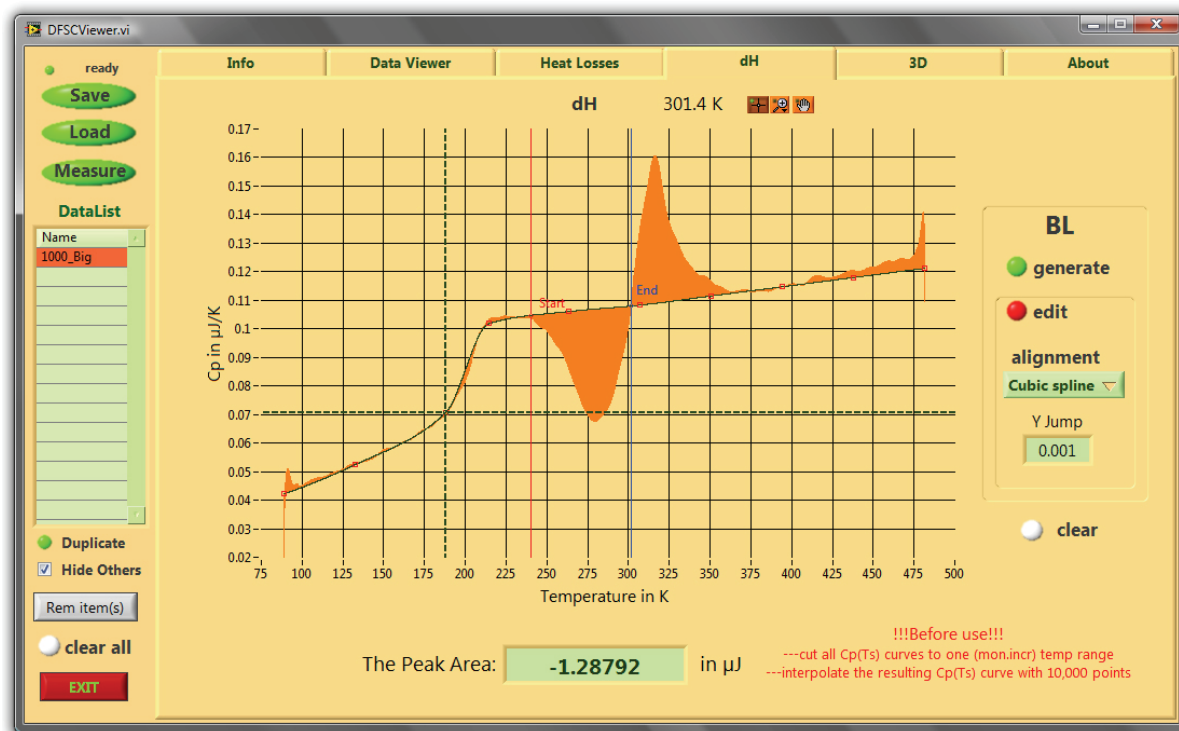


Figure 67. Excess enthalpy change (peak area) calculation.

The software allows also calculation of the excess enthalpy change (peak area) calculation (Figure 67). For that the heat capacity curve should be interpolated to 10,000 points and the corresponding data should be selected while ‘dH’ page is active. After that the integration baseline should be constructed using ‘BL’ buttons and other controls. Depending on ‘alignment’ it could be a line (poly-1) or smooth curve (cubic spline). The editing of the baseline is made in a similar way as for heat losses curves when the ‘edit’ button is pressed. In Figure 67 the baseline is the curve at fast cooling of the molten sample without crystallization. The integration range is modified using the red and blue cursors. The resulting enthalpy change is shown in the bottom of the page in μJ .

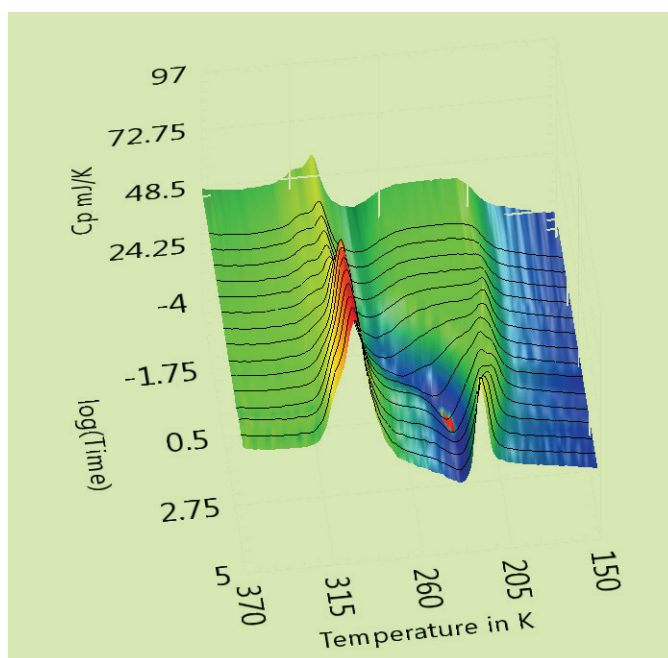


Figure 68. Heat capacity (Z axes) on heating (X axes) of PCL sample discussed above after annealing for different times (Y axes) at 210 K.

The data evaluation software allows basic mathematical data curve treatments, graphic heat losses curve estimation and therefore heat capacity determination and heat capacity vs. temperature peak integration (excess enthalpy change determination). Figure 68 shows three dimensional picture of heat capacity measurement on heating depending on previously made annealing ([see previous chapters](#)). It was used for visual observation of the influence of isothermal crystal nucleation and growth on the behavior of the material on successive heating.

Liste der Veröffentlichung

Publikationen

1. Zhuravlev, E., Schick, C., "Fast Scanning Power Compensated Differential Scanning Nano-Calorimeter: 1. The Device" *Thermochimica Acta* 505 (2010), 1 - 13
2. Zhuravlev, E., Schick, C., "Fast Scanning Power Compensated Differential Scanning Nano-Calorimeter: 2. Heat Capacity Analysis" *Thermochimica Acta* 505 (2010), 14 - 21
3. Zhuravlev, E., Schick, C., "Power Compensated Differential Scanning Calorimeter for Studying of Solidification of Metals and Polymers on Millisecond Time Scale" *Netsu Sokutei*, vol.37, No.1 (2010), 17-25
4. Guns, S., Kayaert, P., Martens, J. A., Van Humbeeck, J., Mathot, V., Pijpers, T., Zhuravlev, E., Schick, C., Van den Mooter, G., "Characterization of the copolymer poly(ethyleneglycol-g-vinylalcohol) as a potential carrier in the formulation of solid dispersions" *European Journal of Pharmaceutics and Biopharmaceutics* 74 (2009), 239-247
5. Mileva, D., Androsch, R., Zhuravlev, E., Schick, C. "Temperature of Melting of the Mesophase of Isotactic Polypropylene" *Macromolecules* 42 (2009), 7275 - 7278
6. Yang, B., Gao, Y. L., Zou, C. D., Zhai, Q. J., Zhuravlev, E., Schick, C. "Repeated nucleation in an undercooled tin droplet by fast scanning calorimetry" *Materials Letters* 63 (2009), 2476–2478
7. Gao, Y. L., Zou, C., Yang, B., Zhai, Q., Liu, J., Zhuravlev, E., Schick, C. "Nanoparticles of SnAgCu lead-free solder alloy with an equivalent melting temperature of SnPb solder alloy" *Journal of Alloys and Compounds* 484 (2009), 777-781
8. Mileva, D., Androsch, R., Zhuravlev, E., Schick, C. "Critical rate of cooling for suppression of crystallization in random copolymers of propylene with ethylene and 1-butene" *Thermochimica Acta* 492 (2009), 67-72
9. Gao, Y. L., Zhuravlev, E., Zou, C. D., Yang, B., Zhai, Q. J., Schick, C. "Calorimetric measurements of undercooling in single micron sized SnAgCu particles in a wide range of cooling rates" *Thermochimica Acta* 482 (2009), 1 – 7

Patent application: US 12/479,105 entitled "CALORIMETER AND METHODS OF USING IT AND CONTROL SYSTEMS THEREFOR" E. Zhuravlev and C. Schick

Conferences

1. Zhuravlev, E., Wurm, A., Schick, C., “Differential power compensated fast scanning calorimeter”. Poster, 8th International Workshop on Subsecond Thermophysics, September 26–28, 2007 Moscow, Russia
2. Zhuravlev, E., Garg, S., Wurm, A., Schick, C., “Solidification of fast crystallizing polymers studied by differential chip nano-calorimetry”. Poster, 72nd Annual Meeting of the DPG, 25-29 February 2008, Berlin, Germany
3. Zhuravlev, E., Schick, C., “Differential power compensated fast scanning calorimeter”. Poster, fast scanning calorimeter exhibition, 10th Lahnwitzseminar on Calorimetry, 8-13 June 2008, Rostock, Germany
4. Zhuravlev, E., Gao, Y-L., Wurm, A., Schick, C., “Solidification of polymers and metal particles studied by differential fast scanning calorimetry”. Poster, The Polymer Processing Society 24th Annual Meeting, 15-19 June 2008, Salerno, Italy
5. Zhuravlev, E., Burkel, E., Schick, C., “Fast thermal processing by differential chip calorimeter”. Poster, Marie Curie Conference, 17-18 July 2008, Barcelona, Spain
6. Zhuravlev, E., Gao, Y-L., Schick, C., “Actively Power Compensated Differential Scanning Calorimeter for Studying of Solidification of Metals and Polymers on Millisecond Time Scale”. Lecture, North American Thermal Analysis Society (NATAS) 36th Annual Conference, 16-20 August 2008, Atlanta GA, USA
7. Zhuravlev, E., Schick, C., “Differential power compensated fast scanning calorimeter”. Poster, lecture[#], North American Thermal Analysis Society (NATAS) 36th Annual Conference, 16-20 August 2008, Atlanta GA, USA
8. Zhuravlev, E., Schick, C., “Solidification of polymers and metal nano-particles studied by differential fast scanning calorimeter”. Lecture, Fast Scanning Calorimeter exhibition, The 13th International Conference on Rapidly Quenched & Metastable Materials RQ13 24-29 August 2008, Dresden, Germany
9. Zhuravlev, E., Schick, C., “Fast scanning calorimetry at processing relevant cooling rate”. Lecture, Fast Scanning Calorimeter exhibition, The Polymer Processing Society 25th Annual Meeting, March 1-5, 2009, Goa, India
10. Zhuravlev, E., Schick, C., “Solidification of polymers at controlled high cooling rates. Differential fast scanning calorimeter”. Lecture, Fast Scanning Calorimeter exhibition, 18th Ulm-Freiberg Kalorimetrietage, March 18 – 20, 2009, Freiberg, Germany
11. Zhuravlev, E., Schick, C., “PCL solidification investigation using fast scanning calorimeter nuclei formation in wide range of time-temperature scale”. Poster, Fast Scanning Calorimeter exhibition, Seventeenth Symposium on Thermophysical Properties, June 21-26, 2009, Boulder CO, USA
12. Zhuravlev, E., Schick, C., “PCL solidification investigation using fast scanning calorimeter nuclei formation in wide range of time-temperature scale”. Poster, Fast Scanning Calorimeter exhibition, Calorimetry Conference CALCON 2009, June 28 – July 2, 2009, Santa Fe NM, USA

[#] Graduate Student Travel Award for the lecture “Differential Fast Scanning Calorimeter”

13. Zhuravlev, E., Schick, C., "Solidification of polymers at controlled high cooling rates. Differential fast scanning calorimeter". Poster, Fast Scanning Calorimeter exhibition, Material days, July 9,10 2009, Rostock, Germany
14. Zhuravlev, E., Schick, C., "PCL solidification investigation using fast scanning calorimeter nuclei formation in wide range of time-temperature scale". Lecture, Poster, Fast Scanning Calorimeter exhibition, International Discussion Meeting on Polymer Crystallization (IDMPC), August 12-15, 2009, Shanghai, China
15. Zhuravlev, E., Gao, Y-L., Schick, C., "Investigation of Sn supercooling in a wide range of cooling rates studied by fast scanning calorimeter". Poster, Fast Scanning Calorimeter exhibition, North American Thermal Analysis Society (NATAS) 37th Annual Conference, September 20-23, 2009, Lubbock TX, USA
16. Zhuravlev, E., Schick, C., "Nuclei formation in PCL in a wide range of time and temperature studied by fast scanning calorimetry". Plenary lecture^{##}, North American Thermal Analysis Society (NATAS) 37th Annual Conference, September 20-23, 2009, Lubbock TX, USA
17. Zhuravlev, E., Schick, C., "Actively power compensated differential scanning calorimeter for studying of solidification of metals and polymers on millisecond time scale". Lecture, North American Thermal Analysis Society (NATAS) 37th Annual Conference, September 20-23, 2009, Lubbock TX, US
18. Zhuravlev, E., Schick, C., "Solidification of polymers at controlled high cooling rate. Fast scanning calorimetry". Lecture, poster, Fast Scanning Calorimeter exhibition, 11th International Conference on Pharmacy and Applied Physical Chemistry, February 07-10, 2010, Innsbruck, Austria
19. Zhuravlev, E., Schick, C., "Nuclei formation in PCL in a wide range of times and temperatures studied by fast scanning calorimeter". Lecture, Nucleation Theory and Applications, April 10 - 17, 2010, Dubna, Russia

^{##} Perkin Elmer Student Award for the lecture "Nuclei formation and growth in PCL in a wide range of times and temperatures studied by fast scanning calorimeter"

Acknowledgements

I want to thank my “ADVATEC” program co-supervisors Prof. Dr. Christoph Schick, Rostock, and Prof. Dr. Eberhard Burkel, Rostock, very much for giving me the opportunity to carry out this work. The very essential and fruitful discussions helped me to get a deeper insight into many current problems of calorimetry and polymer solidification.

I would like to thank Dr. Alexander Minakov, Moscow, for valuable discussions and ideas.

I am very grateful to all my colleges (former and present) for their support and friendship.

Prof. Dr. Dongshan Zhou, Prof. Dr. Wenbing Hu, Nanjing University, Prof. Dr. Yu-Lai Gao, Shanghai University and Dr. Jörn Schmelzer, University of Rostock, I acknowledge for the important contribution to phenomenological and theoretical interpretation of my data.

I am very thankful for the European Union funded Marie Curie EST fellowship, which allowed me to carry out this work, and Functional Materials Rostock e.V. for the possibility to present my work at several international conferences.

This work would not be possible without the serious support and help from my family.

Erklärung

Ich versichere hiermit an Eides statt, dass ich die vorliegende Arbeit selbstständig angefertigt und ohne fremde Hilfe verfasst habe, keine außer den von mir angegebenen Hilfsmitteln und Quellen dazu verwendet habe und die den benutzten Werken inhaltlich und wörtlich entnommenen Stellen als solche kenntlich gemacht habe.

Rostock,

Evgeny Zhuravlev